2009

Investigations of Crystallization of Molecular Sieves and their Behaviour under High Pressures

Yueqiao Fu

Recommended Citation

Fu, Yueqiao, "Investigations of Crystallization of Molecular Sieves and their Behaviour under High Pressures" (2009). *Digitized Theses*. 4281.
https://ir.lib.uwo.ca/digitizedtheses/4281

Investigations of Crystallization of Molecular Sieves and their Behaviour under High Pressures

(Spine Title: Molecular Sieve Formation and Behaviour under High Pressure)

(Thesis Format: Integrated-Article)

By

Yueqiao Fu

Graduate Program in Chemistry

Submitted in partial fulfillment
of the degree of
Master of Science

School of Graduate and Postdoctoral Studies
The University of Western Ontario
London, Ontario
Canada

THE UNIVERSITY OF WESTERN ONTARIO

SCHOOL OF GRADUATE AND POSTDOCTORAL STUDIES

CERTIFICATE OF EXAMINATION

Supervisor	Examiners
Dr. Yining Huang	Dr. John F. Corrigan
Supervisory Committee	Dr. Paul J. Ragogna
	Dr. Liying Jiang

The thesis by

Yueqiao Fu

entitled:

Investigations of Crystallization of Molecular Sieves and their Behaviour under High Pressures

is accepted in partial fulfillment of the requirements for the degree of Master of Science

Date________________________

Chair of the Thesis Examination Board

ABSTRACT

The behaviour of completely siliceous zeolite ZSM-5 under high pressure up to 16 GPa were investigated by *in situ* Raman spectroscopy, Infrared spectroscopy and X-ray diffraction with synchrotron radiation using diamond anvil cell. Pressure-induced amorphization was observed in both as-made and calcined siliceous ZSM-5 which transform to a low-density amorphous silica first and then to a high-density amorphous silica. However, transition pressures and reversibility were different for the as-made and calcined siliceous ZSM-5. It was found that the occluded template molecules are the major factor for these differences.

The crystallization mechanism of $AlPO_4$-16 molecular sieve was preliminarily investigated under dry gel conversion method by X-ray diffraction and Solid-State NMR spectroscopy. The $AlPO_4$-16 and a crystalline by-product which has similar structure were formed via a semi-crystalline layered AlPO intermediate. The by-product could be transformed to amorphous materials with different structures by calcination and washing with distilled water.

Keywords:

Molecular sieve, High pressure, Pressure-induced amorphization, ZSM-5, Diamond anvil cell, Raman spectroscopy, Infrared spectroscopy, X-ray diffraction, Synchrotron radiation, Crystallization, Dry gel conversion (DGC), $AlPO_4$-16, Solid-State NMR spectroscopy

To my dear husband, Qingxiang Song and our parents

ACKNOWLEDGEMENTS

First and foremost I would like to express my sincere thanks to my supervisor, Professor Yining Huang. Without his guidance, encouragement and patience, this thesis would not have been possible. Yining has set a fantastic example not only as a scientist but also as a successful person. His personality and thought will affect me for a life time.

I would like to express my gratitude to Dr. Yang Song for granting me unlimited use of his high-pressure equipment and helping me do the synchrotron X-ray diffraction experiments at Argonne National Laboratory. My research could not be done so smoothly without his valuable discussions and technical support.

I would also like to thank my examiners and advisors, Dr. John Corrigan, Dr. Paul Ragogna, Dr. Liying Jiang, Dr. Peter Norton and Dr. Peter Guthrie for their valuable advice and friendly help.

My gratitude is also extended to Dr. Nicholas Payne for his interesting and helpful course. I would like to thank former and present NMR managers, Dr. Zhimin Yan and Dr. Mathew Willans, for their technical assistance. I would also like to thank Ms. Grace Yau for my XRD experiments, Ms. Zhaohui Dong for my high-pressure experiments, Dr. Todd Simpson for the SEM and the many other people in the department whom I got help from.

I feel greatly honored working together with the many intelligent group mates of the Huang lab group: Dr. Zhimin Yan, Dr. Banghao Chen, Dr. Jianfeng Zhu, Dr. Li Liu, Janice Lee, Andre Sutrisno, Lu Zhang and Jun Xu. I appreciate their kindly help and especially want to thank Janice for proofreading my thesis. I would like to thank all my friends for their support and encouragement.

Last but not the least, I would like to thank my dear husband, Qingxiang Song, for his love and support throughout this project. I would love to thank my parents, who always love me, believe in me, and pray for me on the other half of the earth.

TABLE OF CONTENTS

LIST OF FIGURES

LIST OF TABLES

ABBREVIATIONS

5MR	five-membered rings
Å	Angstrom
ADXRD	Angle Dispersive X-ray Diffraction
$AlPO_4$	aluminophosphate
APS	Advanced Photon Source
atm	atmospheric pressure
BDCM	Branching Double-Crystal Monochromator
Catapal B	Al_2O_3
CCD	Charge-Coupled Device
cm^{-1}	wavenumber
d	d-spacing
dv/dP	pressure dependence of frequency
D6R	double six-rings
DAC	Diamond Anvil Cell
DGC	dry gel conversion
EDM	Electric Discharge Machine
EDXRD	Energy-Dispersive X-ray Diffraction
eV	electron volt
FIB	Focused Ion Beam
FT	Fourier transform
FWHM	full width at half maximum
GPa	giga pascal
HDA	high density amorphous
HEX	hexamethyleneimine
hkl	Miller indices
HPCAT	high pressure collaborative access team
HTS	hydrothermal synthesis
i.d.	inside diameter
IR	Infrared radiation
IZA	International Zeolite Association
KB	Kirkpatrick–Baez
keV	kiloelectron volt
kHz	kilohertz
LDA	low density amorphous
LUDOX	30 wt% colloidal silica
MAS	Magic Angle Spinning

mbar	millibar
MCT	mercury cadmium telluride
MeAlPOs	metal aluminophosphate
MHz	megahertz
MOFs	metal-organic frameworks
mol	mole
ms	millisecond
n	reflection
NBS	National Bureau of Standards
nm	nanometer
NMR	Nuclear Magnetic Resonance
P	pressure
PAP	primary amorphous phase
PIA	pressure-induced amorphization
PIH	pressure-induced hydration
ppm	part per million
PTM	pressure-transmitting medium
Q	quinuclidine
rf	radiofrequency
SAC	steam-assisted conversion
SAP	secondary amorphous phase
SAPOs	silicon aluminophosphate
SAXS	Small-Angle X-ray Scattering
SBUs	second building units
SDA	structure-directing agent
SEM	Scanning Electron Microscopy
SR	Synchrotron Radiation
SS-NMR	Solid-State Nuclear Magnetic Resonance
T	temperature
T	tesla
Teflon	polytetrafluoroethene
TG-DTA	Thermogravimetric- differential thermal analysis
TMS	tetramethylsilane
TO_4	tetrahedra unit
TPA^+	tetrapropylammonium cation
TPAB	tetrapropylammonium bromide
UV-Vis	Ultraviolet/Visible spectroscopy
VPT	vapour phase transport
WAXS	Wide-Angle X-ray Scattering
WB	Weber

WC	tungsten-carbon alloy
XAS	X-ray absorption spectroscopy
XRD	X-ray diffraction
ZSM-11	Zeolite Socony Mobil #11
ZSM-5	Zeolite Socony Mobil #5

δ	bending vibration
$\Delta\lambda$	wavelength difference
θ_{hkl}	Bragg angle
λ	wavelength
λ_0	wavelength measured at 1 bar
μm	micrometer
μrad	microradian
μs	microsecond
ν	symmetric stretching vibration
ν_0	vibrational frequency of incident beam
ν_{as}	asymmetric stretching vibration
ν_m	vibrational frequency of the molecule

Chapter 1 Introduction

1.1 Molecular Sieves

1.1.1 Definition and Evolution of Molecular Sieves

Molecular sieves are porous materials containing channels and cavities with pores of the size of molecular dimensions. The most well known family of molecular sieves is the zeolites which are crystalline aluminosilicates of alkali and alkaline earth group elements such as Na, K, Mg, and Ca. They are widely utilized in industry as ion-exchangers, sorbents, and catalysts.[1]

The history of zeolites began in 1756 when the first zeolite mineral was discovered by the Swedish mineralogist Cronstedt. The word 'zeolite' has Greek roots and means 'boiling stones', an allusion to the visible loss of water noted when the natural zeolites are heated.[2]

Natural zeolites are considered to occur typically as minor constituents in a variety of geological environments mainly from volcanic debris. The widespread occurrence of numerous natural zeolites are revealed by geologic discoveries.[1] They may well be important to the formation of other minerals, such as feldspars and clay minerals by alteration.[2]

The first synthetic zeolite was reported by St. Claire using hydrothermal synthesis in 1862.[3] However, the early studies largely concentrated on the synthesis of the synthetic zeolites by simulating the high temperatures and pressures ($T > 200$ °C, $P > 10000$ kPa) conditions under which natural zeolites were believed to form. The first definitive synthesis of zeolites including the synthetic analogue of the zeolite mineral mordenite was reported by Barrer in 1948.[4] Inspired by the pioneering work of Barrer, researchers at Union

Carbide laboratories initiated large scale synthetic methodologies and developed hydrothermal zeolite syntheses at low temperature (ca. 100 °C) using alkali metal aluminosilicate gels in the late 1940s.[5, 6]

Over the last fifty years, the research on molecular sieves has been a quest for new structures and compositions. In 1967 – 1969 Mobil Oil reported the synthesis of the high silica zeolites beta and ZSM-5. The completely siliceous zeolite ZSM-5, also referred to as silicalite-1 and other analogues were synthesized in the early 1970s. ZSM-5 and silicalite-1 have achieved commercial significance up to now.[1] Recently, metallosilicates were synthesized by incorporating heteroatoms which substitute for silicon in a known silicate framework. The most important substitution is titanium for silicon; the titanosilicalites-1 is the titanosilicate analogue of ZSM-5.[7]

The discovery of the aluminophosphate ($AlPO_4$) molecular sieves by Wilson and co-workers in 1982 announced a beginning of the chemistry of non-silicate microporous materials.[8] Based on this discovery, other related materials were synthesized by incorporating other elements into the framework, such as MeAlPOs and SAPOs which contain metal and silicon, respectively. Since then a variety of new classes of microporous materials have been synthesized by including a large number of main group (Ge, Ga, In)[9, 10] and transition metal (Fe, Co, Zn)[11, 12] elements.[13] Nowadays, $AlPO_4$-based materials have shown several important applications in industry.[1]

One of the fastest-growing classes of microporous materials is composed of metal-organic frameworks (MOFs) in which organic groups form part of the framework.[14] These materials have attracted much attention in recent years since the organic groups can be modified by different functional groups. As a result, they can offer exciting new possibilities and applications.[15-17]

1.1.2 Nomenclature and Structures of Molecular Sieves

For molecular sieves, there is no systematic nomenclature. The discoverer of the synthetic species based on a characteristic X-ray powder diffraction pattern and chemical composition assigns trivial symbols. Some used the Arabic alphabet and some used the Greek alphabet. The molecular sieve literature is replete with acronyms. With more novel materials being synthesized by different research groups, the naming convention became more complicated. Some materials with different names actually have the same structure type, while quite different structures may have similar numerical designations. In order to differentiate certain structure types, the International Zeolite Association (IZA) Structure Commission assigns a three-letter code to be used for a known framework topology irrespective of composition and unit cell symmetry.[18] As a result, the same structure type with different names can be represented by a single three-letter code. For instance, FAU is used for molecular sieves with a faujasite topology, including zeolite X and Y; MFI is assigned to ZSM-5 and silicalite-1, both of which have the same topology.[1]

Zeolites comprise corner-sharing AlO_4 and SiO_4 tetrahedral units connected via bridging oxygens to form a three-dimensional network. Each AlO_4 tetrahedron in the framework bears a net negative charge which is balanced by an extra-framework cation, whereas pure silica frameworks are electrically neutral. The frameworks of $AlPO_4$ molecular sieves which are also electrically neutral are built upon alternating, corner-sharing PO_4 and AlO_4 tetrahedra.

Zeolite structure types can be described in terms of identifiable structural units which are often referred to as second building units (SBUs) within the frameworks. The SBUs and frameworks are usually described by rings made up of corner-sharing TO_4 tetrahedra, where T is referred to as tetrahedral site. T can be any tetrahedrally coordinated cation which is Al or Si for zeolite. For instance, six-membered rings (6MR) contain six T atoms and six oxygens, 8MR contain eight T sites and eight oxygens, and so on. Some SBUs are considered as being constructed by two rings linked together as a prism. The two n-membered rings connected in this way are described as double n-rings. The examples include D4R, D6R, and so on (Figure 1.1 (a)). Some more complicated building units which can be used to built up important structures are also considered as SBUs, including the α-cage and the β-cage (sodalite cage).[16] Figure 1.1 (b) illustrates the structure of zeolite A containing α- and β-cages.

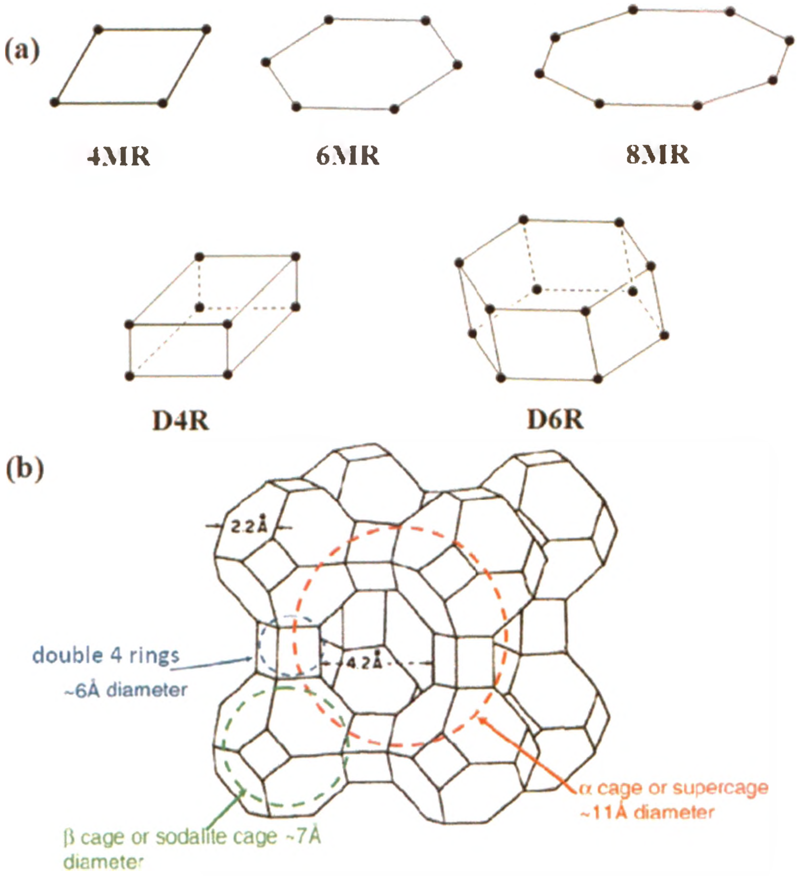

Figure 1.1 (a) Several SBUs found in molecular sieve frameworks; (b) The structure of zeolite A, showing the SBUs: the *α* cage, *β* cage and D4R. The openings for the *α* and *β* cages are indicated. The corners of the SBU polyhedra define the positions of Si and Al tetrahedra and the edges the bridging oxygens. (Adapted from Ref. 19)

1.1.3 Applications of Molecular Sieves

The properties of ion exchange, sorption and diffusion are among the most important properties of molecular sieves. Cations which compensate the negative charges of the framework can be exchanged partially or totally. These microporous materials show the so-called molecular sieving effect since the cages and channels are of molecular dimensions, allowing the entrance of certain molecules and excluding the others due to their sizes. When the molecules or ions are adsorbed in the inner pores of these materials, they will diffuse through the channels and cavities to reach a specific adsorption site.[20]

The protonated forms of zeolites which could be used as active, stable and shape selective catalysts in hydrocarbon transformations have shown great benefit to the refining and petrochemicals industry. A variety of feedstock and fine chemicals synthesis are also being developed using zeolites as catalysts. For example, MFI type zeolites play a special role in selective alkylations and isomerisations of monoaromatics *via* diffusion and transition state selectivity. The $AlPO_4$-based molecular sieves containing redox-active framework cations such as Co(II) and Co(III) can be used in selective oxidations.[16]

Recently, zeolite thin films and membranes have been extensively studied, which may be applied in high-temperature industrial applications of sensing and more efficient separation and catalysis. Zeolites can be used as auxiliary agents in the detergent industry, in radioactive waste treatment and storage, and in the treatment of waste water and auto-exhaust. Zeolites are also considered as inert carriers in medical diagnosis and treatment.[20, 21]

1.2 High-Pressure Studies

1.2.1 Overview of High-Pressure Studies

The concept of pressure is vital to physics and chemistry, and the earliest high-pressure studies can be dated back to Boyle's formulation of his gas laws in the 17th century.[22] Static high pressure in excess of 300 GPa (1 GPa = 10^9 Pa = 10000 atm), a pressure close to the pressure in the earth core (around 330 – 360 GPa) can be generated on samples in some laboratories by advanced techniques.[23]

Associated with high pressure, free energy change (pressure-volume work) of the materials can be in excess of 10 eV, which exceeds the strengths of the strongest chemical bonds. Such an effect can completely redistribute electronic densities, driving dramatic changes in the chemistry of a molecular system, because under such conditions interactions among atoms increase substantially when the effective volume occupied by the constituent particles is reduced. The densities of materials can be increased by over an order of magnitude inducing a variety of transformations and new physical and chemical phenomena.[23, 24]

Upon compression, chemical bonds and affinities of otherwise familiar elements and compounds can be entirely altered, thus new classes of materials with unusual combinations of physical properties can be formed, such as novel superhardness and unusual electronic properties. Furthermore, new high-pressure techniques provide an important means to carefully tune electronic, magnetic, structural, and vibrational properties for testing fundamental theory and a wide range of new applications.[25]

Diamond anvil cell (DAC) methods, new synchrotron diffraction and spectroscopy techniques with a wide detection range from X-ray to far infrared region are especially important high-pressure techniques with rapid progresses.[23, 26]

1.2.2 High-Pressure Studies on Zeolites

As previously mentioned, zeolites have numerous industrial applications.[1] The effective application of zeolites in chemical processes in industry requires a thorough understanding of the behaviour of the zeolites under the applied conditions, which may be different from the ambient ones, and the stability of zeolites is important to their applications. To this end, many experimental and theoretical studies of zeolites have been focused on their behaviours under high temperature at ambient pressure for many years.[27, 28] However, there exist only a few studies of the behaviours of zeolites under external pressure in the past several decades.[19, 29-37] This is partly due to the experimental complexities and the analytical ambiguities arising from the porous nature of the materials.[29, 38] Most important high-pressure studies on zeolite in the literature are briefly summarized below.

Pressure-induced structural transformations of zeolites between crystalline phases were first studied by Hazen and Finger. They discovered several high-pressure induced phase transitions in the natural zeolite analcime and described the transitions as polyhedral tilt (displacive) transitions.[39] Since then there have been more studies on natural zeolite (natrolite,[38] scolecite,[40, 41] heulandite[42, 43]) and synthetic zeolite (zeolite Rho,[31] silica sodalite[44]).

Pressure-induced hydration (PIH) in natrolite was originally proposed by Belitsky *et al.*[38] However, only recently the experimental confirmation of PIH was determined by modern analytical techniques such as high-resolution synchrotron X-ray and reliable structural models of zeolites. Under high-pressure conditions, small molecules such as water and alcohols used as the pressure-transmitting medium are penetrating to the cavities and channels of zeolites resulting in "super-hydrated" zeolites and lead to a volume expansion of the zeolite framework.[32, 45-50] PIH which occurred in the zeolites with a natrolite framework[48, 50, 51] illustrated that the distribution and coordination of nonframework species can be distinctly changed by applying high pressure. PIH in natrolite can also lead to well-ordered one-dimensional "water wires" and "water tubes".[52, 53] In other large-pore zeolites such as faujasite and zeolite A, PIH, which is a continuous process can change the framework's compressibility resulting in more disordered water networks inside the pores.[45, 49, 51] Recently, more PIH studies on synthetic zeolite with different frameworks were reported, such as gallosilicate zeolite.[54, 55]

The effect of pressure on ionic conductivity of zeolite A with different cations was studied by Secco and Huang.[36, 56, 57] The ion conductivity of the hydrated NaA zeolite showed an anomalous increase at a relatively low pressure range (~0.5 – 1.8 GPa), which may be caused by structural changes in the stuffing of zeolite pores with activation of interstitial sites and water-assisted increase of Na^+ cation mobility.[36]

Pressure-induced amorphization (PIA), which is the formation of an amorphous phase within a solid state by applying external pressure, has received a great deal of attention since its initial discovery on hexagonal ice.[58] The phenomenon has been observed in many condensed matters, such as silicates, phosphates, hydroxides, and pure elements,[59-62] thus it is believed that the pressure-induced amorphous state is a universal property of condensed materials.[63] The nature of the PIA process has been the subject of many experimental and theoretical studies by different analytical probes which are sensitive to different length scales: *in situ* X-ray diffraction, Raman, Infrared and Brillouin spectroscopies, and high-resolution scanning electron microscopy of the recovered samples.[33, 47, 64-67]

The underlying mechanisms, however, remain largely speculative. Several hypotheses have been proposed to explain PIA including thermodynamic melting,[58, 59] mechanical instability,[68] and kinetic hindrance of phase transformations to a thermodynamically stable high-pressure phase.[69, 70] Some new structural factors such as polyhedral packing[71] and increased atomic coordination[68, 72] may also cause the PIA process.

The natrolite group zeolites were found to experience several phase transitions under high pressure and the PIA might occur at the pressures above 8 GPa reported by Belitsky *et al.*[38] Since then PIA and the reversibility of this process upon decompression of zeolites have been widely investigated experimentally and theoretically.[33, 64, 65, 72, 73]

The pressure-induced amorphous phase of some zeolites under high pressures was found partially or totally to recover the initial zeolite's crystalline structure upon decompression to ambient pressure.[30, 64, 74, 75] The occurrence of such reversibility may depend on the maximum pressure applied, the time under compression and the existence of the non-deformable units (such as hydrated charged balancing cations and template molecules in the framework) driving the reversible transformation.[30, 74, 75] Such property is also called structural memory effect. The guest molecules can also serve as the centres redirecting the collapsed host frameworks around them back to their original structures. On the other hand, the framework of zeolites without guest species could not be recovered.[33, 70]

Recent work by Greaves and co-workers has renewed the interest in PIA.[19, 47, 76, 77] Their results show that a zeolite may contain two different pressure-induced amorphous phases: a low density amorphous (LDA) phase which might form a 'perfect glass' with ordered structure and negligible configuration entropy, and a high density amorphous (HDA) phase with conventional density of alumino-silicate glass in the course of amorphization. This phenomenon is called polyamorphism: occurrence of more than one amorphous phase with the same chemical composition but different densities and entropies.[78] Moreover, the crystalline topology (i.e., the atomic coordination and bonding) is found to be preserved in the LDA phase and lost in the HDA phase.[79] Cohen, Iniguez, and Neaton suggested that amorphization will be reversible in the former phase and irreversible in the latter.[73] These results accompanied with other studies show that the reversibility of PIA largely depends on the zeolite composition.[35, 65, 75, 80]

1.3 Crystallization Studies

1.3.1 The Process of Molecular Sieve Crystallization

As mentioned before, molecular sieves which have many practical applications have been discovered and studied for over fifty years, however, there is still a lack of knowledge about the mechanism of the crystallization process.[81, 82] There is a pressing demand to understand the formation mechanisms of these materials under different synthetic conditions so that the design of new materials with required properties for particular applications will be possible.[83]

The most probable mechanistic process in zeolite formation can be divided into three major periods in sequence: induction period, nucleation, and crystal growth.[81] The determination of the end of each period is dependent on the method of analysis; the most general way is a combination of microscopic methods or visual inspection with diffraction methods. So far, crystallization kinetic studies of molecular sieves are mostly based on the measurement of an S-shaped growth curve of detectable crystallinity against time (Figure 1.2).[21, 84]

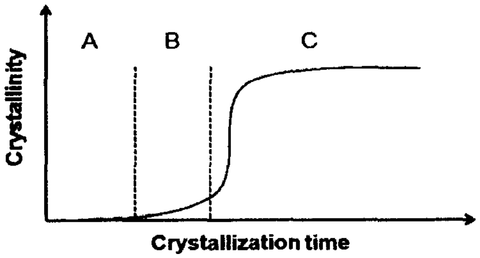

Figure 1.2 The S-shaped growth curve for the crystallization of molecular sieves: (A) induction period, (B) nucleation, and (C) crystal growth.

The induction period is considered to be the time between the notional start of the reaction and the point at which crystalline product is first detectable. Before this period, there only exists the individual reactants in the initial reaction mixture; after this period, numerous small zeolite crystals already form and grow larger and larger. Since the growth process has no discontinuity when it starts, the mechanism of further growth is already established in this early period.[81] It is apparent that this period contains all the important elements of the crystallization of molecular sieves.[85]

It is often convenient to assume the amorphous phase, which is the undetectable phase, before the end of the induction period remains unchanged during this stage. This approach is usually adopted in reaction modelling.[86] However, the earliest mechanistic studies recognised the dynamic nature of this phase.[87] Moreover, the evolution of this amorphous material is really essential in the early stages of the reaction. Figure 1.3 shows an evolution of the materials under hydrothermal synthesis (HTS) conditions.

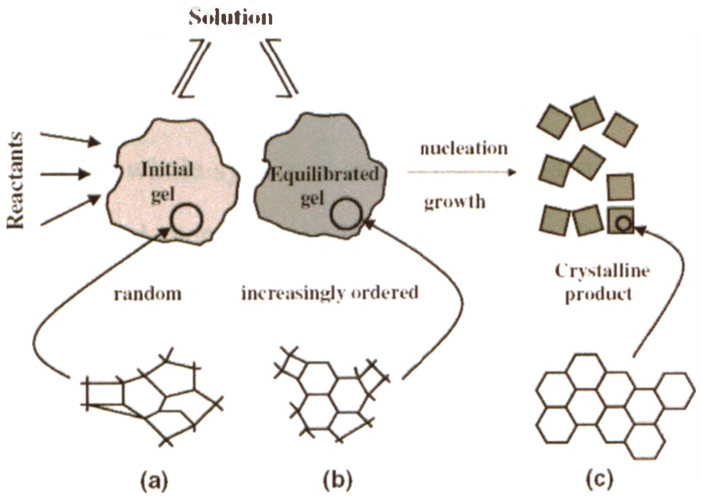

Figure 1.3 The evolution of order, from the primary amorphous phase (a) through the secondary amorphous phase (b) to the crystalline product (c). (Adapted from Ref. 81)

Generally, a visible gel is formed when the synthesis reactants are blended together.

This is referred to as the primary amorphous phase (PAP) which is a heterogeneous phase containing the initial and immediate products from the reactants. Upon heating the reactants for a period of time, the equilibration reactions occur, resulting in a re-distribution of species and repartition of reaction components between the solid and liquid phases when they gradually approach equilibrium. Then a reconstructed phase or so-called secondary amorphous phase (SAP) forms, which has a similar chemical composition to that of the final zeolite product. However, SAP is X-ray amorphous because of lacking long-range, periodical order. Its existence has been reported[88] and this phase is vital in the zeolite nucleation stage.

After the induction period, there is a stage during which the amorphous phase keeps increasing its structural ordering but without the formation of the periodic zeolite lattice. Finally, some areas of the structure become ordered enough, a periodic lattice will propagate, which means the occurrence of nucleation. As a result, nucleation could be defined as "a phase transition whereby a critical volume of a semi-order gel network is transformed into a structure which is sufficiently well ordered to form a viable growth centre from which the crystal lattice can propagate." [81] It is important to emphasize that the process is dynamic for the whole system at any moment, and such more ordered areas are being created, up-graded and even destroyed simultaneously. However, the overall trend of the degree of order is increasing.[89]

The last stage of the zeolite formation (crystal growth) is also very significant because this is usually the step that can be monitored in a laboratory or synthetic factory.[81] The crystalline product can be considered to be a semi-covalent, three dimensional polymer of "TO_2" (T = tetrahedral site), which is assembled piece by piece through the formation of T-O-T bonds. Thus, the crystals seem to grow rather slowly compared to the other types of crystals. The overall growth rate of zeolite formation from the predominant layer-by-layer adsorption growth model is determined by the surface integration step and the nucleation of a new layer which is slower than the lateral spread of such a layer.[90]

1.3.2 Crystallization Mechanisms of $AlPO_4$-based Molecular Sieves

Compared to the other molecular sieves, the mechanisms of crystallization of $AlPO_4$-based molecular sieves have been relatively less studied. It is generally believed that there are at least two stages in the synthesis of the materials under conventional HTS conditions.[91] The first stage is the aluminum containing starting material reacts with phosphoric acid to form an amorphous AlPO layer.[92] The next stage(s) is the transformation from layer to crystalline product. The process is less clear because the induction and nucleation periods of crystallization in aqueous solution under HTS conditions are fast.[93, 94] An additional difficulty is the identification and subsequent characterization of the true intermediates which may be altered by the post-synthesis treatments, such as washing.[91, 95]

1.3.3 General Methods to Study Crystallization Mechanisms of $AlPO_4$-based Molecular Sieves

1.3.3.1 Hydrothermal Synthesis (HTS) Method

The $AlPO_4$-based Molecular Sieves are generally synthesized by the traditional HTS method in autoclaves from an active aluminophosphate gel containing an organic template at a temperature above 100 °C and under autogenous pressure. The phosphorous source is usually orthophosphoric acid, and the aluminum source is either alumina or aluminum alkoxide in most cases. The organic template molecule plays a dual role as a structure-directing agent (SDA) and a pH controller. An appropriate gel composition and the type of SDA is important to synthesize a specific $AlPO_4$-n (n denotes a specific structure type).[1]

The crystallization mechanisms are commonly studied by analyzing the important intermediate phases formed during the synthesis. These intermediates are obtained by quenching the reactions. Such intermediates or precursors (solid phase) of the final products are isolated from the liquid phase and then characterized. Although the crystallization mechanisms of $AlPO_4$-n have been largely studied using this method,[91, 96-98] they are still not yet fully understood due to the fact that HTS is an extremely complicated process involving many reactions with both solid and liquid phases co-existing.[99] It is quite difficult to characterize the true intermediates whose structures may be changed by washing or isolation[95]. Sometimes, it is not clear that the solid phases are real intermediates or just competing phases.

Recently, some *in-situ* studies of the crystallization process of microporous materials have been performed using techniques such as ultraviolet/visible spectroscopy (UV-Vis),[100] nuclear magnetic resonance (NMR) spectroscopy,[101] X-ray absorption spectroscopy (XAS),[102] energy-dispersive X-ray diffraction (EDXRD)[103] and small-angle/wide-angle X-ray scattering (SAXS/WAXS).[82] *In-situ* methodologies are real-time studies that probe the processes occurring during crystallization without the need for quenching the reactions. However, it is difficult to use *in-situ* methods under HTS conditions because such techniques require specially designed reaction vessels which can sustain high pressure and temperature. Such special vessels are generally suitable for one or two related techniques to study crystallization at the same time, which means that the characterization is usually partial and insufficient to gain a thorough understanding of the crystallization process.[82, 91]

1.3.3.2 Dry Gel Conversion (DGC) Method

Dry gel conversion (DGC) is a relatively new synthetic method, which was initially introduced by Xu and co-workers in the 1990s to synthesize zeolite ZSM-5.[104] Recently, DGC has been used in the synthesis of many types of zeolites and $AlPO_4$-based molecular sieves.[95, 105, 106]

A comparison between the conventional HTS method and the DGC method is illustrated in Figure 1.4. As shown in Figure 1.4 (a) the hydro-gel of HTS contains all sources for the formation of final product, including SDA. DGC method can be further divided into two different but related methods: (1) steam-assisted conversion (SAC) method (Figure 1.4 (b)), in which the pre-dried gel powders containing SDA are physically separated from a very small amount of pure water in an autoclave. (2) Vapour phase transport (VPT) method (Figure 1.4 (c)), which is similar to SAC except that the SDA is not contained in the initial dry gel. A small amount of SDA aqueous solution is placed at the bottom of the autoclave. For the SAC method, all the reactive species are contained in the solid phases. The small amount of bulk water is separated from the dry-gel, which prevents the direct contact between reactive species in solution and solid gel. The small amount of water in vapor is not enough to dissolve the solids. Therefore, the formation of a molecular sieve by SAC is unlikely through gel dissolution. For the VPT method, SDA is gradually brought in contact with the solid gel through vapor, it can be used to investigate the effect of SDA on the crystallization.[105]

It is noteworthy that although lacking an apparent liquid phase in DGC, the pre-dried powder is not completely dry. In fact, the dry powder usually contains a great deal of absorbed and surface bonded water. Thus, there is no reason to view the reactions as fundamentally different from those having a more accessible liquid phase under HTS.[81] The dry-gel samples can be characterized directly without isolation from the liquid phase. DGC method has the great potential for studying crystallization mechanism of molecular sieves, especially on crystallization process of $AlPO_4$-based molecular sieves because it can avoid altering the intermediate structure during isolation. However, there have been relatively few crystallization mechanism studies in the literature regarding the DGC method.[105, 107, 108]

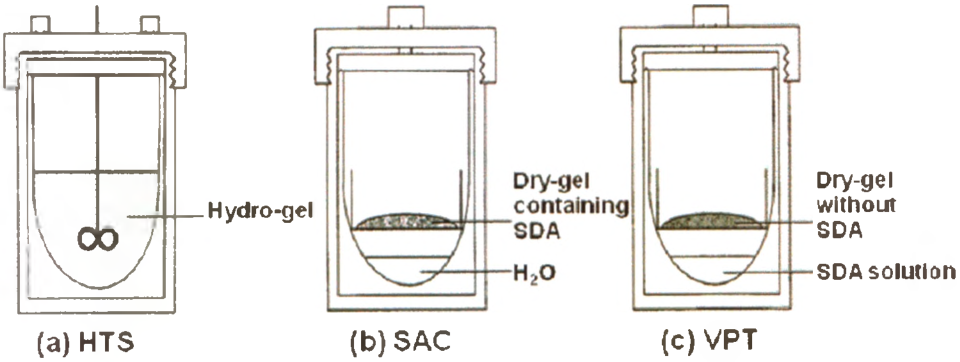

Figure 1.4 Schematic diagrams of the methods for the synthesis of molecular sieves (a) HTS method, (b) SAC method, (c) VPT method (Adapted from Ref. 105)

1.4 Apparatus and Characterization Methods

1.4.1 Diamond Anvil Cell

The diamond anvil cell (DAC) is the prevailing apparatus for high-pressure studies, which was invented and developed by Weir, Lippincott, Van Valkenburg, and Bunting of the National Bureau of Standards (NBS) in the late of 1950s.[109] The prototype of DAC can be dated back to the 1940s, when Percy Williams Bridgman developed an opposed anvil device made of tungsten-carbon alloy (WC) with small flat areas that were pressed against each other with a lever-arm. The principles of the DAC are similar to the Bridgman anvils, however, the DAC is comprised of brilliant-cut, high purity single crystal diamonds and their hardness allows one to reach the highest possible pressures without breaking the anvils. The DAC has evolved to be the most powerful device for generating static high pressures in modern laboratories.[110] The range of static pressures attainable today extends to the pressures at the Earth's center (~360 GPa).[26]

There are many different styles of DACs, for instance, P-type DAC from High

Pressure Diamond Optics Inc and the membrane cell from Easylab, UK. Depending on the type of experiments, many other types such as symmetric DAC, Merrill-Bassett type DAC are customer designed or specially made by specific laboratories.[111]

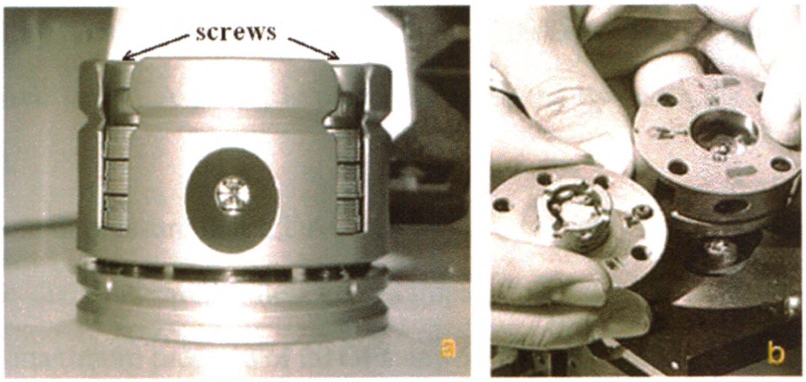

Figure 1.5 (a) Side view of an assembled symmetric piston-cylinder type DAC and (b) photo of the dissembled DAC with two parts, piston (right hand) and cylinder (left hand).

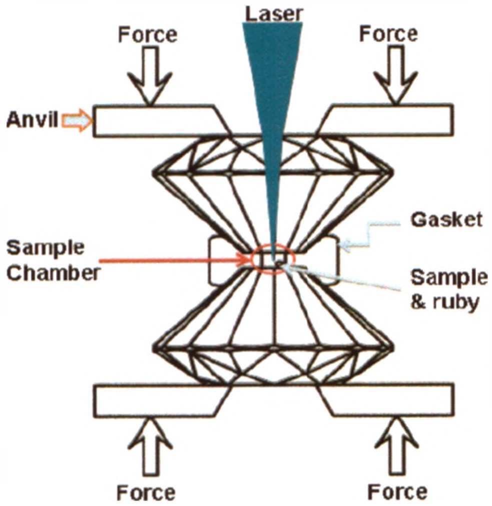

Figure 1.6 General schematic of a DAC. The force is applied symmetrically via a screw system.

Figure 1.5 (a) shows a symmetric type manufactured by Princeton University, which was used in this project. The DAC can be disassembled into two parts, a piston and a cylinder as shown in Figure 1.5 (b). The pressure can be applied by tightening the screws (Figure 1.5 (a)). The schematic structure of a symmetric DAC is shown in Figure 1.6. A pair of brilliant-cut diamonds is mounted by epoxy glue with their tables on the flat hard WC seats and tips (culet) parallel. The function of the seats is to support and transmit force to the anvil tables. A gasket is placed between the tips with the sample and ruby chips enclosed.

The maximum pressure that a DAC can achieve for safe operation is determined by the size of the diamond anvil culet. For example, culet sizes of 700 μm and 400 μm would allow a maximum pressure of 20 GPa and 50 GPa respectively. Since spectroscopy is one of the most effective probes for high-pressure studies, optical transparency is the prime factor in selecting diamonds. Two types of diamonds are used for different spectroscopic probes.[112] Type I stones (with nitrogen impurities) have strong absorption in the spectral region between 1100 and 1300 cm^{-1}, which are generally used in Raman spectroscopy.[113] Type II stones (nitrogen free) which are usually used in IR spectroscopy only have an absorption around 2000 cm^{-1} allowing IR measurements in other spectral region.[114] Gaskets are generally made of metal sheet, such as stainless steel or beryllium copper. Normally, the metal sheet is 200 – 250 μm thick. After pre-indentation using the diamond anvils, a certain thickness can be reached. Desirable thickness depends on the target maximum pressures required by the experiment.[115] A pre-indented gasket is then pierced with a mechanical micro-drill or an electric discharge machine (EDM) by spark erosion. The hole with certain diameter drilled in the centre of the pre-indented gasket is used as sample chamber. When the gasket is squeezed by the anvils, it gradually deforms with decreasing the thickness. This causes a reduction of the volume of the cylindrical hole, which results in the pressure build-up in the sample. The DAC holds the sample at constant pressures thus it is a static technique.[116]

1.4.2 Pressure Calibration

1.4.2.1 Pressure-Transmitting Media

An ideal compression environment of high-pressure studies requires the sample to be under hydrostatic conditions which means a uniform pressure across the sample chamber. It is difficult to maintain pressure homogeneity especially in the ultrahigh pressure range. A pressure-transmitting medium (PTM) may be used in order to improve the hydrostatic conditions in the sample chamber for a single crystal or a powder sample. The function of pressure-transmitting media is to make the pressure distribution in the sample more uniform when external pressure is applied.[111]

The most widely used compressing medium is a 4:1 methanol-ethanol mixture which remains hydrostatic pressure up to ~10 GPa.[117] A small addition of water with a proportion of 16:3:1 methanol-ethanol to H_2O in the mixture appears to extend the hydrostatic range of the alcohol mixture to 14.5 GPa.[111] Above 15 GPa, commercial silicone oil is more preferable to an ethanol-methanol mixture because it has lower shear strength under pressures.[118] Rare gases are the best quasi-hydrostatic pressure media,[119, 120] especially at low temperatures. The most frequently used rare gas medium is argon,[121] which can be loaded at liquid nitrogen temperature.

1.4.2.2 Ruby Pressure Gauge

A reliable and accurate pressure gauge is a vital component in high-pressure experiments. The absolute pressure is obtained indirectly by making reference to the isothermal equations of state of the metals derived from shock-wave data. Although less accurate, primary independent calibration is determined by making precise measurements of force per unit area. The calibration measurements are carried out in a number of geometrical configurations of the metal calibrant samples to average the possible effects of nonhydrostatic stress.[122-124]

The ruby gauge is the most commonly used method for pressure calibration in the DAC.[123] Ruby is Al_2O_3 doped with Cr^{3+} and ruby has two dominant luminescent peaks R_1 and R_2 when excited by shorter wavelength radiations, such as the 488 nm. The fluorescence is associated with the R_1 and R_2 transitions involving the Cr^{3+} ion. The positions of these two peaks are sensitive to pressure and shift to longer wavelengths upon compression (Figure 1.7).

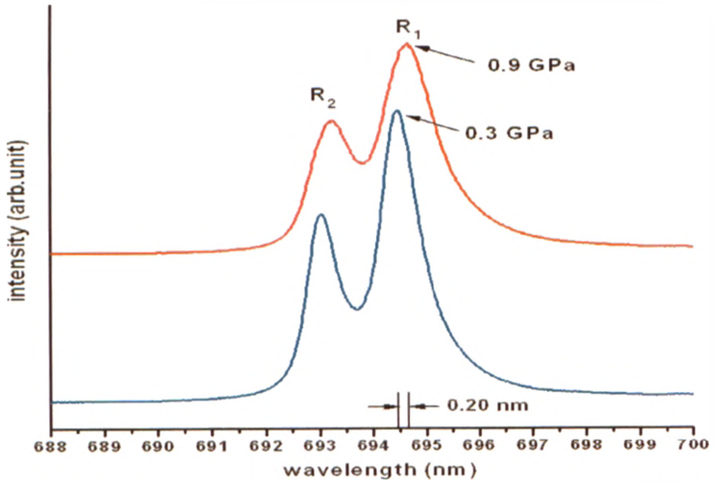

Figure 1.7 Ruby fluorescence measured at different pressures with the two luminescent lines labeled. The upper spectrum is taken at 0.9 GPa, and the lower spectrum is taken at 0.3 GPa. The red shift of the R_1 is 0.2 nm labeled in the figure. The excitation wavelength is 488 nm.

According to Mao,[125, 126] the ruby fluorescence is calibrated against Cu and W as a standard under quasi-hydrostatic conditions in argon and neon medium respectively up to 110 GPa. The calibrations in both conditions can be described in the same equation:

$$P\ (\mathrm{GPa}) = \mathrm{A/B}\ [(1+\Delta\lambda/\lambda_0)^{\mathrm{B}} - 1] \qquad \textbf{(Equation 1.1)}$$

Here, A = 1904 GPa, B = 7.665, $\Delta\lambda$ is the difference between the wavelength of the R_1

ruby line at pressure P and atmospheric pressure, and λ_0 = 694.28 nm. The sample pressure was monitored via the ruby chips placed in the gasket with the sample. Using the well-documented red shifts of the ruby fluorescence line with an accuracy of ± 0.05 GPa the pressure was determined under quasi-hydrostatic conditions.

1.4.3 Vibrational Spectroscopy

Due to the wide spectral transparency of diamonds, different types of radiations are accessible to samples loaded in DACs. The two most commonly used methods of spectroscopic characterization under high pressure are *in situ* Raman and Infrared (IR) spectroscopy.[127] Vibrational spectroscopy can provide complementary information regarding the effects of pressure on short-range ordering and local structures of the zeolite.[74] Vibrational spectra of the aluminosilicates framework are sensitive to the sizes of the TO_4 (T = Si, Al) rings present in the zeolites and provide information about the structural changes of the zeolites between the crystalline and amorphous phases under high pressure.[128]

Raman spectroscopy is a technique used to study the vibrational and rotational modes of various materials.[129] It relies on the scattering of monochromatic light, usually from a laser in visible, near infrared, or near ultraviolet range. When light is scattered from a molecule, most photons undergo Rayleigh or elastic scattering; that is, they have the same energy and wavelength as the incident photons. However, a small fraction of the scattered light ($\sim 1/10^6$ photons) is inelastically scattered by an excitation. These photons have different frequencies than that of the incident photons. This is referred to as Raman scattering. It occurs because the electron cloud can be perturbed by molecular vibrations; it is possible for the optical (incident light) and vibrational oscillations to interact to produce Raman scattering. Raman scattering is much weaker than the incident beam ($\sim 10^{-5}\ \nu_0$; ν_0 = incident beam). Its frequency is equivalent to $\nu_0 \pm \nu_m$, where ν_m is the vibrational frequency of the molecule. Stokes scattering is generated when a molecule is excited from the ground state to a virtual energy state and then relaxes into a vibrational excited state ($\nu_0 + \nu_m$). In this case, the energy of the scatting is less than the incident energy. If the molecule was already in an elevated vibrational energy state, anti-Stokes scattering is generated as the molecule relaxes back to the ground state ($\nu_0 - \nu_m$). In this case, the scatted energy is more than the incident energy. Rayleigh and Raman scattering are shown in Figure 1.8.

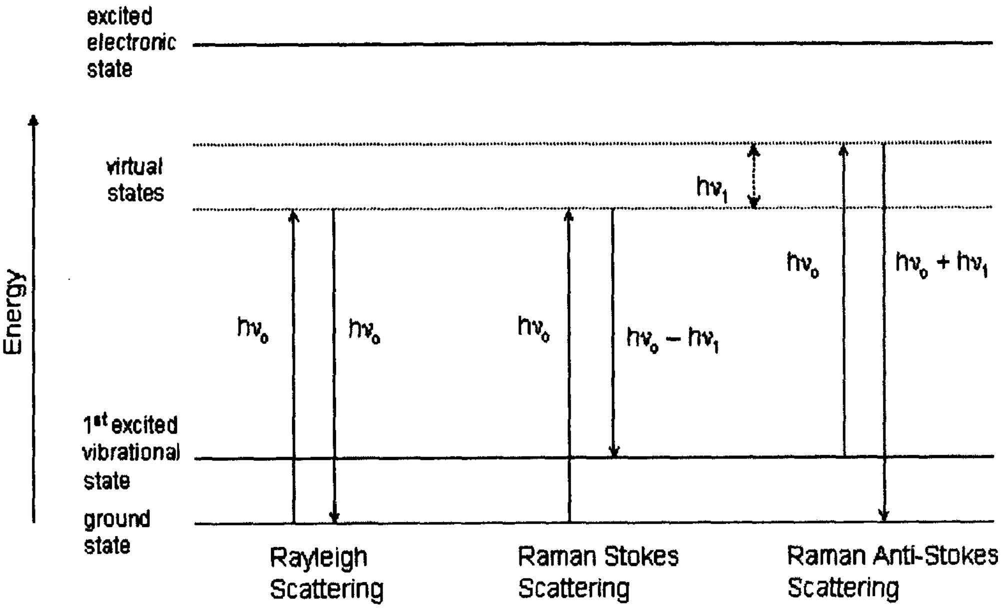

Figure 1.8 Origin of Rayleigh and Raman scattering (Reproduced with permission from Ref. 130)

All three scattering can be detected by Raman spectroscopy. However, Stokes lines are usually measured since they are more intense than anti-Stokes lines. This is due to the fact that the ground state is more populated than the first vibrational state, and thus produces a more intense signal.

Raman spectra are acquired by irradiating a sample with a powerful laser source, and the scattered radiation is measured using a spectrometer. The oscillating electric field of the incoming light induces a polarization in the sample molecule, and this short-lived distortion of the electron cloud is indicated as the virtual state in Figure 1.8.

Raman microspectroscopy now is often used for many high-pressure studies. It is advantageous due to its higher spatial resolution which is important when the sample volume is small.[131] Zeolites usually exhibit very weak Raman signals; however, this can be particularly advantageous in the investigations of template-framework interactions because the weak background of the zeolites allows Raman scattering arising from the occluded species to be detected.[132]

IR spectroscopy is used as a complementary technique to Raman spectroscopy regarding the molecular structural information.[133] IR photons in IR spectroscopy[134] excite a molecule to various discrete vibrational modes upon absorption; monitoring the absorption leads to spectroscopic data since molecules have specific characteristic frequencies upon which they rotate and vibrate.

IR spectra of a large number of zeolites have been reported by Flanigen *et al.*,[135] who have observed many strong bands in the region 1200 – 200 cm^{-1}. They were able to assign these bands either to the vibration of the silica tetrahedra or to external linkages between these characteristic tetrahedra of individual zeolite structures.

The diamonds in the DAC are chosen appropriately to have a transparency to infrared radiation and thus allow one to observe the changes caused by the pressure. Fourier transform (FT) IR spectroscopy[136] is a important tool for investigations of high-pressure systems since it avoids the contradictory requirements of small sample and large radiation-interacting volumes by providing high sensitivity and dynamic range.

IR and Raman active vibration modes can be predicted according to the selection rules. A vibration is IR-active if there occurs a change in the molecule's dipole moment during vibration, and it is Raman-active if there occurs a change in the polarizability of the molecule during vibration.

1.4.4 Powder X-ray Diffraction (XRD)

1.4.4.1 General Principles of XRD

XRD is the most widely used and least ambiguous technique to determine the long-range ordering and the phase purity of different samples and provides the most direct information on material structures. Due to the micro-crystalline nature of most molecular sieves, structure determinations are often limited to powder samples.[137, 138]

X-rays interact with electrons; when an X-ray beam strikes a material it is scattered in various directions by the electron clouds of the atoms. If the wavelength of the X-rays is comparable to the separation between atoms, interference can occur. Interference maxima and minima will result if the scattering centers are in an ordered array, such as atoms in a crystalline solid. The periodicity of the electron density in a crystal leads to coherent scattering of the X-ray and gives rise to a 'diffraction pattern' in a similar manner to the diffraction patterns obtained from the interaction of optical light with diffraction grating (Figure 1.9). For a XRD pattern, each reflection observed at a given angle 2θ, measured at wavelength λ with certain order of reflection n, is related to lattice planes with a distance d and an orientation indicated by the Millers indices *hkl* as described by the Bragg equation:[139]

$$2d_{hkl} sin\theta = n\lambda \qquad \textbf{(Equation 1.2)}$$

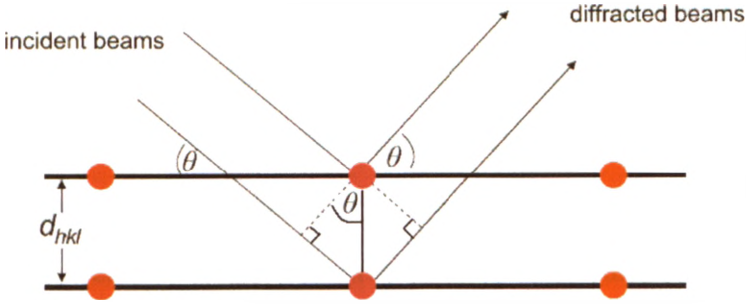

Figure 1.9 Deriving Bragg equation using the reflection geometry (Reproduced with permission from Ref. 130)

1.4.4.2 XRD with Synchrotron Radiation

Synchrotron radiation (SR) is the electromagnetic radiation emitted when charged particles, such as electrons or positrons, traveling at relativistic speeds which approach the speed of light follows a curved path with large radius. Electron accelerators that confine these relativistic electrons in the circular orbit are known as storage rings and synchrotron light sources. For high-energy electrons traveling in the magnetic fields (to accelerate the traveling electrons) of storage rings, this radiation is extremely intense over a wide range of photon energies extending from the broad spectral range. As a result, the SR is a powerful tool for basic and applied studies in biology, chemistry, physics, materials, geology, especially for studying micron-sized samples at high pressures while the conventional sources are limited only to low pressures, low spatial resolution, and very long measurement times.[140]

For monochromatic radiation (radiation with a fixed λ), maxima in the scattered intensity are observed at some discrete values of $2\theta_{hkl}$ corresponding to the lattice spacing. Such synchrotron geometry is called angle dispersive X-ray diffraction (ADXRD).[141]

Developments in the DAC techniques have strongly promoted the widespread application of XRD to solids under pressures. With this technique, lattice parameters and structural changes are studied almost routinely in polycrystalline solids at ambient temperatures and at low pressures in some laboratories. However, under high pressures, due to the constraints of bulk anvils and small sample size, XRD can only be performed with very intense high-energy X-ray beams which cannot be achieved in local laboratories. The extraordinary properties of modern synchrotron radiation source thus allow the perfect application of XRD in high-pressure studies.

1.4.5 Scanning Electron Microscopy (SEM)

SEM is a type of electron microscope that uses a beam of highly energetic electrons which are generated by electron gun to investigate objects on a very fine (nanometer) scale. The electrons interact with the sample producing signals that contain the information about the surface topography, morphology and composition of the sample.[142]

When the electrons of the beam strike the surface of the specimen and interact with the sample on or near its surface, secondary electrons and back-scattered electrons that come from the sample surface are detected by the SEM detectors. In the primary detection mode, SEM can produce very high-resolution images of the surface of an ideal sample, revealing surface details about 1 to 7 nm in size. Due to the way these images are created, SEM micrographs have a very large depth of focus yielding a characteristic three-dimensional appearance useful for understanding the surface structure of a sample.

1.4.6 Solid-State Nuclear Magnetic Resonance (SS-NMR)

The first NMR[143-145] signal was detected early in 1938 in a molecular beam, and the first studies of NMR in bulk materials were carried out about eight years later. Over the following decades, NMR has grown from an interesting and important study of a physical phenomenon to an indispensable technique in a very wide variety of fields. NMR deals with the interactions of the nuclear spins of atoms with external magnetic field. These interactions provide much information about local magnetic environments of nuclei, from which the information on local structure and dynamics can be obtained. In organic chemistry, solution NMR is arguably one of the most important tools for the elucidation of molecular structures. In addition, there are dynamic as well as static aspects of solid-state structures and SS-NMR can be used to study the motions of molecules in solids which may be related to their mechanical, electronic and other physical properties.

However, the less initial use of SS-NMR than solution NMR was due to the inherent lack of resolution in SS-NMR spectra. The major difference between solution and solid-state NMR lies in the fact that molecules are free to diffuse and tumble isotropically in solution, however, the structure is much more rigid and experiences much less motion in solid state. Due to the fast and isotropic motion of the molecules in solution state, many of the orientation-dependent nuclear spin interactions are averaged, resulting in narrow and highly resolved signals. On the other hand, these orientation dependent nuclear spin interactions are not averaged in the solid due to the relatively fixed orientations of the molecules, often leading to broad and featureless NMR spectra.

High resolution SS-NMR can be obtained with the invention and development of new methods and techniques from which many line-broadening interactions are reduced or removed, resulting in solution-like narrow signals. Moreover, the anisotropic nuclear spin interactions which lead to featureless NMR signals usually have structure information and can be selectively re-introduced and observed by certain techniques. As a result, SS-NMR has the potential to give more structural information than solution NMR, especially for the amorphous and disordered solids where powder XRD may not show useful information.

The five main interactions of nuclear spins in an applied magnetic field in solid state are Zeeman, dipolar, chemical shift, spin-spin coupling and quadrupolar interactions. The SS-NMR spectrum of a powder sample contains broad lines resulting from many of these anisotropic interactions. The broad lines can be considerably narrowed if the sample is rapidly spun. Furthermore, if the sample is spun around an axis with an angle of 54.74°, the magic angle, with respect to the external magnetic field and the spinning rate of the sample is much greater than the magnitude of the interaction (in Hz), the anisotropic portions of the chemical shift and dipolar interactions, and the first-order quadrupolar anisotropy will disappear, resulting in significantly narrow lines at isotropic position.

As one of the most important NMR techniques, the magic angle spinning (MAS) is employed to show local information about the atoms involved in the formation of molecular sieves in the present project. From the MAS spectra of the $AlPO_4$-based materials, the number and relative intensities of the ^{31}P and ^{27}Al resonances directly reflect the numbers and occupancies of the crystallographically inequivalent P and Al sites in the asymmetric unit of the unit cell, which yield the information of the framework structures of these materials.

1.5 Motivation

Although many experimental and theoretical studies[27, 28] of zeolites have been focused on their behaviours under high temperature at ambient pressure, there exist only a few studies[19, 29-34, 36] of the behaviours of zeolites under external pressure, especially the pressure-induced amorphization effect. As mentioned earlier, the main reason is due to that it is difficult to achieve the demanded high-pressure conditions as well as the absence of effective analytical probes. As such, one goal of our research is to study the behaviour of completely siliceous zeolite ZSM-5 under high pressure by DAC technique with several modern *in situ* analytical methods: Raman, IR, XRD with synchrotron radiation and to check the morphology of the initial and recovered samples by SEM. Further, the different reversibility of phase transitions for this zeolite with and without template molecules inside the channels is also investigated, which may further explain the role of the encapsulated molecules in framework transformation under high-pressure conditions.

Compared to zeolites, there are only few studies[91, 92] focused on the $AlPO_4$-n molecular sieves crystallization mechanisms which are still not yet well understood due to the absence of ideal approach to probe their crystallization process. Thus, the other goal of our research is to use the DGC method, especially the SAC method to study the crystallization mechanism of the $AlPO_4$-16 molecular sieve. The critical intermediates during the crystallization process are characterized by the powder XRD and SS-NMR techniques.

1.6 References

[1]H. Van Bekkum, E. Flanigen, P. Jacobs and J. Jansen, *Introduction to Zeolite Science and Practice, 2nd Completely revised and Expanded Edition*, 2001.
[2]A. Dyer, *Introduction to zeolite molecular sieves*, John Wiley & Sons New York, NY, 1988.
[3]H. St.Claire-Deville, Compt. Rend. Séances Acad. Sci., 54 (1862) 324.
[4]R.M. Barrer, J. Chem. Soc., (1948) 2158.
[5]R.M. Milton, *US Patent* 2882243 (1959).
[6]R.M. Milton, ACS Symp. Ser., 398 (1989) 1.
[7]M.G. Clerici, Met. Oxide Catal., 2 (2009) 705.
[8]S.T. Wilson, B.M. Lok, C.A. Messina, T.R. Cannan and E.M. Flanigen, J. Am. Chem. Soc., 104 (1982) 1146.
[9]L. Beitone, J. Marrot, T. Loiseau, G. Ferey, M. Henry, C. Huguenard, A. Gansmuller and F. Taulelle, J. Am. Chem. Soc., 125 (2003) 1912.
[10]L.L. Koh, Y. Xu, H.B. Du and W.Q. Pang, Stud. Surf. Sci. Catal., 105A (1997) 373.
[11]C.M. Cardile, N.J. Tapp and N.B. Milestone, Zeolites, 10 (1990) 90.
[12]X. Song, J. Li, Y. Guo, Q. Pan, L. Gan, J. Yu and R. Xu, Inorg Chem, 48 (2009) 198.
[13]E.M. Flanigen, R.L. Patton and S.T. Wilson, Stud. Surf. Sci. Catal., 37 (1988) 13.
[14]L. Mishra, R. Prajapati and G. Govil, Natl. Acad. Sci. Lett. (India), 30 (2007) 197.
[15]A.U. Czaja, N. Trukhan and U. Muller, Chem. Soc. Rev., 38 (2009) 1284.
[16]P. Wright, *Microporous framework solids*, Royal Society of Chemistry, 2008.
[17]U. Mueller, M.M. Schubert and O.M. Yaghi, Handb. Heterog. Catal. (2nd Ed.), 1 (2008) 247.
[18]Website of the International Zeolite Association: http://www.iza-online.org/.
[19]G.N. Greaves, F. Meneau, F. Kargl, D. Ward, P. Holliman and F. Albergamo, J. Phys.: Condens. Matter, 19 (2007) 415102/1.

[20] J. Nagy, P. Bodart, I. Hannus and I. Kiricsi, *Synthesis, characterization and use of zeolitic microporous materials*, DecaGen Szeged-Szoreg, Hungary, 1998.

[21] R. Xu, *Chemistry of Zeolites and Related Porous Materials: Synthesis and Structure*, Wiley-Interscience, 2007.

[22] R. Boyle, *New Experiments Physico-Mechanicall, Touching the Spring of the Air and its Effects*, Printer for T Robinson, Oxford, UK, 1660.

[23] R.J. Hemley and H.K. Mao, Proc. Int. Sch. Phys. "Enrico Fermi", 147th (2002) 3.

[24] R.J. Hemley, Annu. Rev. Phys. Chem., 51 (2000) 763.

[25] H. Hochheimer, *Frontiers of high pressure research II: application of high pressure to low-dimensional novel electronic materials*, Kluwer Academic Publishers, 2001.

[26] R.J. Hemley and N.W. Ashcroft, Phys. Today, 51 (1998) 26.

[27] G.N. Greaves, F. Meneau and G. Sankar, Nucl. Instrum. Methods Phys. Res., Sect. B, 199 (2003) 98.

[28] M. Derewinski, M.J. Peltre, M. Briend, D. Barthomeuf and P.P. Man, J. Chem. Soc., Faraday Trans., 89 (1993) 1823.

[29] R.M. Hazen, Science, 219 (1983) 1065.

[30] J.S. Tse, D.D. Klug, J.A. Ripmeester, S. Desgrenlers and K. Lagarec, Nature, 369 (1994) 724.

[31] Y. Lee, J.A. Hriljac, T. Vogt, J.B. Parise, M.J. Edmondson, P.A. Anderson, D.R. Corbin and T. Nagai, J. Am. Chem. Soc., 123 (2001) 8418.

[32] Y. Lee, T. Vogt, J.A. Hriljac, J.B. Parise, J.C. Hanson and S.J. Kim, Nature, 420 (2002) 485.

[33] E.A. Havenga, Y. Huang and R.A. Secco, Materials Research Bulletin, 38 (2003) 381.

[34] S. Ori, S. Quartieri, G. Vezzalini and V. Dmitriev, Am. Mineral., 93 (2008) 53.

[35] R. Arletti, O. Ferro, S. Quartieri, A. Sani, G. Tabacchi and G. Vezzalini, American Mineralogist, 88 (2003) 1416.

[36] R.A. Secco, S.V. Goryainov and Y. Huang, Phys. Status Solidi B, 242 (2005) R73.

[37] J. Gulin Gonzalez, A. Dorta-Urra, P. Demontis and G.B. Suffritti, Microporous Mesoporous Mater., 123 (2009) 30.

[38] I.A. Belitsky, B.A. Fursenko, S.P. Gabuda, O.V. Kholdeev and Y.V. Seretkin, Phys. Chem. Miner., 18 (1992) 497.

[39] R.M. Hazen and L.W. Finger, Phase Transitions, 1 (1979) 1.

[40] P. Ballone, S. Quartieri, A. Sani and G. Vezzalini, Am. Mineral., 87 (2002) 1194.

[41] P. Comodi, G.D. Gatta and P.F. Zanazzi, Eur. J. Mineral., 14 (2002) 567.

[42] P. Comodi, G.D. Gatta and P.F. Zanazzi, Eur. J. Mineral., 13 (2001) 497.

[43] G. Vezzalini, S. Quartieri, A. Sani and D. Levy, Stud. Surf. Sci. Catal., 135 (2001) 1470.

[44] O. Oeckler, S. Werner, H. Schulz and P. Behrens, Koatsuryoku no Kagaku to Gijutsu, 7 (1998) 139.

[45] M. Colligan, P.M. Forster, A.K. Cheetham, Y. Lee, T. Vogt and J.A. Hriljac, J. Am. Chem. Soc., 126 (2004) 12015.

[46] G.D. Gatta and S.A. Wells, Phys. Chem. Miner., 33 (2006) 243.

[47] G.N. Greaves, F. Meneau, A. Sapelkin, L.M. Colyer, I. ap Gwynn, S. Wade and G. Sankar, Nat. Mater., 2 (2003) 622.

[48] Y. Lee, J.A. Hriljac, T. Vogt, J.B. Parise and G. Artioli, J. Am. Chem. Soc., 123 (2001) 12732.

[49] Y. Lee, H.H. Lee, D.R. Lee, T.J. Shin, J.-Y. Choi and C.-C. Kao, J. Am. Chem. Soc., 129 (2007) 4888.

[50] Y. Lee, T. Vogt, J.A. Hriljac, J.B. Parise and G. Artioli, J. Am. Chem. Soc., 124 (2002) 5466.

[51] Y. Lee, J.A. Hriljac, J.B. Parise and T. Vogt, Am. Mineral., 90 (2005) 252.

[52] Y. Lee, C.D. Martin, J.B. Parise, J.A. Hriljac and T. Vogt, Nano Letters, 4 (2004) 619.

[53] Y. Lee, C.-C. Kao, S.J. Kim, H.-H. Lee, D.R. Lee, T.J. Shin and J.-Y. Choi, Chem. Mater., 19 (2007) 6252.

[54] Y. Lee, J.A. Hriljac, S.J. Kim, J.C. Hanson and T. Vogt, J. Am. Chem. Soc., 125 (2003) 6036.

[55] Y. Lee, S.J. Kim, C.-C. Kao and T. Vogt, J. Am. Chem. Soc., 130 (2008) 2842.

[56] R.A. Secco, M. Rutter and Y. Huang, Technical Physics (Translation of Zhurnal Tekhnicheskoi Fiziki), 45 (2000) 1447.

[57] R.A. Secco and Y. Huang, Journal of Physics and Chemistry of Solids, 60 (1999) 999.

[58] O. Mishima, L.D. Calvert and E. Whalley, Nature, 310 (1984) 393.

[59] R.J. Hemley, A.P. Jephcoat, H.K. Mao, L.C. Ming and M.H. Manghnani, Nature, 334 (1988) 52.

[60] M.B. Kruger and R. Jeanloz, Science, 249 (1990) 647.

[61] J.H. Nguyen, M.B. Kruger and R. Jeanloz, Phys. Rev. Lett., 78 (1997) 1936.

[62] S.K. Deb, M. Wilding, M. Somayazulu and P.F. McMillan, Nature, 414 (2001) 528.

[63] S.M. Sharma and S.K. Sikka, Prog. Mater. Sci., 40 (1996) 1.

[64] M.D. Rutter, T. Uchida, R.A. Secco, Y. Huang and Y. Wang, Journal of Physics and Chemistry of Solids, 62 (2001) 599.

[65] J. Gulin-Gonzalez and G.B. Suffritti, Microporous Mesoporous Mater., 69 (2004) 127.

[66] S.V. Goryainov and M.B. Smirnov, Eur. J. Mineral., 13 (2001) 507.

[67] C. Sanchez-Valle, A.D. Lethbridge Zoe, V. Sinogeikin Stanislav, J. Williams Jennifer, I. Walton Richard, E. Evans Kenneth and D. Bass Jay, J Chem Phys, 128 (2008) 184503.

[68] J.S. Tse and D.D. Klug, Phys. Rev. Lett., 70 (1993) 174.

[69] I. Daniel, P. Gillet, P.F. McMillan, G. Wolf and M.A. Verhelst, J. Geophys. Res., [Solid Earth], 102 (1997) 10313.

[70] H. Xu, J. Zhang, Y. Zhao, G.D. Guthrie, D.D. Hickmott and A. Navrotsky, Am. Mineral., 92 (2007) 166.

[71] R.R. Winters, G.C. Serghiou and W.S. Hammack, Phys. Rev. B: Condens. Matter, 46 (1992) 2792.
[72] J. Zhang, Y. Zhao, H. Xu, M.V. Zelinskas, L. Wang, Y. Wang and T. Uchida, Chem. Mater., 17 (2005) 2817.
[73] M.H. Cohen, J. Iniguez and J.B. Neaton, J. Non-Cryst. Solids, 307-310 (2002) 602.
[74] Y. Huang, J. Mater. Chem., 8 (1998) 1067.
[75] Y. Huang and E.A. Havenga, Chem. Phys. Lett., 345 (2001) 65.
[76] F. Meneau and G.N. Greaves, Nucl. Instrum. Methods Phys. Res., Sect. B, 238 (2005) 70.
[77] G.N. Greaves, F. Meneau, O. Majerus, D.G. Jones and J. Taylor, Science, 308 (2005) 1299.
[78] M.C. Wilding, M. Wilson and P.F. McMillan, Chem. Soc. Rev., 35 (2006) 964.
[79] I. Peral and J. Iniguez, Phys. Rev. Lett., 97 (2006) 225502/1.
[80] E. Fois, A. Gamba, G. Tabacchi, R. Arletti, S. Quartieri and G. Vezzalini, Am. Mineral., 90 (2005) 28.
[81] C.S. Cundy and P.A. Cox, Microporous Mesoporous Mater., 82 (2005) 1.
[82] D. Grandjean, A.M. Beale, A.V. Petukhov and B.M. Weckhuysen, J. Am. Chem. Soc., 127 (2005) 14454.
[83] M.E. Davis, Stud. Surf. Sci. Catal., 97 (1995) 35.
[84] R.I. Walton, F. Millange, D. O'Hare, A.T. Davies, G. Sankar and C.R.A. Catlow, J. Phys. Chem. B, 105 (2001) 83.
[85] J. Warzywoda, R.D. Edelman and R.W. Thompson, Zeolites, 9 (1989) 187.
[86] R.W. Thompson, in *Modelling of structure and reactivity in zeolites,* C.R.A. Catlow; R.Vetrivel, Eds., Academic Press, London, 1992.
[87] G.T. Kerr, J. Phys. Chem., 70 (1966) 1047.
[88] B. Fahlke, P. Starke, V. Seefeld, W. Wieker and K.P. Wendlandt, Zeolites, 7 (1987) 209.
[89] C.D. Chang and A.T. Bell, Catal. Lett., 8 (1991) 305.
[90] J. Mullin, *Crystallization,* Butterworth-Heinemann Boston, 2001.
[91] R.J. Francis and D. O'Hare, J. Chem. Soc., Dalton Trans., (1998) 3133.
[92] H. He and J. Klinowski, J. Phys. Chem., 98 (1994) 1192.
[93] R.W. Thompson, Mol. Sieves, 1 (1998) 1.
[94] S. Oliver, A. Kuperman, A. Lough and G.A. Ozin, Chem. Mater., 8 (1996) 2391.
[95] M.H. Kim, H.X. Li and M.E. Davis, Microporous Mater., 1 (1993) 191.
[96] Y. Huang, B.A. Demko and C.W. Kirby, Chem. Mater., 15 (2003) 2437.
[97] Y. Huang, R. Richer and C.W. Kirby, J. Phys. Chem. B, 107 (2003) 1326.
[98] S. Oliver, A. Kuperman and G.A. Ozin, Angew. Chem., Int. Ed., 37 (1998) 46.
[99] M.E. Davis and R.F. Lobo, Chem. Mater., 4 (1992) 756.
[100] B.M. Weckhuysen, D. Baetens and R.A. Schoonheydt, Angew. Chem., Int. Ed., 39 (2000) 3419.

[101]M. Haouas, C. Gerardin, F. Taulelle, C. Estournes, T. Loiseau and G. Ferey, J. Chim. Phys. Phys.-Chim. Biol., 95 (1998) 302.

[102]M. Dong, G. Wang, Z. Qin, J. Wang, T. Liu, Y. Xie and T. Hu, Stud. Surf. Sci. Catal., 170A (2007) 771.

[103]G. Muncaster, A.T. Davies, G. Sankar, R.A. Catlow, J.M. Thomas, S.L. Colston, P. Barnes, R.I. Walton and D. O'Hare, Phys. Chem. Chem. Phys., 2 (2000) 3523.

[104]W. Xu, J. Dong, J. Li, J. Li and F. Wu, J. Chem. Soc., Chem. Commun., (1990) 755.

[105]M. Matsukata, M. Ogura, T. Osaki, P. Raja, H.P. Rao, M. Nomura and E. Kikuchi, Top. Catal., 9 (1999) 77.

[106]M. Bandyopadhyay, R. Bandyopadhyay, Y. Kubota and Y. Sugi, Chem. Lett., (2000) 1024.

[107]B. Chen and Y. Huang, J. Am. Chem. Soc., 128 (2006) 6437.

[108]B. Chen and Y. Huang, J. Phys. Chem. C, 111 (2007) 15236.

[109]C.E. Weir, E.R. Lippincott, A. Van Val-kenburg and E.N. Bunting, J. Res. Natl. Bur. Stand., Sect. A, 63A (1959) 55.

[110]S. Block and G. Piermarini, Phys. Today, 29 (1976) 44.

[111]A. Jayaraman, Rev. Mod. Phys., 55 (1983) 65.

[112]K. Lonsdale and H. Smith, Nature, 148 (1941) 112.

[113]M.A. Washington and H.Z. Cummins, Phys. Rev. B, 15 (1977) 5840.

[114]A.T. Collins, Physica B (Amsterdam), 185 (1993) 284.

[115]W. Holzapfel and N. Isaacs, *High Pressure Techniques in Chemistry and Physics: A Practical Approach*, Oxford University Press, USA, 1997.

[116]J. Ferraro and E. Skelton, Phys. Today, 39 (1986).

[117]G.J. Piermarini, S. Block and J.D. Barnett, J. Appl. Phys., 44 (1973) 5377.

[118]G.D. Gatta, P. Comodi and P.F. Zanazzi, Microporous Mesoporous Mater., 61 (2003) 105.

[119]A.K. Kleppe, A.P. Jephcoat and J.R. Smyth, Am. Mineral., 91 (2006) 1102.

[120]A.P. Jephcoat, H.K. Mao and P.M. Bell, J. Geophys. Res., B, 91 (1986) 4677.

[121]S.H. Shim, T.S. Duffy and G. Shen, Phys. Earth Planet. Inter., 120 (2000) 327.

[122]R. Forman, G. Piermarini, J. Barnett and S. Block, Science, 176 (1972) 284.

[123]H.K. Mao, J. Xu and P.M. Bell, J. Geophys. Res., B, 91 (1986) 4673.

[124]G.J. Piermarini, S. Block, J.D. Barnett and R.A. Forman, J. Appl. Phys., 46 (1975) 2774.

[125]J.A. Xu, H.K. Mao and P.M. Bell, Science, 232 (1986) 1404.

[126]R.J. Hemley, C.S. Zha, A.P. Jephcoat, H.K. Mao, L.W. Finger and D.E. Cox, Phys. Rev. B: Condens. Matter, 39 (1989) 11820.

[127]J.R. Ferraro, Coord. Chem. Rev., 29 (1979) 1.

[128]P.K. Dutta and M. Puri, J. Phys. Chem., 91 (1987) 4329.

[129]D. Gardiner, P. Graves and H. Bowley, *Practical Raman Spectroscopy*, Springer-Verlag New York, 1989.

[130]J.A. Lee, M. Sc. thesis, University of Western Ontario (2008).

[131]A. Jayaraman and S.K. Sharma, Curr. Sci., 74 (1998) 308.

[132]Y. Huang, J. Am. Chem. Soc., 118 (1996) 7233.

[133]C.L. Angell, J. Phys. Chem., 77 (1973) 222.

[134]N. Colthup, L. Daly and S. Wiberley, *Introduction to infrared and Raman spectroscopy*, Academic press Boston, 1964.

[135]E.M. Flanigen, H. Khatami and H.A. Szymanski, Advan. Chem. Ser., 101 (1971) 201.

[136]J. Ferraro and L. Basile, *Fourier transform infrared spectroscopy*, Academic press: New York, 1978.

[137]R. Jenkins and R. Snyder, *Introduction to X-ray powder diffractometry*, Wiley. New York. US, 1996.

[138]V. Pecharsky and P. Zavalij, *Fundamentals of Powder Diffraction and Structural Characterization of Materials*, Kluwer Academic Publishers, 2003.

[139]W.L. Bragg, Proc. R. Soc. London, Ser. A, 89 (1913) 248.

[140]K. Wille, *The physics of particle accelerators: an introduction*, Oxford University Press, 2000.

[141]A. Clearfield, Reibenspies, Joseph Henry, Bhuvanesh, Nattami., *Principles and applications of powder diffraction* Chichester, UK ; Ames, Iowa : John Wiley and Sons, Ltd., 2008.

[142]J. Goldstein, D. Newbury, P. Echlin, D. Joy, C. Fiori and E. Lifshin, *Scanning electron microspcopy and X-ray analysis. A text for biologists, material scientists and geologists*, Plenum Press: New York & London, 1981.

[143]E. Becker, *High resolution NMR: theory and chemical applications*, Academic Press, 1999.

[144]E. Ebsworth, S. Cradock and D. Rankin, *Structural methods in inorganic chemistry*, CRC Press Boca Raton, Fla, 1991.

[145]C. Fyfe, *Solid state NMR for chemists*, CFC Press Guelph, 1983.

Chapter 2 Experimental Details

2.1 Commercial Reagents Used

The reagents 99% hexamethyleneimine (HEX), 98% tetrapropylammonium bromide (TPAB), and 30 wt% colloidal silica (LUDOX) were purchased from Aldrich Chemical Co. and used as received without any further purification. Phosphoric acid (85%) and sodium hydroxide (NaOH, 97%) were purchased and used as received from Caledon. The 65% Al_2O_3 (Catapal B) was purchased from Vista Chemical Company.

2.2 High-Pressure Techniques

2.2.1 Sample Synthesis

Completely siliceous ZSM-5 was prepared by the typical synthesis method carried out as follows: 0.020 L of 3.50 mol L^{-1} NaOH was added to 88 g of 30 wt% colloidal silica. After mixing for 15 minutes, 0.030 L of 0.86 mol L^{-1} TPAB, the template was added to the above solution. After stirring for 30 minutes, the resulting mixture was then transferred to a 0.125 L Teflon-lined stainless steel autoclave, and heated at a constant temperature of 150 ^{o}C for two weeks. The crystals were then washed with 4 L of distilled water to remove excess base, resulting in as-made siliceous ZSM-5. The calcined siliceous ZSM-5 was made by heating the as-made sample in a Muffle furnace at 550 ^{o}C for 3 hours to remove the template molecules. The samples were checked by XRD before use in high-pressure experiments.

2.2.2 Diamond Anvil Cell

Two different types of cells were used in the present experiment, each with a specific purpose. A diamond anvil cell (DAC) composed of two type I diamonds, with a culet size of 600 μm, was used for Raman studies; a diamond anvil cell composed of two type II diamonds, which has good transmission in the infrared region, with a culet size of 600 μm, was used for IR studies. High pressures up to 20 GPa could be achieved by the two types of cells. Stainless steel gaskets with thicknesses of 250 μm served as sample chambers and were pre-indented to approximately 100 and 50 μm via the Raman and IR cells used for the experiments respectively. Using an electric discharge machine, holes with 200 μm were drilled in the centre of the indentations. Pressure of the sample within the cell used is changed via tightening or loosening a symmetric four-screw system. The sample reaches equilibrium almost instantaneously upon the tightening or loosening of the screw-pairs while keeping the culets parallel to each other. Bevelled washers were used to apply a spring-like delivery of force while allowing for finer control.

2.2.3 The Raman System

The Raman experiments were carried out using a customized Raman micro-spectroscopy system (Figure 2.1). The 488 nm line of an argon ion laser was used as the excitation source (Coherent Innova 90C Series Ion Laser). The maximum power of the laser was approximately 3 W and appropriate filters were used to ensure that only a few milli-Watts of laser power is incident on the sample to minimize photo induced reactions and fluorescence. The system used a 0.500 m focal distance monochromator (SpectroPro-2500i, Acton Research Corporation) equipped with multiple gratings. The 1800 line/mm grating with a ± 0.1 cm^{-1} resolution was used in this experiment. The signal was detected by a charge-coupled device (CCD) (Spec-10 system, Princeton

Instrument) detector, which was cooled and locked at –120 °C using liquid nitrogen before each run. The instrument control and data acquisition were executed via WinSpec Software, by which pressures can be obtained directly from the position of the R_1 ruby fluorescence.[11] The system was calibrated using standard neon lines. With the calibration, the Raman system could achieve an uncertainty of ±1 cm^{-1}. All measurements were carried out at room temperature.

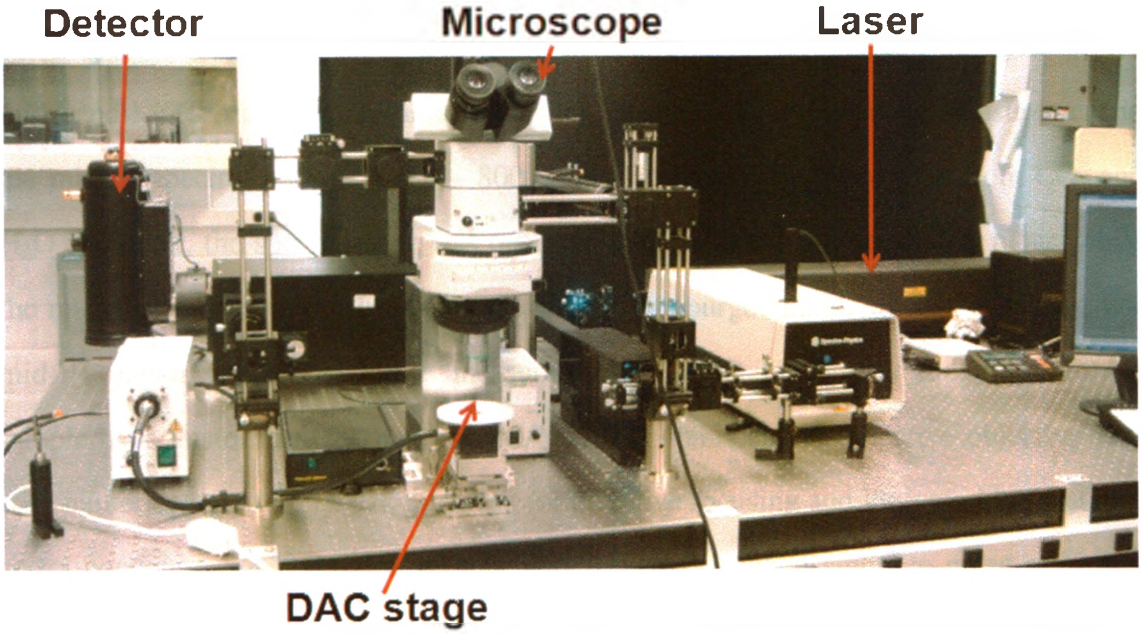

Figure 2.1 The Raman microscopy system used. The system features an argon laser, a microscope, a CCD detector and a DAC stage.

2.2.4 The FTIR System

Infrared experiments were performed using a custom-built infrared micro-spectroscopy system. The major component of this system includes a commercial FTIR spectrometer (a vacuum bench Vertex 80v model) from Bruker Optics Inc. and several customized IR microscopes as shown in Figure 2.2. Globar was used as the mid-IR source in the spectrometer. The spectrometer was equipped with a number of beam splitters (e.g. KBr for mid-IR) and detectors including a liquid nitrogen cooled mid-band MCT (mercury cadmium telluride) detector, allowing for the measurement in the mid-IR spectral region of 650 – 8000 cm^{-1}. To reduce the absorption from CO_2 and H_2O in the air, the spectrometer was operated in a vacuum of better than 5 mbar, while the microscope system outside the spectrometer was purged continuously by dry air. For mid-IR transmittance/absorbance measurements, the IR beam was focused onto the sample by a customized IR microscope, which contains an IR reflective objective lens with numerical aperture of 0.4, allowing for effective focusing and long working distance, and a condenser for collection of transmitted signal. A good signal-to-noise ratio was achieved using 1024 scans, with a resolution of 4 cm^{-1}. The thickness of the sample for IR measurement was carefully chosen to allow sufficient IR transmission measurements. A gasket was pre-indented to less than 50 μm and then filled with KBr (with Ruby chips inserted as pressure calibrant) before loading the sample to reduce the actual sample thickness. The reference spectrum, i.e., the IR absorption of diamond anvil together with KBr in the gasket at ambient pressure, was ratioed as background from each sample spectrum later to obtain the absorbance spectrum.

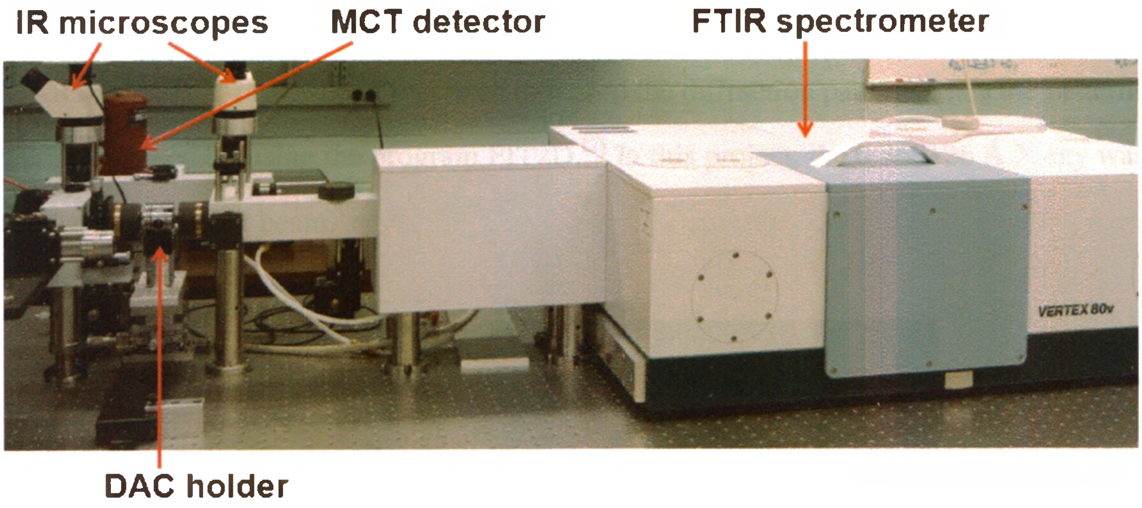

Figure 2.2 The FTIR system with an adjustable sample holder, customized IR microscopes, a MCT detector and a FTIR spectrometer (a vacuum bench Vertex 80v model)

2.2.5 Angle Dispersive X-ray Diffraction with Synchrotron Radiation

The angle dispersive X-ray diffraction (ADXRD) experiments were carried out at the high pressure collaborative access team (HPCAT), Advanced Photon Source (APS), Argonne National Laboratory.

An APS undulator type-A was used at an insertion device undulator beamline (16ID-B) at HPCAT, which provided a highly brilliant X-ray source of 2475 μm^2 in size and 36 μrad in divergence. With water cooled Si (220) crystals, the branching double-crystal monochromator (BDCM) provided a monochromatic beam to 16ID-B station with an energy range of 25 – 36 keV and energy resolution of 1×10^{-4} ΔE/E, which served the purpose well for most high-pressure XRD studies (Figure 2.3). To obtain a very intense and highly focused beam at sample position, a table top Kirkpatrick-Baez (KB) mirror system was used in 16ID-B, giving a focused spot size of 20 μm^2 at full width at half maximum (FWHM) with a flux at the focused spot of 0.5 – 1 × 10^{11} photons/s at 30 keV. A MAR165 CCD X-ray detector was used to record the diffraction patterns, then the patterns were integrated by using the program FIT2D.[2] In this project, the 0.369126 Å X-ray was used as the incident beam.

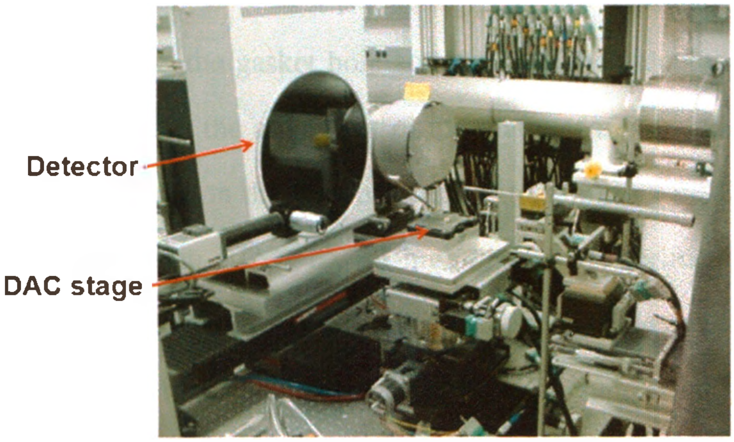

Figure 2.3 ADXRD set up at 16ID-B with MAR CCD detector and DAC stage labeled.

2.2.6 The SEM System

SEM images were collected using a Leo/Zesis 1540XB FIB/SEM Crossbeam. The crossbeam combined a high resolution SEM for imaging with a focused ion beam (FIB) for micromachining by sputter milling with a sub-100 nm lateral resolution. The spatial resolution of the images can be as small as 1 nm depending on the materials. The SEM system has two chambers: a delivery chamber and a specimen chamber. The delivery chamber, which has a small volume was used to pre-vacuum the sample before the sample was delivered to the specimen chamber, which protects the emission tip from repeated vacuuming. Upon evacuation, the sample was delivered to the specimen chamber and SEM images were collected. Our samples recovered from decompression were fixed to the sample stage and taken into the delivery chamber with a 10^{-6} – 10^{-7}

mbar vacuum. SEM images were collected under different magnifications from nm to μm.

2.2.7 Experimental Procedures

The sample loaded in the hole of a pre-indented gasket with 200 μm in diameter. Prior to each sample loading, the gasket hole and the diamond culets were cleaned with acetone and checked to ensure the alignment of the diamonds. Since the behaviour of a zeolite under pressure depends on the type of pressure-transmitting medium (PTM) used (penetrating or non-penetrating PTM[2-4]), all high-pressure experiments we performed were without PTM in order to avoid any possible interactions between the sample and the PTM which may enter the channels of the sample during compression. A tiny ruby ball was placed inside the hole of the gasket with sample to calibrate the pressure. Then the sample was investigated using Raman and FTIR spectroscopy, and XRD with synchrotron radiation.

Upon loading the sample, *in situ* Raman and FTIR spectra were measured carefully for each pressurized step. A minimum of 15 min was allowed to ensure equilibrium in the cell upon increasing or decreasing of the pressure. At each pressure, the Raman spectrum of the sample was collected for 1 min using 1800 line/mm grating. For FTIR measurements, the sample was diluted with pre-dried KBr, which was transparent and showed no peaks in the mid-IR region. At each pressure, the FTIR spectrum of the sample was collected for 1024 scans. The Raman data were collected using the Winspec software; this program was also used to measure the pressure of the sample at each respective step. The IR data were collected using the Brucker software OPUS.

X-ray diffraction measurements were carried out by Dr. Yang Song and Ms. Zhaohui Dong at 16ID-B in APS with a wavelength of 0.369126 Å. For each pressurized step, the pressure was measured using the ruby R_1 fluorescence line. XRD patterns were collected for 15 minutes in order to get clear images. The two-dimensional diffraction images were integrated using the FIT2D software to be converted to standard 1-D diffraction profiles.

All the data from the high-pressure experiments mentioned above were converted, plotted and further analyzed using the software Origin Lab.

After decompression, the recovered samples in the gaskets were carefully removed from the DAC and imaged by SEM using the 1540 Leo FIB/SEM beam.

2.3 Dry Gel Conversion Techniques

2.3.1 Sample Preparation

In the present study, $AlPO_4$-16 was synthesized by SAC method and the initial gel molar composition is 1.0 Al_2O_3: 1.0 P_2O_5: 1.0 HEX: 45 H_2O. In a typical procedure, the appropriate amount of 65% Al_2O_3 was mixed with distilled water and stirred at room temperature for 30 minutes, followed by dropwise addition of 85% phosphoric acid with continuous stirring for 90 minutes. Afterwards, HEX was added dropwise to the above mixture and the resultant gel was stirred for homogeneity for 3 hours.[5] The gel was then placed into several weighing boats and allowed to air dry until a yellowish solid dry gel formed. This was then ground into a fine powder and sealed in glass vials for analysis. A series of dry gel samples was prepared typically by placing 1.0 g of the initial dry gel powder into a series of small Teflon (polytetrafluoroethene) cups (20 mm i.d. × 24 mm) with Teflon holders (Figure 2.4). Each cup was placed into a Teflon-lined autoclave, and 0.3 g distilled water was placed at the bottom of each autoclave so that the dry gel in cup never came into direct contact with external water. Crystallization was then carried out under static conditions at different temperatures in an oven. After various heating times, the autoclaves were taken out of the oven and the reactions were quenched by cold water.

The solid samples were then air dried, ground into a fine powder, and stored in tightly sealed vials for analysis.

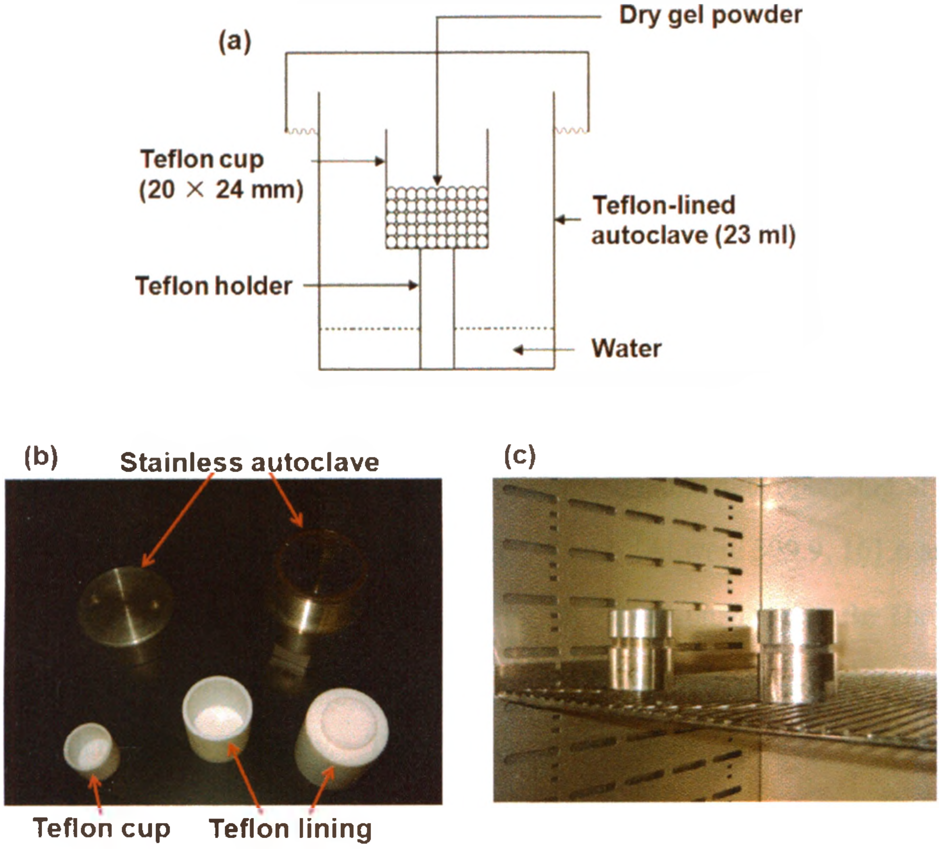

Figure 2.4 (a) Schematic diagram of $AlPO_4$-16 synthesis by SAC method; (b) Picture of stainless autoclave, Teflon cup and Teflon lining used in this thesis; (c) Parallel samples were heated in an oven.

Specific samples were further treated by certain post-synthesis treatments. Some samples were calcined in the Muffle furnace at 550 °C for varying periods of time. Some samples were washed using distilled water by a centrifuge and then dried in air. For comparison, some samples were washed by distilled water in a beaker and then dried in the same beaker in air without isolation from the liquid phase. This ensured that no solid particles would be washed away.

2.3.2 Characterization Methods

2.3.2.1 Powder X-ray Diffraction Measurements

Powder XRD patterns were recorded on a Rigaku diffractometer using Co Kα radiation (λ = 1.7902 Å). The XRD patterns were recorded from $5° \leq 2\theta \leq 65°$ at a scan rate of 10°/min with a step-size of 0.02°.

2.3.2.2 Solid-State NMR Measurements

All NMR experiments were carried out on a Varian/Chemagnetics Infinityplus 400 WB spectrometer equipped with three radiofrequency (rf) channels operating at the field strength of 9.4 T. The Larmor frequencies of ^{1}H, ^{31}P and ^{27}Al were 399.9, 161.6 and 104.1 MHz, respectively. The magic angle was set using the ^{79}Br resonance of KBr. The shifts of ^{31}P, ^{27}Al and ^{1}H were referenced to 85% H_3PO_4, 1M $Al(NO_3)_3$ aqueous solution and TMS (tetramethylsilane), respectively. The NMR probe used in this project is the Varian/Chemagnetics 5.0-mm triple tuned T3 MAS probe. Pulses of 2 μs ($\pi/6$ pulse) and 1.5 μs ($\pi/2$) were used for ^{31}P and ^{27}Al, respectively. The recycle delay was 120 s for ^{31}P and 500 ms for ^{27}Al. The spin rate used in all MAS experiments was 10 kHz.

2.4 References

[1] H.K. Mao, J. Xu and P.M. Bell, J. Geophys. Res., B, 91 (1986) 4673.
[2] G.D. Gatta, P. Comodi, P.F. Zanazzi and T.B. Ballaran, Am. Mineral., 90 (2005) 645.
[3] M. Colligan, P.M. Forster, A.K. Cheetham, Y. Lee, T. Vogt and J.A. Hriljac, J. Am. Chem. Soc., 126 (2004) 12015.
[4] R.M. Hazen, Science, 219 (1983) 1065.
[5] R. Bandyopadhyay, M. Bandyopadhyay, Y. Kubota and Y. Sugi, J. Porous Mater., 9 (2002) 83.

Chapter 3 A Study of the Behaviour of Completely Siliceous Zeolite ZSM-5 under High Pressures

3.1 Introduction

Zeolites are microporous aluminosilicates with well defined channels and cavities. They comprise corner-sharing AlO_4 and SiO_4 tetrahedral units connected via bridging oxygens to form a three-dimensional network. Each AlO_4 tetrahedron in the framework bears a net negative charge which is balanced by an extra-framework cation, whereas pure silica frameworks are electrically neutral.[1] Based on their unique structures and physicochemical properties, they are widely used as ion-exchangers, molecular sieves, sorbents and catalysts in many industrial fields (e.g. petrochemistry, agronomy, radioactive waste isolation, wastewater and auto-exhaust treatments, medical applications).[2-4]

The stability of zeolites is crucial to their wide range of applications. Many experimental and theoretical studies have been concentrated on their thermal stability. On the contrary, their behaviours under external high pressures have received much less attention, probably due to experimental difficulties and limits. Even with the great improvements of high-pressure apparatus and increasing availability of synchrotron X-ray sources, only a handful of the many zeolite topologies have been studied under high pressures so far.[5-14] Most previous work has been on: (1) pressure-induced structural transformations between crystalline phases;[15] (2) pressure-induced hydration (PIH) and the compressibility of zeolites affected by non-framework species;[16] (3) the effect of pressure on ionic conductivity of zeolites;[17] (4) pressure-induced amorphization (PIA) and the reversibility of this process upon decompression.[18]

PIA, which is the formation of an amorphous phase within a solid state by applying external pressure, has received much attention since its initial discovery on hexagonal ice.[19] The phenomenon has been found to occur in various materials, especially in framework silicates like SiO_2 (quartz and coesite)[20, 21] and feldspars.[22] Thus, it is believed that the pressure-induced amorphous state is a universal property of condensed materials.[23] The nature of the PIA process has been the subject of many experimental and theoretical studies by various analytical probes which are sensitive to different length scales: *in situ* X-ray diffraction (XRD), Raman, Infrared (IR) and Brillouin spectroscopies, and high-resolution scanning electron microscopy (SEM) of the recovered samples.[9, 24-28]

PIA and the reversibility of this process upon decompression of zeolites have been investigated experimentally and theoretically in the recent decade.[9, 24, 25, 29-31] Some pressure-induced amorphous phases of certain zeolites have been found to partially or totally revert back to the initial zeolite's crystalline structure upon decompression to ambient pressure.[6, 18, 24, 32] The occurrence of such reversibility may depend on the maximum pressure applied, the time under compression and the existence of the non-deformable units (such as hydrated charged balancing cations and template molecules in the framework) driving the reversible transformation.[6, 18, 32]

Recently, the interest in the PIA of zeolites has been renewed by Greaves and co-workers.[11, 27, 33, 34] Their results showed that a zeolite may contain two different pressure-induced amorphous phases: a low density amorphous (LDA) phase of low entropy (low structure disorder), and a high density amorphous (HDA) phase with higher entropy. This phenomenon which has been proposed to occur in diverse systems such as silica[35], water[36] and alumina[37] is called polyamorphism: occurrence of more than one amorphous phase with the same chemical composition but different densities and entropies.[38] Moreover, the zeolite topology (or connectivity of T-O-T linkages) existing in the crystalline state is found to be preserved in the LDA phase, but lost in the HDA phase.[39] Some authors suggested that amorphization will be reversible in the former phase and irreversible in the latter.[30] These results together with other studies show that the reversibility of PIA largely depends on the zeolite composition.[13, 18, 25, 40]

Zeolite ZSM-5 is a representative member of a class of high-silica zeolites which was first invented by Mobil Oil Company, and it is an important zeolite which has traditional applications in adsorption and catalysis[41-43] and emerging applications such as thin films and membranes.[44, 45] Moreover, it is often used as a model system in studies of zeolite properties.[46] The completely siliceous zeolite ZSM-5 which is also known as Silicalite-1(structure type MFI) is a synthetic zeolite that has a framework only consisting of SiO_4 tetrahedral units. The framework is neutral and hydrophobic, and without cations or zeolitic water molecules present.

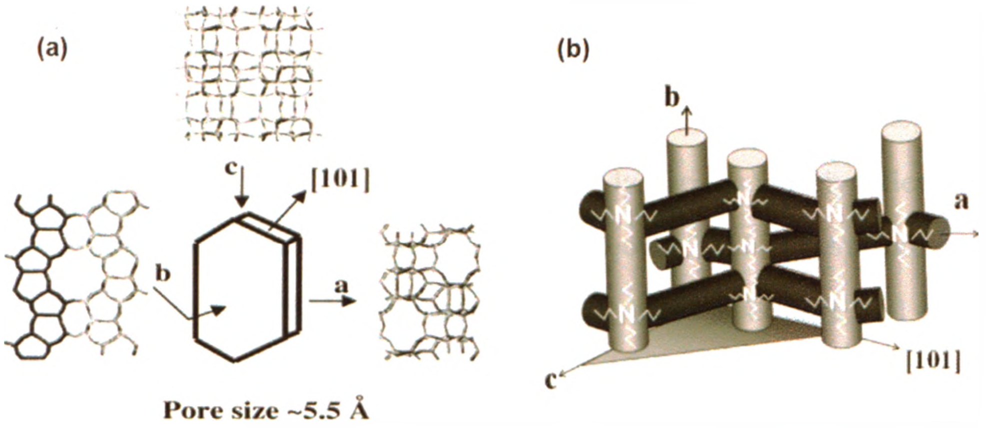

Figure 3.1 (a) A schematic identifying the crystal faces and dimensions along with the corresponding framework projections. The pentasil chain is highlighted. (b) Schematic of the pore structure of TPA-MFI with the TPA^+ located at channel intersections. (Adapted from Ref. 47)

The MFI structure is described as a combination of two interconnected channel systems (Figure 3.1). The silicate framework forms sinusoidal 10-membered rings (10MR) channels along the direction of the *a*-axis, interconnected with straight 10MR channels that run down the *b*-axis. A tortuous pore path is present along the *c*-axis. The MFI framework model can be built by connecting pentasil silicate chains.[47] ZSM-5 is usually synthesized in the presence of tetrapropylammonium cations (TPA^+) and the template ions are found in the intersections of the two channel systems. The as-made ZSM-5 belongs to the orthorhombic crystal system with the Pnma space group, and the calcined ZSM-5 obtained by removal of template molecules at high temperature in air ('calcination') belongs to the monoclinic crystal system with the $P2_1/n$ space group.

The behaviour of the completely siliceous zeolite ZSM-5 under high pressures at room temperature was investigated in a previous study by Liu *et al.*[48] The zeolite was synthesized under hydrothermal methods using tetrapropylammonium bromide (TPAB) as a template which is the same as the present study. After removal of the adsorbed water and water of crystallization, the anhydrous ZSM-5 was pressurized to 4.0 GPa using a belt-type high-pressure apparatus and the pressure was released after 20 minutes. The recovered sample was then characterized by powder XRD and thermogravimetric-differential thermal analysis (TG-DTA). In their study, the completely siliceous zeolite ZSM-5 is directly and irreversibly transformed into zeolite ZSM-11 (structure type MEL) which is an intergrowth of ZSM-5 by skeletal rearrangement at 4.0 GPa, and the ZSM-11 is stable up to a pressure of 8.0 GPa.

Since their study did not use any *in situ* technique, they could not show any detailed changes in the zeolite's structure during the compression and decompression. Moreover, their study was limited to 8.0 GPa, the information on the behaviour of this zeolite at high pressures above 8.0 GPa was not obtained.

The aim of our research is to study the behaviour of completely siliceous zeolite ZSM-5 under high pressure with diamond anvil cell (DAC) technique, using several *in situ* analytical methods including Raman, IR spectroscopies and XRD with synchrotron radiation. SEM was also used to examine the morphology of the initial and recovered samples. Our attention is also focused on the differences in the reversibility of the amorphization between the ZSM-5 samples with and without template molecules. The results may further explain the role of the encapsulated organic molecules in framework transformation under high pressures.

3.2 Experimental Section

The detailed procedures of sample preparation and characterizations are described in chapter 2 (pages 35 – 42).

3.3 Results and Discussion

3.3.1 High-Pressure Study of As-made Siliceous Zeolite ZSM-5

3.3.1.1 Raman Spectra of As-made Siliceous ZSM-5

3.3.1.1.1 Raman Spectrum of As-made Siliceous ZSM-5 at Ambient Pressure

Vibrational spectroscopy was used to provide complementary information regarding the effects of pressure on short-range ordering and local structures of this zeolite. The Raman spectrum of this material at ambient conditions is shown in Figure 3.2, which is consistent with the spectra reported by Bremard [49] and Bartlett [50]. All the peaks labeled in Figure 3.2 can be observed under high pressure and are assigned in Table 3.1 based on the references.[49, 50] In Figure 3.2, only the ν_2 mode belongs to the ZSM-5 framework due to the Si-O-Si bending vibrations of five-membered rings (5MR), whereas other modes all originate from the occluded TPA$^+$ cations.

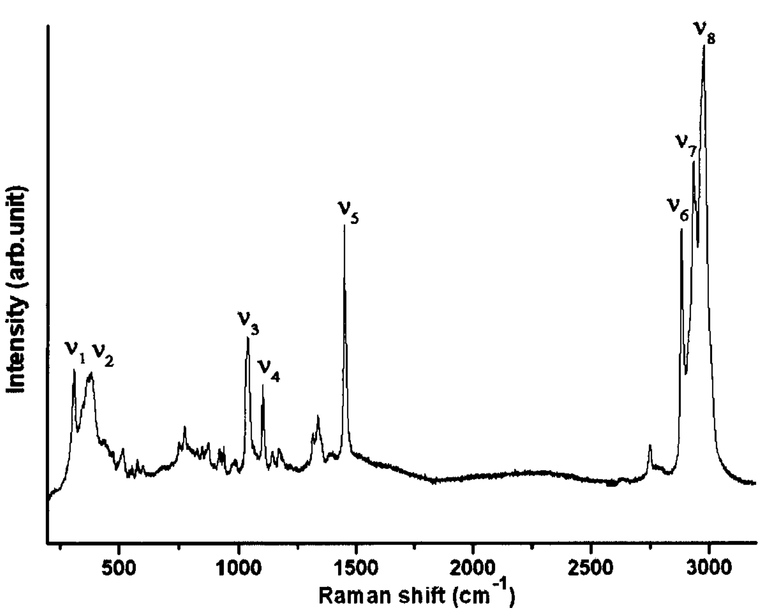

Figure 3.2 Raman spectrum of as-made siliceous ZSM-5 at ambient conditions with the 488 nm excitation line.

Table 3.1 Raman modes (cm^{-1}) of as-made siliceous ZSM-5 sample containing TPA^+ cations

modes	ZSM-5[b]	ZSM-5	Assignments
ν_1	310	309[c]	TPA^+ cations skeletal deformation
ν_2	380	382[c]	δ(Si-O-Si) bending of 5MR
ν_3	1039	1036[a]	ν_{as}(C-C) stretching
ν_4	1101	1101[a]	CH_2 rocking
ν_5	1454	1455[a]	HCH deformation
ν_6	2883	2881[a]	ν(C-H) stretching
ν_7	2935	2933[a]	ν(C-H) stretching
ν_8	2979	2975[a]	ν(C-H) stretching

[a] Ref. 50; [b] this work; [c] Ref. 49

3.3.1.1.2 Raman Spectra of As-made Siliceous ZSM-5 on Compression

The *in situ* Raman spectra of as-made siliceous ZSM-5 were acquired as a function of pressure up to 16.3 GPa at room temperature. The selected spectra in the region of 200 – 1000 cm^{-1} are shown in Figure 3.3. Upon compression, this material's structure undergoes modifications that are visible in the Raman spectra. From ambient pressure up to 2.9 GPa, the intensities of all the original peaks gradually decrease with increasing pressure, especially the ν_2 peak which becomes a broad hump at 2.9 GPa, suggesting that the framework of the as-made ZSM-5 gradually deforms under high pressure and the PIA starts at about 3 GPa, since the appearance of a low intensity broad spectrum can be considered as the direct evidence of amorphization.[51] At 3.8 GPa, a new broad band ν_A appears at about 491 cm^{-1}, which may already exists at 2.9 GPa. The appearance of this new band confirms that an amorphous phase shows up at about 3 GPa. Under 3.8 GPa, the intensity of the ν_1 mode which is associated with the TPA$^+$ cations gradually decreases with increasing pressure.

The new band ν_A can be detected clearly at 4.8 GPa, and another new broad band ν_B at 588 cm^{-1} can be seen at the same pressure. From 4.8 to 7.6 GPa, the ν_A gradually becomes the most prominent band in the spectra. This is accompanied by the gradual disappearance of the ν_2 band due to the zeolite framework. All the bands shift to higher frequencies with increasing pressure. Above 7.6 GPa, the ν_2 mode is almost invisible, which means the framework of as-made ZSM-5 collapses, suggesting another stage of amorphization. From 8.4 to 12.5 GPa, we cannot observe significant spectral changes except a further decrease in the intensity of the ν_1 mode with increasing pressure.

At 13.7 GPa, all the modes due to the as-made ZSM-5 originally observed at ambient conditions vanish, and the intensities of the two new bands (ν_A and ν_B) decrease largely and almost disappear in the baseline, which indicates this zeolite totally transforms to amorphous materials and the PIA finishes at around this pressure since the spectra acquired between 13.7 and 16.3 GPa are almost the same.

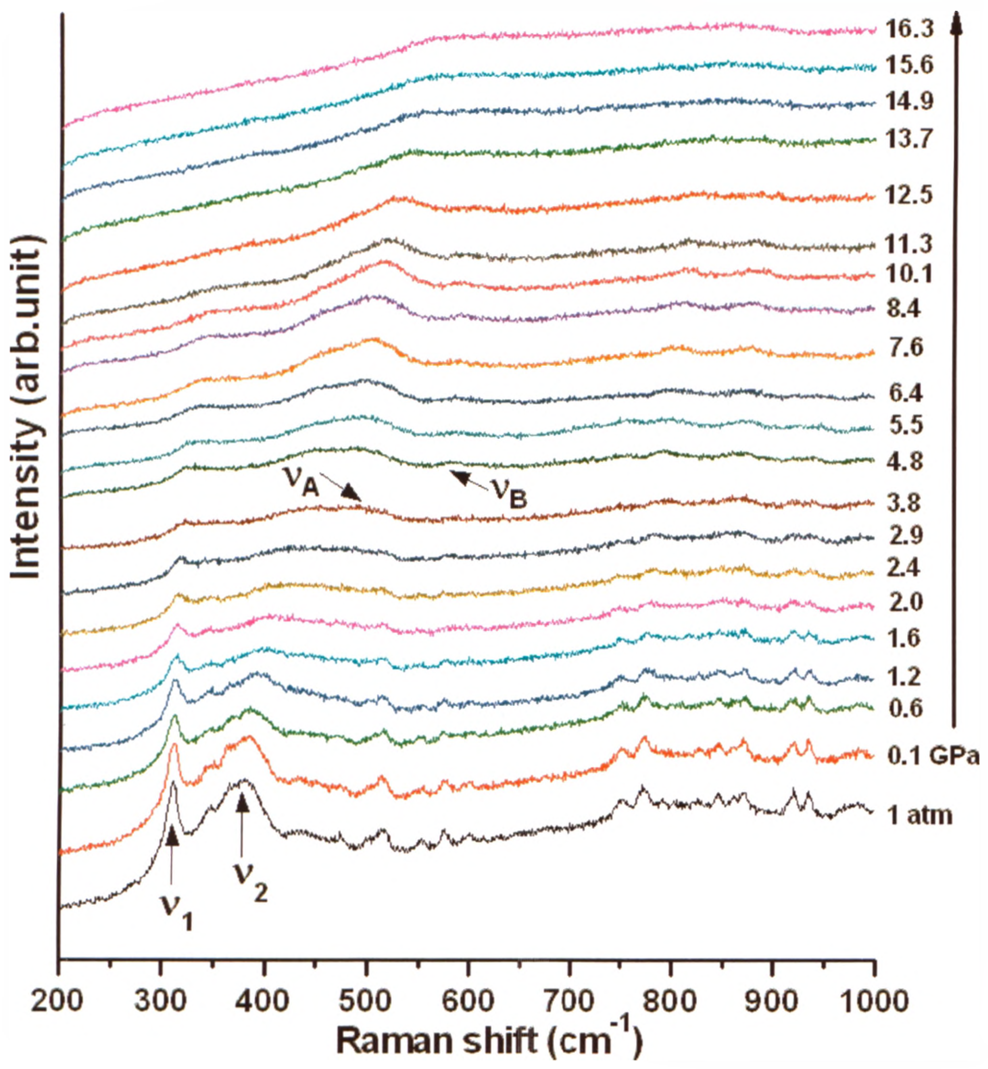

Figure 3.3 Selected Raman spectra of the as-made siliceous ZSM-5 on compression with the 488 nm excitation line in the pressure region 0 – 16.3 GPa in the spectral region of 200 – 1000 cm^{-1}. The vertical arrow indicates the experimental sequence.

The pressure dependence of characteristic Raman modes for the as-made ZSM-5 in the region of 200 – 1000 cm^{-1} during compression is shown in Figure 3.4. All the bands exhibit a pressure-induced linear blue shift. In general, the major changes in the spectra such as the sudden change in the slope of pressure-dependence, disappearance of the initial peaks and appearance of new peaks provide evidence for the start and finish of the pressure-induced phase transitions including amorphization.

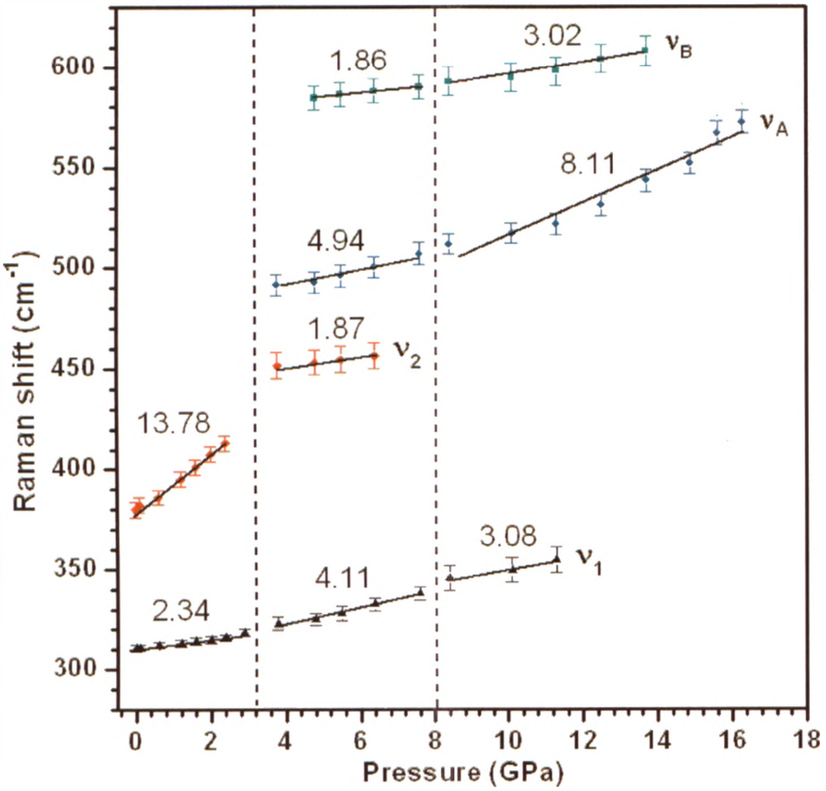

Figure 3.4 Pressure dependence of the Raman shift of the as-made siliceous ZSM-5 in the spectral region of 200 – 1000 cm^{-1}. The vertical dashed lines denote the proposed phase boundaries. The *dv/dP* values (cm^{-1}/GPa) are indicated.

The proposed phase boundaries for as-made ZSM-5 are denoted as dash lines in the Figure 3.4. The first distinct region is between 0 – 2.9 GPa where the Raman modes ν_1 and ν_2 show linear and positive pressure dependences with *dv/dP* values of 2.34 and 13.78 cm^{-1}/GPa, respectively. The values indicate that the structure of this zeolite is more compressible than that of the template ions. Overall, this region almost contains the initial as-made ZSM-5 whose structure gradually deforms under pressure.

In the second pressure region (3.8 – 7.6 GPa), the ν_2 mode shows a much smaller *dv/dP* value of 1.87 cm^{-1}/GPa than that in the first region, and two new modes ν_A and ν_B can be seen, which clearly means an amorphous material forms in the sample. All the phenomena indicate that the crystalline zeolite gradually transforms to an amorphous phase under high pressure and the system is a mixture in this pressure region.

In the highest pressure region (above 7.6 GPa), the v_2 mode disappears and the bands assigned to the amorphous material both show bigger *dv/dP* values than those in the second pressure region, which indicates a different amorphous phase may form. Finally, only amorphous materials exist in this region without any zeolite left. Overall, the two phase boundaries indicate the crystalline to amorphous and the amorphous to amorphous phase transitions, respectively.

The selected Raman spectra of the same sample in the spectral region of 1000 – 1600 cm^{-1} are shown in Figure 3.5. All the strong bands (v_3, v_4, v_5) are due to the template. In the pressure range of 0 – 2.9 GPa, the intensities of these bands gradually decrease with increasing pressure and the bands also experience slight line-broadening. These phenomena may indicate that the pressure starts to change the template's environment which is the surrounding zeolite framework. Thus, the initial ordered arrangement of the trapped TPA^+ cations is also affected by high pressure. In the pressure range of 3.8 – 7.6 GPa, the intensities of these bands gradually drop, which implies that pressure causes a drastic change in the local structure around the template and makes the arrangement of the trapped TPA^+ cations more disordered. The v_3 and v_4 modes are almost invisible when pressure is above 7.6 GPa. The v_5 mode turns into a broad hump and eventually disappears above 13.7 GPa, suggesting highly disordered orientations of the template cations at high pressures.

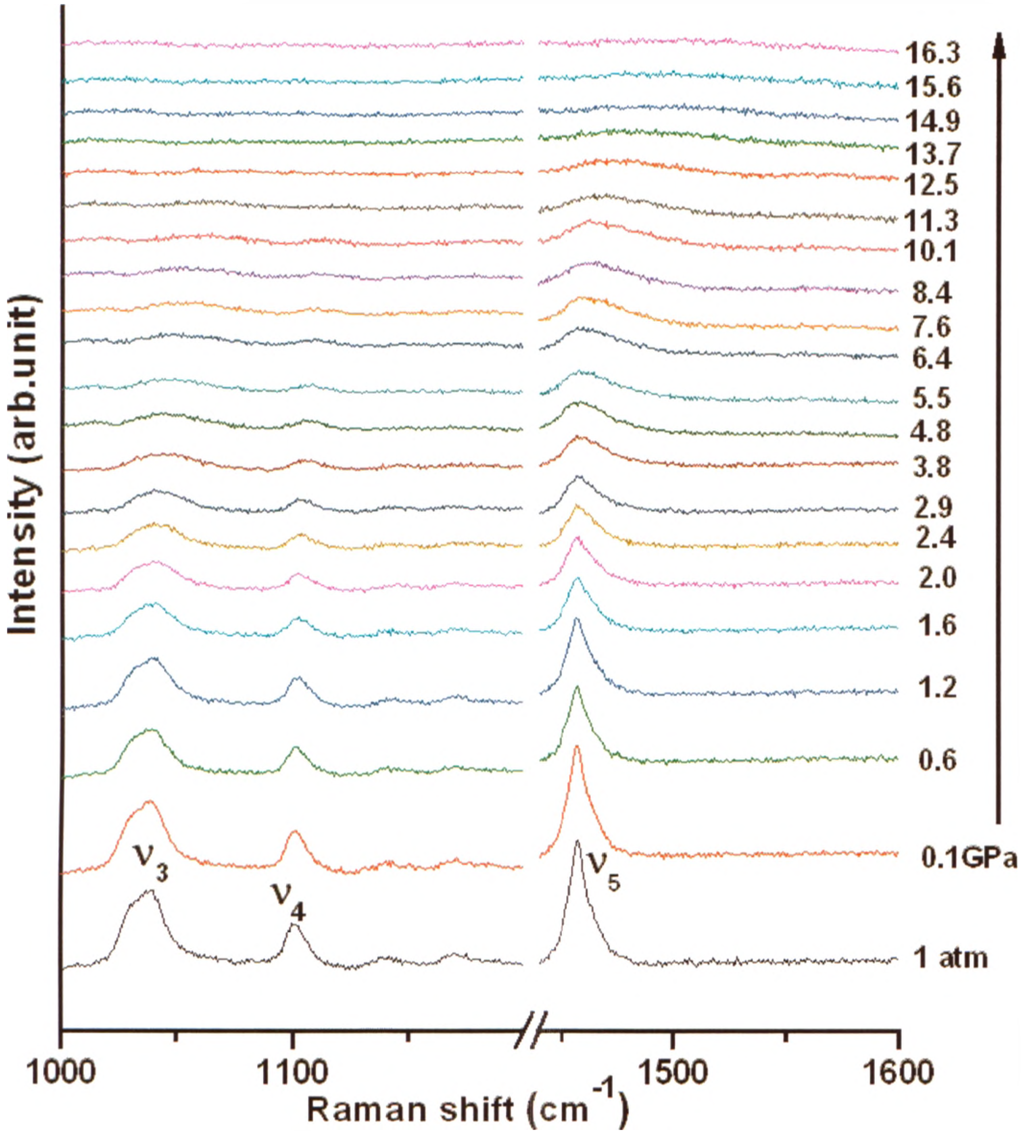

Figure 3.5 Selected Raman spectra of the as-made siliceous ZSM-5 on compression in the spectral region of 1000 – 1600 cm^{-1}.

The pressure dependence of characteristic Raman modes for the as-made ZSM-5 in the region of 1000 – 1600 cm^{-1} during compression is shown in Figure 3.6. All the modes also exhibit a pressure-induced linear blue shift. Figure 3.6 shows a slight change in the slopes (*dv/dP*) of the pressure dependence of these modes at around 3 GPa, indicating the onset of the amorphization. In the pressure region above 8 GPa, v_3 and v_4 modes vanish, and the dv/dP value of v_5 increases to 2.79 from 0.50 cm^{-1}/GPa, which may mean another step of amorphization. Above 14 GPa, no modes can be followed, suggesting the finish of PIA. These three pressure regions are consistent with those in the previous spectral region.

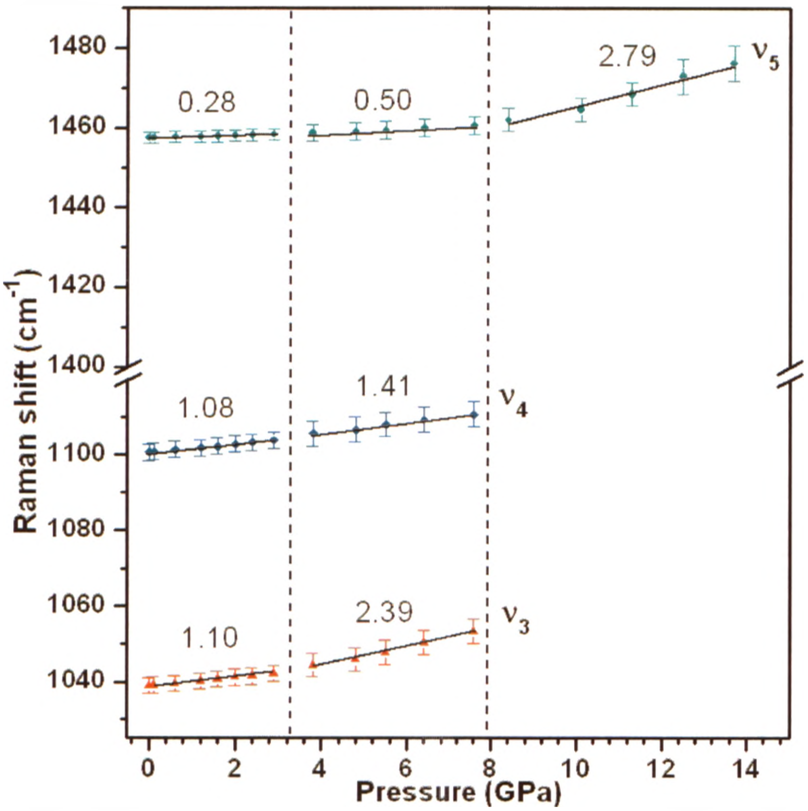

Figure 3.6 Pressure dependence of the Raman shift of the as-made siliceous ZSM-5 in the spectral region of 1000 – 1600 cm^{-1}.

We also conducted the *in situ* Raman experiment for the pure crystalline TPAB solids to further illustrate the behaviour of the template molecules under high pressure, which may help us to understand the role of the occluded template in the ZSM-5 framework in phase transition. The spectra of TPAB in the region of 1000 – 1600 cm^{-1} are shown in Figure 3.7 and were acquired as a function of pressure up to 16.1 GPa at room temperature. Compared to the spectral profile of the occluded TPA$^+$ cations which exhibits a series of broad overlapping bands at ambient pressure, the spectral profile of the crystalline TPAB at the same conditions is somewhat different, since it exhibits a series of sharp and well defined peaks with slightly shifted frequencies. The difference is due to the fact that the TPA$^+$ cations in ZSM-5 are localised at the channel junctions with each of the associated propyl chains being running down one of the intersecting channels. Thus, no interaction between the adjacent TPA$^+$ cations is expected, only the individual propyl chains which are loosely constrained by the channel framework can exhibit a certain degree of conformational disorder.[50]

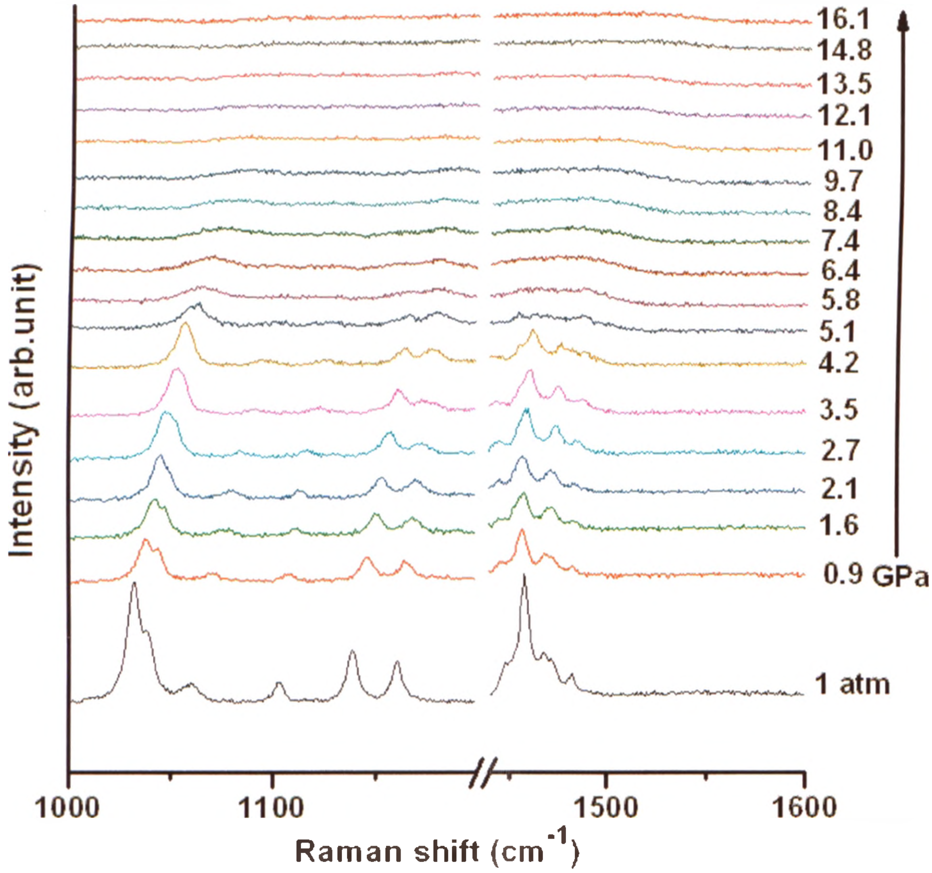

Figure 3.7 Selected Raman spectra of the crystalline TPAB on compression in the pressure region 0 – 16.1 GPa in the spectral region of 1000 – 1600 cm^{-1}.

Compression of crystalline TPAB results in some visible changes in the Raman spectra. In the pressure range of 0 – 4.2 GPa, all the bands in Figure 3.7 gradually shift to higher frequencies with slight line-broadening, suggesting the TPA$^+$ cations start conformational disorder. At 5.1 GPa, the intensities of all the bands decrease dramatically, which probably implies the start of PIA. The broad band also implies that the TPA$^+$ cations experience both conformational and positional disordering. From 5.8 to 11.0 GPa, all the low intensity broad bands gradually turn into broad humps and eventually disappear. No difference among the spectra can be detected above 11.0 GPa, which suggests that the PIA has finished. The solid is completely disordered with each cation having its own local environment and the TPA$^+$ cations adopting all the possible orientations. Overall, the evolution of the crystalline TPAB is quite similar to that of the occluded TPA$^+$ cations in ZSM-5 under high pressure in this spectral region.

The selected Raman spectra of the as-made siliceous ZSM-5 in the spectral region of 2700 – 3200 cm^{-1} are shown in Figure 3.8. All the strong bands (ν_6, ν_7, ν_8) are assigned to the template's C-H stretching vibrations. In the pressure range of 0 – 2.9 GPa, the intensities of these bands gradually decrease upon compression and the bands also undergo slight line-broadening. These observations again indicate that the pressure starts to change the zeolite framework which is the template's environment, therefore, the trapped TPA$^+$ cations are also affected by high pressure. In the pressure range of 3.8 – 7.6 GPa, the ν_7 and ν_8 modes gradually merge into a single broad band which shifts to higher frequencies and the ν_6 mode gradually disappears, suggesting that pressure causes a dramatic change in the environment of template molecules and makes the arrangement of the trapped TPA$^+$ cations more disordered. The ν_6 modes almost vanishes when pressure is above 7.6 GPa and the broad single band becomes an envelope which further shifts to higher frequencies until the highest pressure applied, indicating completely disordered orientations of the template cations under high pressure.

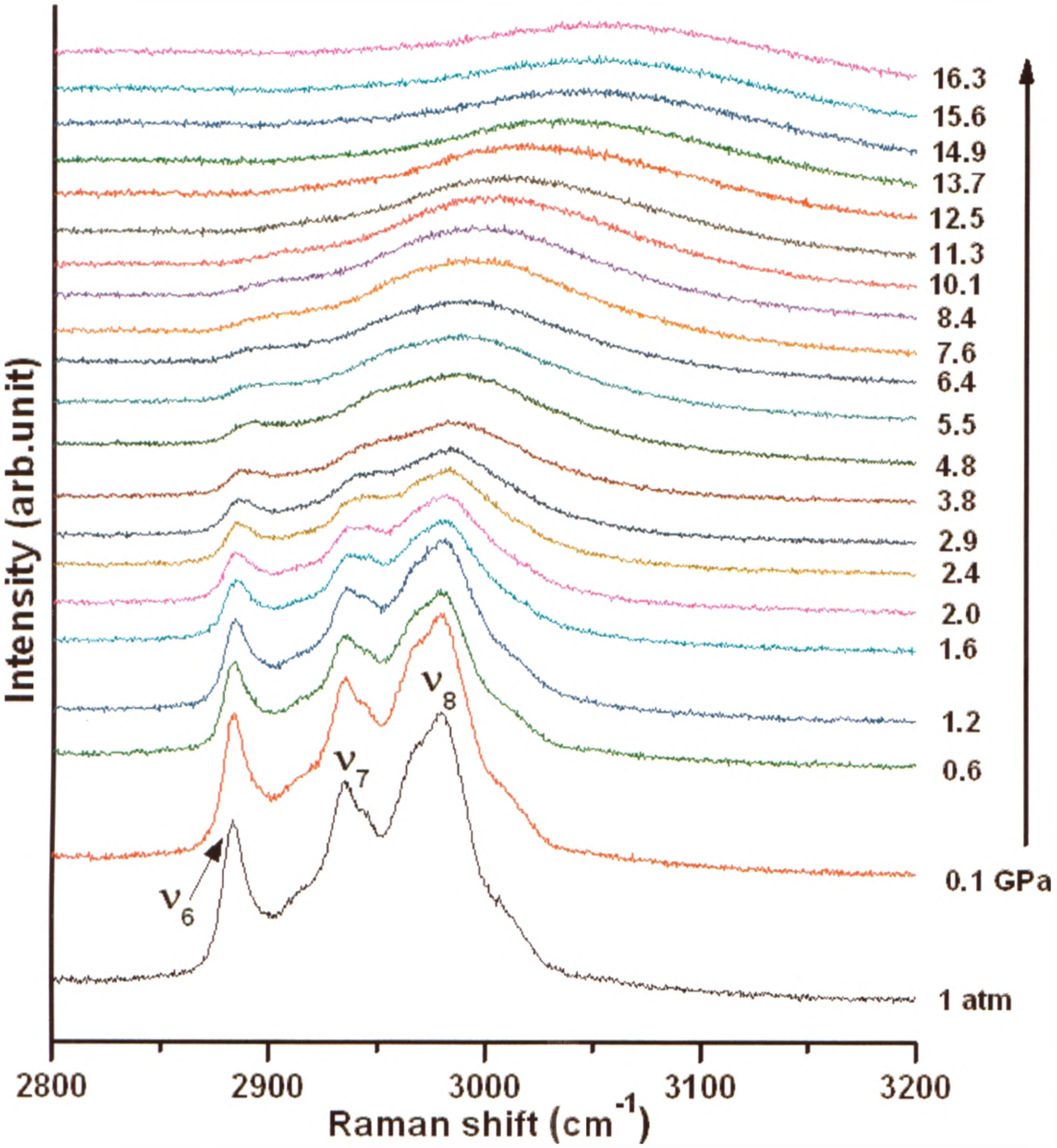

Figure 3.8 Selected Raman spectra of the as-made siliceous ZSM-5 on compression in the spectral region of 2800 – 3200 cm^{-1}.

The pressure dependence of characteristic Raman modes for the as-made ZSM-5 in the region of 2800 – 3200 cm^{-1} during compression is shown in Figure 3.9. Discontinuities in the pressure dependence of these modes can be seen clearly at around 3 GPa, indicating that the amorphization starts. In the pressure region above 8 GPa, ν_6 and ν_7 modes vanish, and the *dν/dP* value of ν_8 increases to 7.82 from 2.21 cm^{-1}/GPa, suggesting the change in the structure of amorphous phase. Above 14 GPa, no noticeable change in the spectra can be detected, suggesting that PIA process is complete. The three pressure regions are consistent with those in the previous spectral regions, indicating that the changes seen in all the spectral windows correspond to the same PIA process of the as-made siliceous ZSM-5.

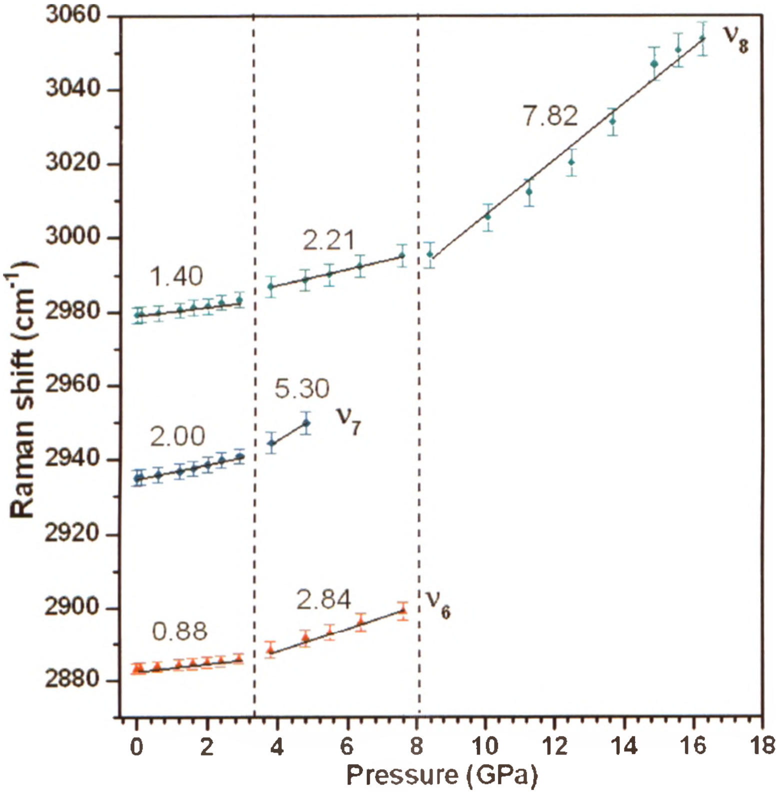

Figure 3.9 Pressure dependence of the Raman shift of the as-made siliceous ZSM-5 in the spectral region of 2800 – 3200 cm^{-1}.

The spectra of crystalline TPAB solids in the spectral region of 2800 – 3200 cm^{-1} are shown in Figure 3.10, and were acquired as a function of pressure up to 16.1 GPa. All the peaks in this region are also due to the C-H stretching vibrations of TPA$^+$ cations. At 0.9 GPa, the strongest peak originating at 2950 cm^{-1} splits into two overlapping peaks at about 2952 and 2957 cm^{-1}, and another sharp peak at 2975 cm^{-1} also splits into two peaks at about 2973 and 2985 cm^{-1}. In the pressure region of 0.9 – 4.2 GPa, the separations of the split peaks gradually increase, and the peaks quickly shift to higher frequencies. Compared to the bands at lower frequencies which have almost no obvious change, these two peaks at 2950 and 2975 cm^{-1} of the initial sample are attributed to the C-H stretching of the methylene groups in the TPA^{+} cations.[52] Since the original chemical environments of two methylene groups of the propyl chains are averaged due to the relatively large degree of mobility, only one peak can be detected in the spectrum at ambient pressure. However, the chemical environments of the two methylene groups become more and more different due to the enhanced restriction on their motions with increasing pressure.

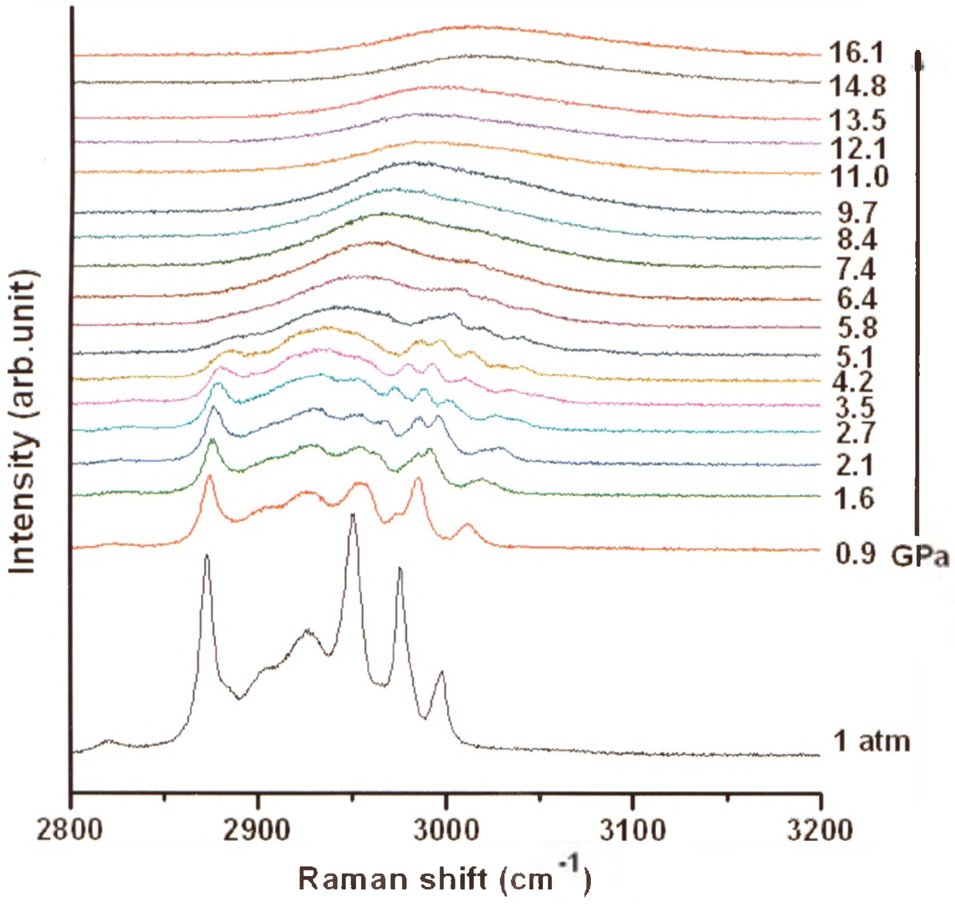

Figure 3.10 Selected Raman spectra of the crystalline TPAB on compression in the spectral region of 2800 – 3200 cm^{-1}

At 5.1 GPa, all the initial sharp and well defined peaks turn into broad bands and overlap to some degree, which implies the occurrence of PIA and the average of all the possible environments of the methyl and methylene groups of TPA^+ cations. Above 5.8 GPa, all the weak broad bands gradually transform to broad humps, and only a very broad envelope can be followed at 7.4 GPa. No significant difference among the spectra can be detected above 11.0 GPa, indicating the finish of PIA and totally disordered orientations of the TPA^+ cations. The results imply that the evolution of the crystalline TPAB is similar to that of the occluded TPAB in ZSM-5 in this spectral region under high pressure.

3.3.1.1.3 Raman Spectra of As-made Siliceous ZSM-5 on Decompression

The reversibility of the pressure effect on zeolite structure provides information on transformation mechanisms. We measured Raman spectra upon successive decompression of the sample to ambient pressure. Figure 3.11 shows that the profiles of the new Raman bands due to an amorphous material formed at high pressure gradually change with decreasing pressure.

In the decompression spectra we observed a new weak band (ν_C) which is also attributed to amorphous materials, but this band is hardly detected in the compression spectra. These bands all move back to lower frequencies until ambient pressure is reached. The intensities of the bands increase during decompression. No other band appears until the pressure is decreased to 2.4 GPa at which a weak broad hump is noticed in the region of 330 – 400 cm^{-1}. This band becomes more distinct with decompression, and it actually contains several overlapping bands which probably correspond to the initial Raman modes of ν_1 and ν_2.

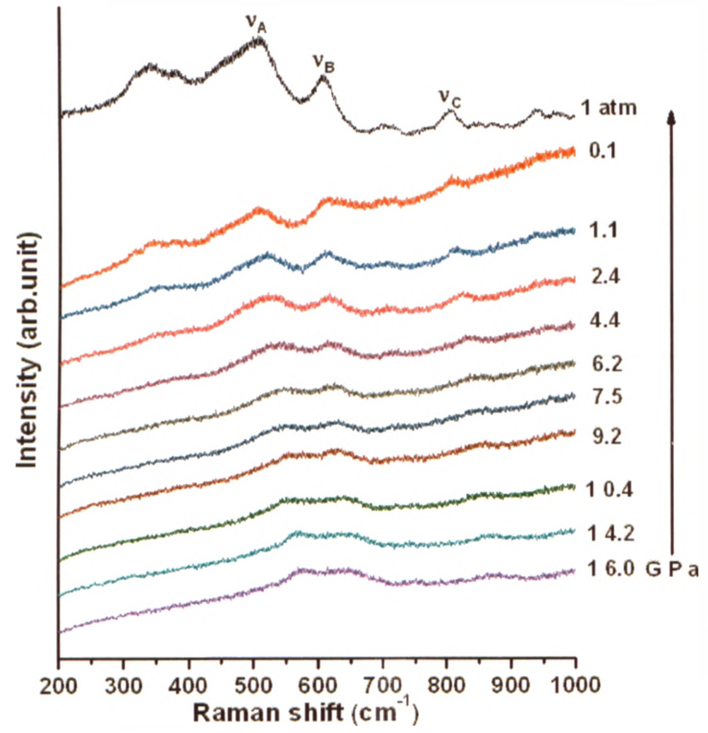

Figure 3.11 Selected Raman spectra of the as-made siliceous ZSM-5 during decompression from 16.0 GPa to ambient pressure in the spectral region of 200 – 1000 cm^{-1}. The vertical arrow indicates the experimental sequence.

In Figure 3.12 (a), we can easily see that the spectra taken at ambient conditions before compression and after decompression look very different in the region above 400 cm^{-1}, which means that the pressure-induced amorphous phase is mostly retained after releasing pressure. However, in the decompression spectrum, the three overlapping peaks below 400 cm^{-1} exhibit some similarities to those in the spectrum of the sample before compression. The band at 380 cm^{-1} of the recovered sample is associated with the ZSM-5 framework, which probably indicates that the framework of as-made ZSM-5 is partially recovered.

The spectrum of the retrieved sample looks almost the same as that of an amorphous SiO_2 (a tetrahedral oxide glass) obtained by high-pressure treatment in previous studies.[35, 53, 54] In those studies, the bands of the decompressed silica sample close to 500 and 610 cm^{-1} (Figure 3.12 (b)) are the D_1 and D_2 lines which shifted from 486 and 601 cm^{-1} (Figure 3.12 (c)) of the silica before compression, and these bands are attributed to symmetric stretching modes of vibrationally isolated 4-membered rings (4MR) and 3-membered rings (3MR) of SiO_2, respectively.[55] The main band (at 450 cm^{-1}) which is close to the D_1 line of the silica before compression in Figure 3.12 (c) is mainly associated with Si-O-Si symmetric stretching modes of 5MR and 6MR [56]; it shifts to higher frequency and merges with the D_1 line on compression (Figure 3.12 (b)), which indicates a conversion of the larger rings to smaller ones.[54]

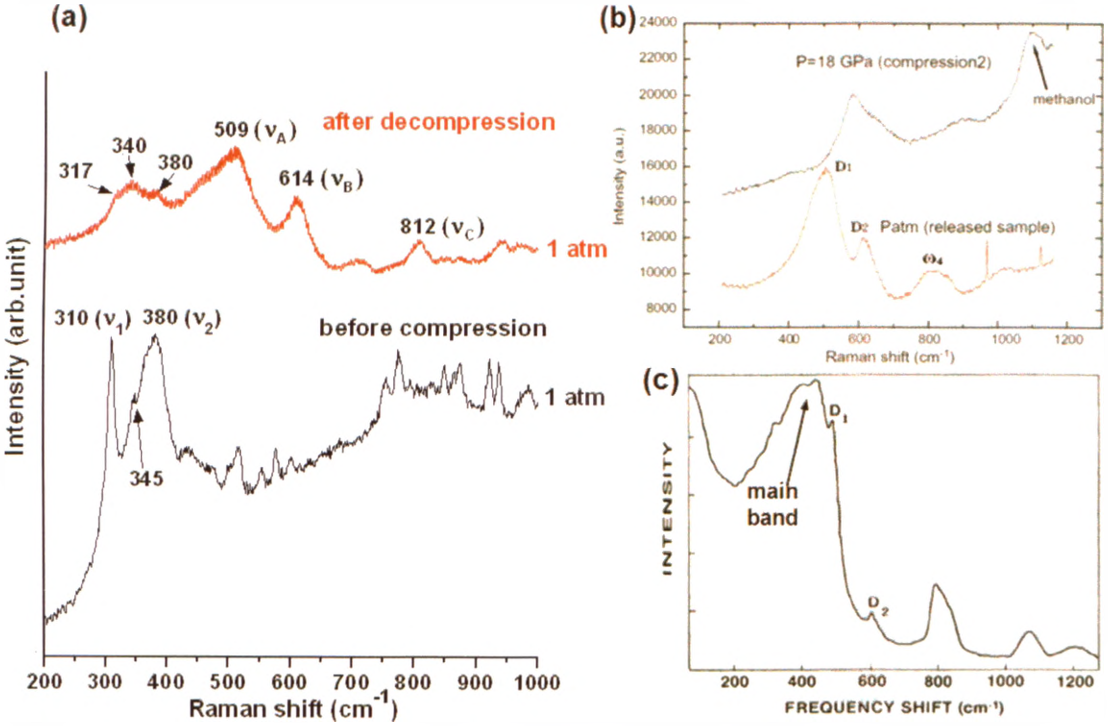

Figure 3.12 (a) Raman spectra of the as-made siliceous ZSM-5 before compression and after decompression in the spectral region of 200 – 1000 cm^{-1}; (b) Raman spectra of the silica glass at pressure 18 GPa and after pressure treatment (red) (Adapted from Ref. 35); (c) Raman spectrum of silica sample before compression (Adapted from Ref. 54)

In above-mentioned studies, the amorphous phase of SiO_2 before compression referred to as low density amorphous (LDA) silica which largely contains 5MR and 6MR (Figure 3.12 (c)) is converted to another amorphous phase of SiO_2 referred to as high density amorphous (HDA) silica which mainly has 3MR and 4MR (Figure 3.12 (b)) by high pressures (polyamorphic transition).[35]

In previous studies of zeolites,[27, 57, 58] the appearance of LDA and HDA phases has been detected by *in situ* Raman and XRD with synchrotron radiation and other techniques under high pressures. Moreover, computer simulations have been used to reveal the mechanisms of PIA and of the occurrence of polyamorphism.[11, 39] Since the zeolite studied in the present work merely consists of silicon and oxygen atoms, it is reasonable to conjecture that the as-made siliceous ZSM-5 also experiences two amorphous phases in the PIA process. Firstly, the zeolite starts to transform to the LDA silica at around 3 GPa, and then the degree of the conversion of ZSM-5 to the LDA silica increases with increasing pressure. Secondly, the LDA silica starts to evolve into HDA silica at around 7 GPa, and the amount of the HDA silica gradually increases upon compression. Finally, only the HDA silica exists in the system at around 14 GPa and the PIA is complete.

The spectra in Figures 3.13 and 3.14 show the evolution of the Raman modes of the TPA^+ cations occluded in the as-made ZSM-5 in other regions upon decompression. In Figure 3.13 (a), the v_3 and v_4 bands are not observable until 2.4 GPa and shift to lower frequencies with decreasing pressure. The v_5 mode, which is an extremely broad band at high pressure, gradually becomes narrower and also moves to lower frequency upon decompression. From Figure 3.13 (b), we can clearly see that all the bands are much wider than those in the spectrum before compression.

In Figure 3.14 (a), upon decompression, the broad hump of C-H stretching is slowly changing back towards its profile before compression. The v_6 mode cannot be seen until 2.4 GPa and the v_7 and v_8 modes always overlap. Although the bands almost shift back to their initial positions, they still remain very broad and overlapping after decompression (Figure

3.14 (b)).

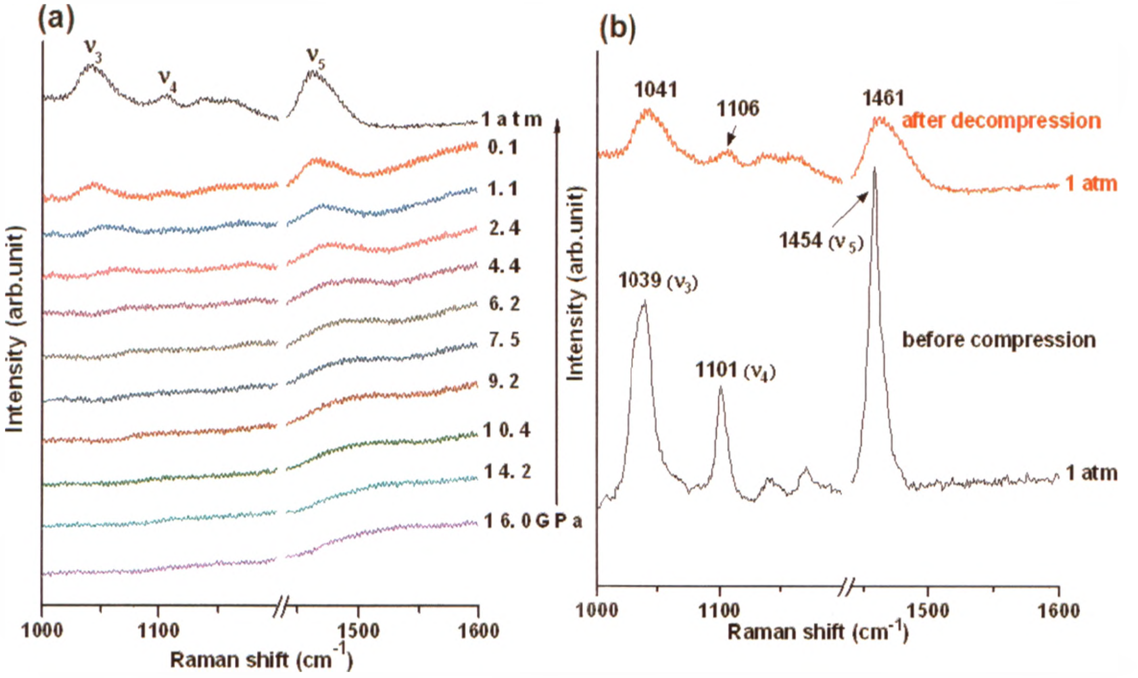

Figure 3.13 (a) Selected Raman spectra of the as-made siliceous ZSM-5 during decompression from 16.0 GPa to ambient pressure and (b) Raman spectra of the same sample before compression and after decompression in the spectral region of 1000 – 1600 cm^{-1}

In all three spectral regions, the evolution of the template vibrations shows that the changes induced by pressure are almost reversible in the spectra upon decompression. However, the spectra taken at ambient conditions after decompression show that the template peaks are broader compared to those before compression, and the peak positions are not exactly identical. These results imply that the environments of the trapped template cations are still disordered upon decompression. This indicates that the sample still contains a large quantity of amorphous material after decompression, which is consistent with the results mentioned earlier.

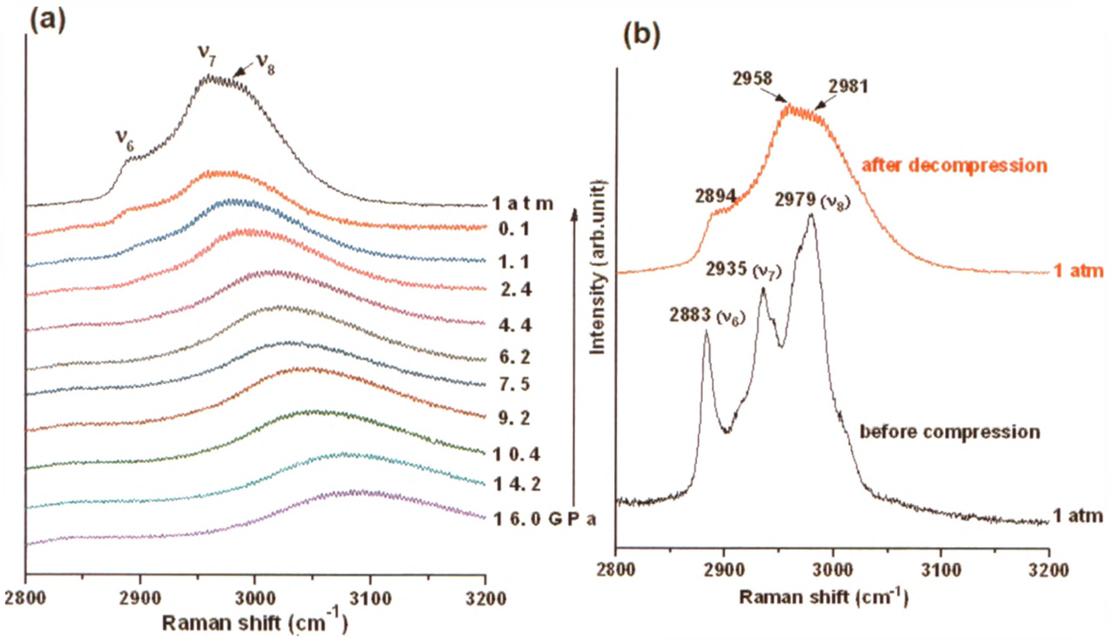

Figure 3.14 (a) Selected Raman spectra of the as-made siliceous ZSM-5 during decompression from 16.0 GPa to ambient pressure and (b) Raman spectra of the same sample before compression and after decompression in the spectral region of 2800 – 3200 cm^{-1}

We also investigated the behaviour of the crystalline TPAB upon decompression after it become amorphous at 16.1 GPa. The spectra in Figures 3.15 and 3.16 show the evolution of the Raman modes of the crystalline TPAB in the two spectral regions upon decompression. In Figures 3.15 (a) and 3.16 (a), no drastic change of the spectra can be detected until 2.2 GPa except that the broad humps gradually shift to lower frequencies with increasing intensities, and this process is quite similar to that of the occluded TPA$^+$ cations upon decompression. At 0.4 GPa, the broad peaks become very sharp and well defined, and they now very similar to the initial peaks. In Figures 3.15 (b) and 3.16 (b), the spectra of the sample after decompression are consistent with those of the initial TPAB with the identical peak positions and without significant line-broadening. Only the intensities of the bands of the recovered sample are less than those of the initial sample, which probably due to the fact that the residual sample in DAC after being compressed is much less than the amount of sample in the DAC before compression.

In both spectral regions, the evolution of the crystalline TPAB vibrations shows that the changes in the spectra are reversible upon decompression, which implies that the TPA^+ cations almost return to their initial crystalline state after decompression to ambient pressure, and the PIA is totally reversible. This is due to the fact that the template molecules are covalently bonded entities which are little affected by the pressures applied.[6] The evolution of the crystalline TPAB is quite different from that of trapped TPA^+ cations in as-made siliceous ZSM-5. The situation for the as-made ZSM-5 indicates that the disordered state of the occluded template cations after decompression is due to the highly distorted HDA silica network surrounding the template molecules and this further demonstrates that the majority of the zeolite framework has already collapsed under high-pressure treatment and cannot be recovered after decompression.

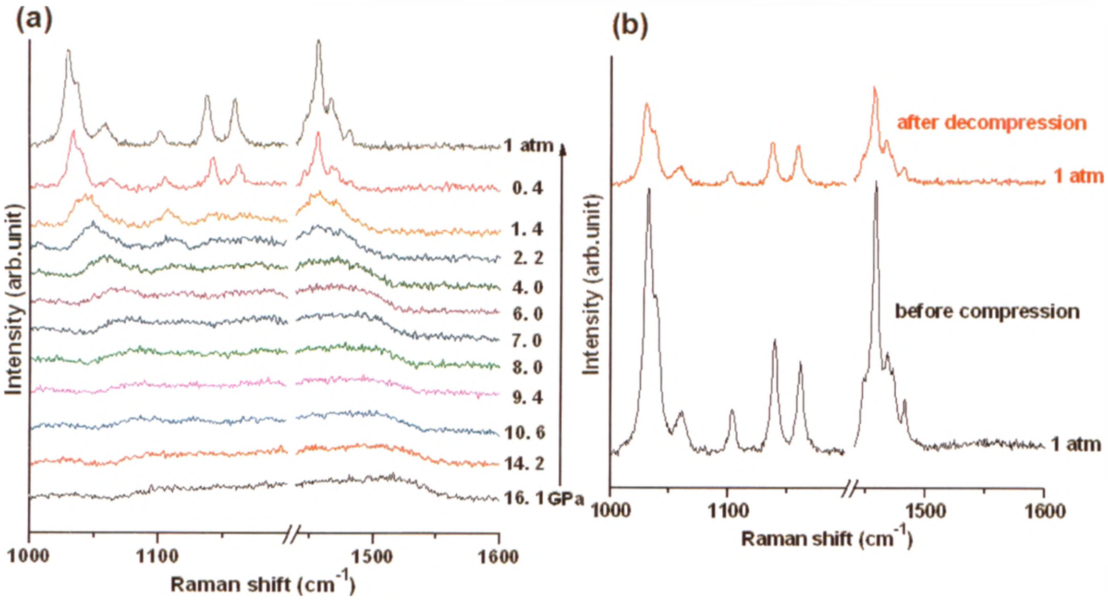

Figure 3.15 (a) Selected Raman spectra of the crystalline TPAB during decompression from 16.1 GPa to ambient pressure and (b) Raman spectra of the same sample before compression and after decompression in the spectral region of 1000 – 1600 cm^{-1}

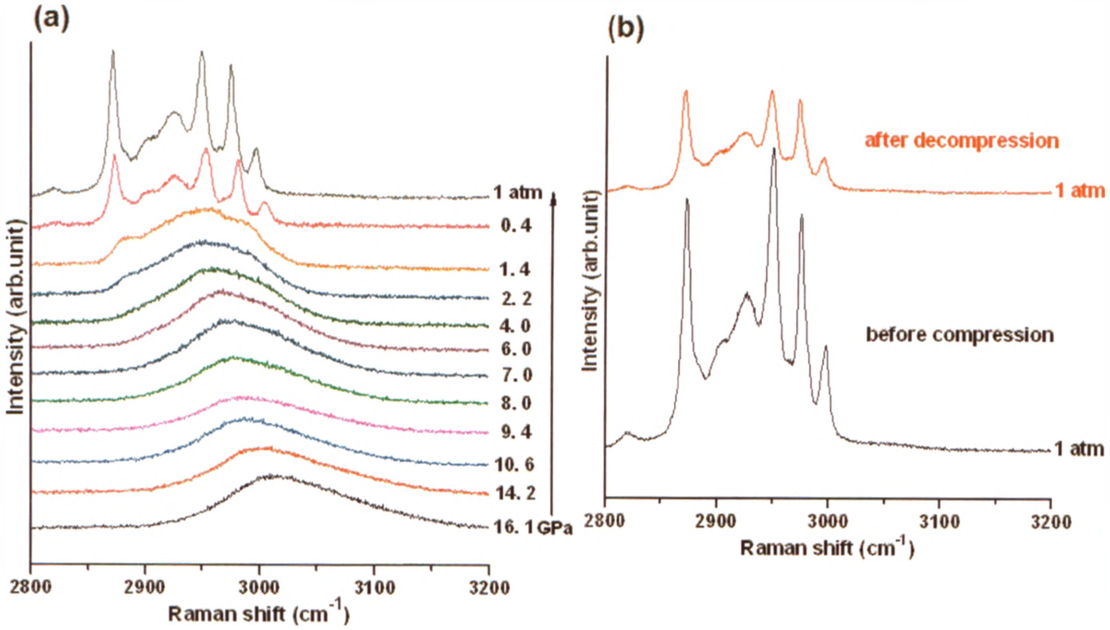

Figure 3.16 (a) Selected Raman spectra of the crystalline TPAB during decompression from 16.1 GPa to ambient pressure and (b) Raman spectra of the same sample before compression and after decompression in the spectral region of 2800 – 3200 cm^{-1}

3.3.1.2 IR Spectra of As-made Siliceous ZSM-5

IR spectroscopy was also used in the present study as a complementary technique to Raman spectroscopy since IR is a sensitive tool for monitoring the changes in the zeolite frameworks via the zeolite vibrations in the region of 200 to 1300 cm^{-1} while the vibrations are weak in the corresponding Raman spectra.[59, 60] The IR spectrum of this material at ambient conditions is shown in Figure 3.17, which is comparable to the spectra reported in the previous studies.[61-65] All the peaks labeled in Figure 3.17 can be observed under high pressure and are assigned in Table 3.2 based on the reference.[65]

Based on the IR investigations of zeolites by Flanigen *et al.*,[60] there are two classes of vibrations: (1) the internal vibrations which are due to TO_4 (T = Si or Al) units existing in all zeolites and also in silica or quartz. These vibrations are neither sensitive to the zeolite topology nor to the second building units (SBUs) in the framework; (2) the external vibrations involving the linkages of different tetrahedra. Therefore, these vibrations are sensitive to the framework structure of certain zeolites and to the presence of some SBUs such as double rings and other unique T-O-T linkages. The four bands of ZSM-5 labeled on Figure 3.17 also belong to these two categories: the broad band at 1083 cm^{-1} has been assigned to the internal SiO_4 vibration and the other bands have been assigned to the external linkages of tetrahedra previously.[61-64]

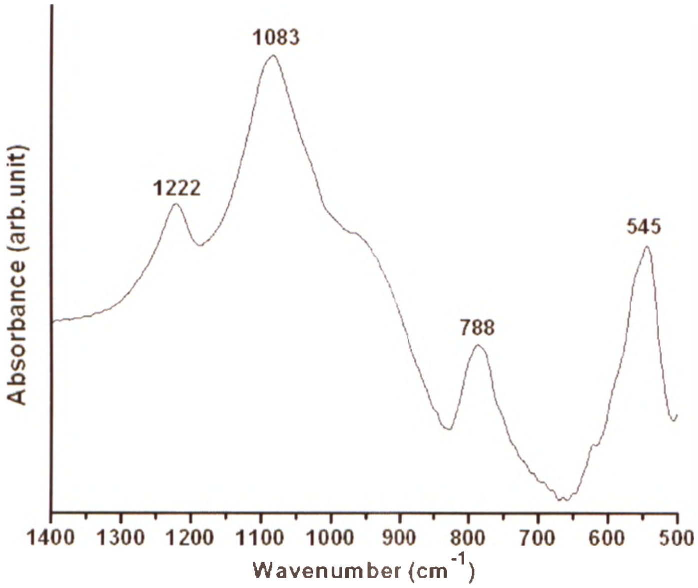

Figure 3.17 IR spectrum of as-made siliceous ZSM-5 at ambient conditions

Table 3.2 IR framework vibrations (cm^{-1}) of as-made siliceous ZSM-5

ZSM-5[a]	ZSM-5[b]	Assignments
545	550	external ν_s (Si-O) stretching of 5MR
788	790	external ν_s (Si-O-Si) stretching
1083	1093	internal ν_{as} (Si-O-Si) stretching
1222	1225	external ν_{as} (Si-O) stretching of 5MR

[a] this work; [b] Ref. 65

The *in situ* IR spectra of as-made siliceous ZSM-5 were acquired as a function of pressure up to 14.1 GPa at room temperature. The selected spectra in the region of 500 – 1400 cm^{-1} are shown in Figure 3.18. The usually strong IR band near 450 cm^{-1} is not detectable under high pressure due to the limitations of the instrument used in the present study. In the spectrum of 0.4 GPa, the band originating at 545 cm^{-1} at ambient pressure shifts to 577 cm^{-1}, which indicates the external linkage of 5MR is subject to high pressure and the framework of the zeolite starts deforming. However, no obvious change can be detected for the other bands in this spectrum except a slightly line-broadening. From 0.4 to 2.2 GPa, no significant change can be observed, except a further increase in the line width.

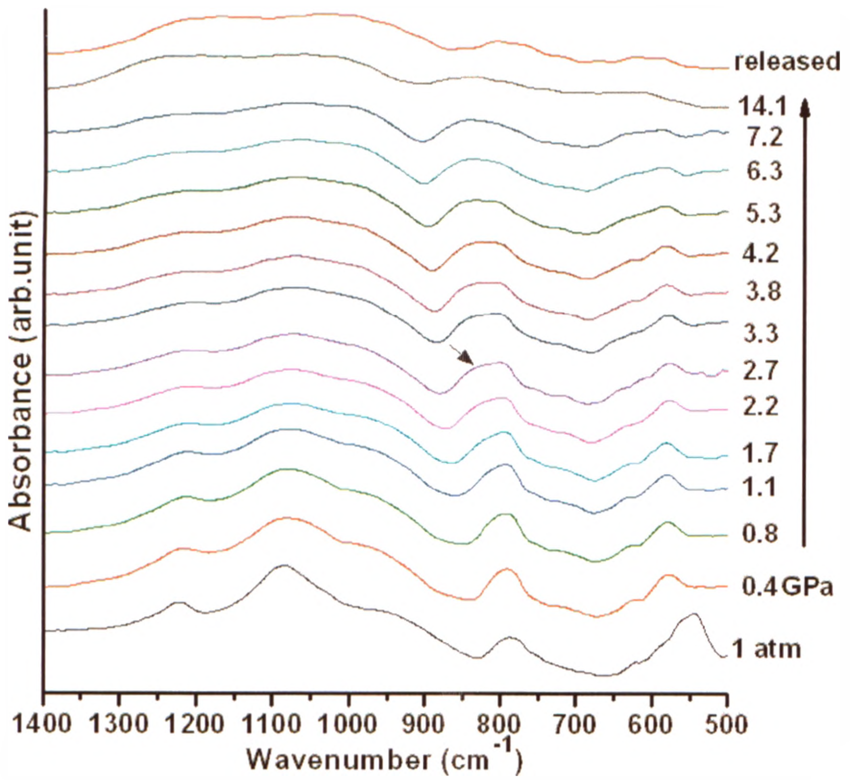

Figure 3.18 Selected IR spectra of the as-made siliceous ZSM-5 on compression in the spectral region of 500 – 1400 cm^{-1}. The vertical arrow indicates the experimental sequence. The small arrow indicates the new band. The released spectrum is the spectrum of the sample recovered from 14.1 GPa.

The band initially at 788 cm^{-1} splits into two overlapping bands and the new shoulder at about 835 cm^{-1} can be seen clearly in the spectrum of 2.7 GPa, which gradually grows up upon compression. This new band is at a position similar to that of the symmetric stretching band of silica which shifts from 805 cm^{-1} at ambient pressure[66] to higher frequencies under high pressures.[67] Thus, the appearance of this new band indicates the formation of an amorphous phase, presumably the LDA silica. This result is consistent with that from the Raman study of this zeolite.

In the spectrum at 4.2 GPa, the overlapping bands merge into one broad band centered at 822 cm^{-1} and continuously shift to higher frequency while other bands just experience slight line-broadening. In the spectra from 4.2 to 7.2 GPa, the band at 822 cm^{-1} further slightly moves to higher frequencies and its width increases with pressure as well. There is no significant change of the spectra between 7.2 GPa and 14.1 GPa except that all the bands become extremely broad and weak. At 14.1 GPa, we cannot detect the band originating at 545 cm^{-1} due to the external linkage of the 5MR, suggesting the initial zeolite has become completely amorphous under high pressures.

Upon releasing pressure, the broad bands at about 837 cm^{-1} and 1240 cm^{-1} at 14.1 GPa move back to 793 cm^{-1} and 1220 cm^{-1} at ambient pressure, respectively, but they are still very broad. The intensities of the other bands increase upon decompression, however, these bands remain extremely broad and overlapping, which look quite different from those before compression. These phenomena imply that the framework of as-made ZSM-5 has collapsed under high-pressure treatment and cannot be recovered after decompression.

3.3.1.3 XRD Patterns of As-made Siliceous ZSM-5

XRD was used to complement the vibrational spectroscopy and to provide direct information about pressure-induced structural transformations. The images of all the XRD spectra collected on the MAR165 CCD X-ray detector with synchrotron radiation are characterized by the presence of numerous spots caused by the poor statistics of the diffraction data, resulting from the relatively large size of the crystallites compared to the beam size. Thus, it is impossible to refine the crystal structure of the zeolite and it is hard to extract the unit-cell parameters from the patterns due to the low symmetry of this zeolite which belongs to orthorhombic crystal system with the Pnma space group.

The as-made siliceous ZSM-5 was compressed to maximum pressure of 14.1 GPa at room temperature. The characteristic XRD patterns during compression are shown in Figure 3.19. The pattern of the sample at ambient pressure before compression is consistent with that of zeolite ZSM-5 with TPA ions of the Powder Diffraction File. Miller indices of the relatively strong peaks are also labeled on this pattern, while the other peaks are not well resolved in the high-pressure patterns.

With increasing pressure, sharp peaks that exist in the middle range of the pattern at ambient conditions become drastically weaker and broader above 1.0 GPa, especially the most intense peak at 5.52^{0} due to the 501 reflection which overlaps with the peaks corresponding to the 303 and 313 reflections. The other two strong peaks located at small angles of 1.91^{0} and 2.13^{0} in the pattern of ambient pressure are identified as the 101 and 200 reflections respectively, and these peaks only broaden very slightly at 1.4 GPa.

Further increase in pressure results in progressive peak broadening and intensity reduction. At 3.2 GPa the diffraction peaks merge into a broad band at around 5.77^{0} and the two peaks at small angles also become broad and move to larger angles. In general, peak broadening and a reduction of intensity are indicative of the onset of amorphization.[68] Thus, the observations indicate that an amorphous phase starts forming at 3.2 GPa. It should be noticed that the scale at which amorphization is observed is only for the long-range and amorphous material should be termed X-ray amorphous, referring to the loss of long-range structural ordering within the crystal lattice.[24] On continuous compression to 7.3 GPa, the broad band is still present, however, the position of it shifts to

5.94°, and the two peaks at the small angles become very broad, which probably indicates an increase in the degree of the amorphization. Finally, the sample becomes completely amorphous at 14.1 GPa.

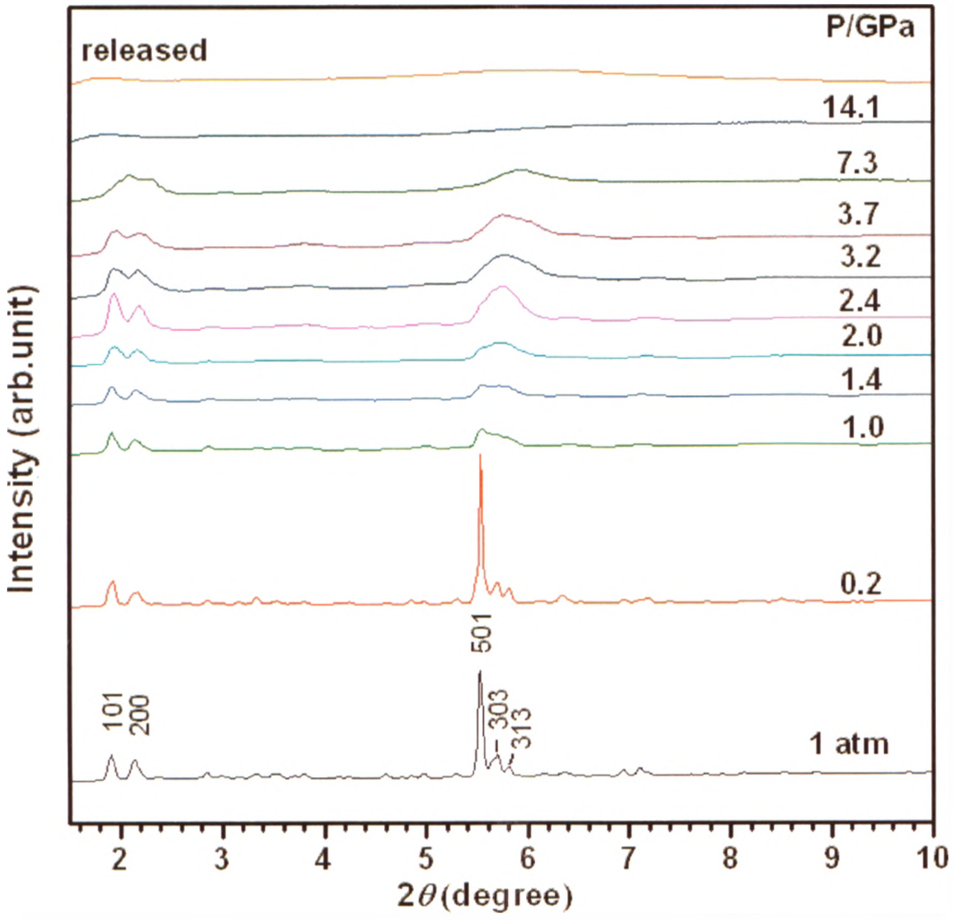

Figure 3.19 XRD patterns of the as-made siliceous ZSM-5 during compression and the released pattern of the sample recovered from 14.1 GPa at room temperature using the wavelength of 0.369126 Å. Miller indices of the relatively strong reflections are labeled on the 1 atm pattern.

After decompression to ambient conditions, the pattern of the released sample is quite comparable to that of the compressed sample at 14.1 GPa, which means the sample cannot recover its crystalline structure and the loss of the long-range ordering in ZSM-5 is irreversible. Since many materials show a large range of pressures in which crystalline and amorphous phases coexist,[69] it is difficult to pinpoint the exact pressure values of the onset and finish of PIA.

3.3.2 High-Pressure Study of Calcined Siliceous Zeolite ZSM-5

3.3.2.1 Raman Spectra of Calcined Siliceous ZSM-5

3.3.2.1.1 Raman Spectrum of Calcined Siliceous ZSM-5 at Ambient Pressure

The spectrum of calcined ZSM-5 (Figure 3.20) is consistent with that reported by Dutta.[52] The most prominent band at 385 cm^{-1} (ν_9) is assigned to the Si-O-Si bending vibration of the 5MR present in this zeolite; this band is the only peak that can be followed at high pressures. The weak bands near 500 cm^{-1} are attributed to the Si-O-Si bending vibrations of the 4MR and 6MR, and the band at around 830 cm^{-1} is assigned to Si-O stretching vibration.[52]

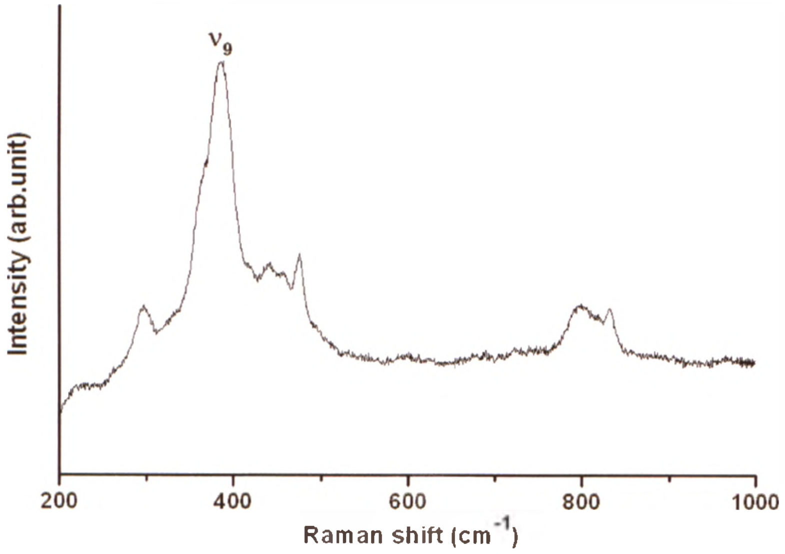

Figure 3.20 Raman spectrum of calcined siliceous ZSM-5 at ambient conditions with the 488 nm excitation line.

3.3.2.1.2 Raman Spectra of Calcined Siliceous ZSM-5 on Compression

The *in situ* Raman spectra of calcined siliceous ZSM-5 were obtained as a function of pressure. The selected spectra in the region of 200 – 1000 cm^{-1}are shown in Figure 3.21. The calcined siliceous ZSM-5 was compressed up to 13.9 GPa at room temperature. The strongest band (ν_9) is gradually suppressed beyond 0.9 GPa, meanwhile, a new weak band (ν_D) appears at 450 cm^{-1} on the high-frequency side of the ν_9 band at 1.5 GPa. The new band is due to the main band of the LDA silica mentioned before.[56, 66] These observations show that the framework of ZSM-5 is quickly distorted under high pressure and an amorphous material appears.

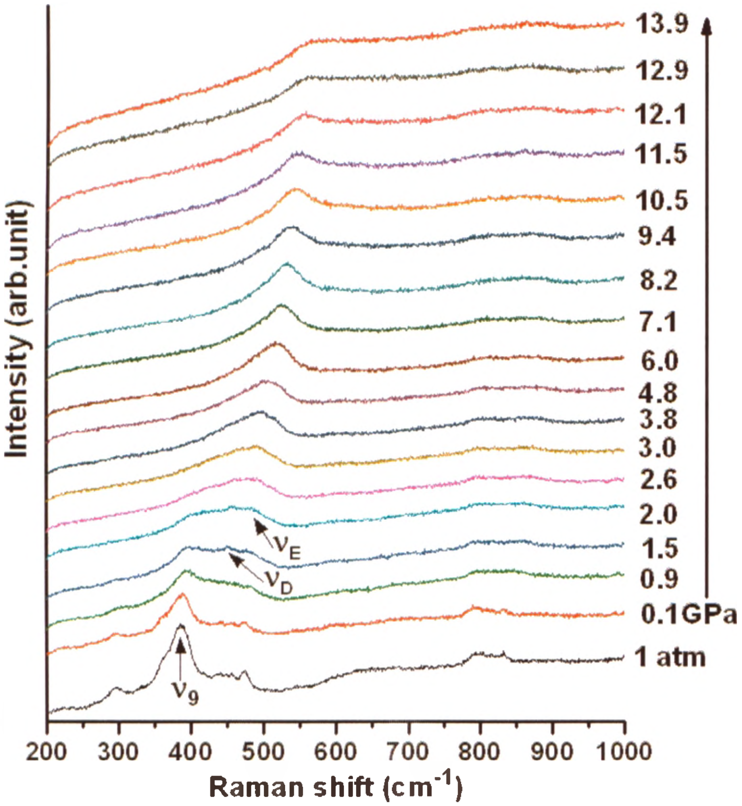

Figure 3.21 Selected Raman spectra of the calcined siliceous ZSM-5 on compression with the 488 nm excitation line in the pressure region 0 – 13.9 GPa in the spectral region of 200 – 1000 cm^{-1}. The vertical arrow indicates the experimental sequence.

At 2.0 GPa, a new broad band (ν_E) is observed clearly at about 481 cm^{-1}, and this new band is apparently due to another amorphous material resulting from amorphization. At 2.6 GPa, the ν_9 mode is hardly visible, the new band ν_E becomes prominent with increasing pressure, and the band ν_D shifts to higher frequency and merges with ν_E. Above 3.0 GPa, the ν_E mode is the only band that can be observed in the spectra, and it gradually shifts to higher frequencies with increasing pressure, suggesting a further amorphization.

Above 11.5 GPa, no significant change can be detected except slight line-broadening and intensity reduction of ν_E band, which implies that this crystalline zeolite totally becomes amorphous and the PIA finishes at around 11 GPa.

The pressure dependence of characteristic Raman modes for the calcined siliceous ZSM-5 during compression is shown in Figure 3.22. All the bands exhibit a pressure-induced linear blue shift. The phase boundaries for this sample are denoted as dash lines in the figure. The first distinct region is between 0 – 1.5 GPa where the modes ν_9 shows linear and positive pressure dependences with a *dv/dP* value of 6.40 cm^{-1}/GPa.

In the second pressure region (1.5 – 3.0 GPa), the mode ν_9 shows a larger *dv/dP* value of 10.20 cm^{-1}/GPa than that in the first region, and two new modes ν_D and ν_E start to show up, which means that the crystalline zeolite gradually becomes amorphous under high pressure and the system is a mixture in this pressure region.

In the highest pressure region (above 3.0 GPa), the ν_9 and ν_D modes disappear whereas the ν_E mode remains, which implies the formation of a different amorphous phase.

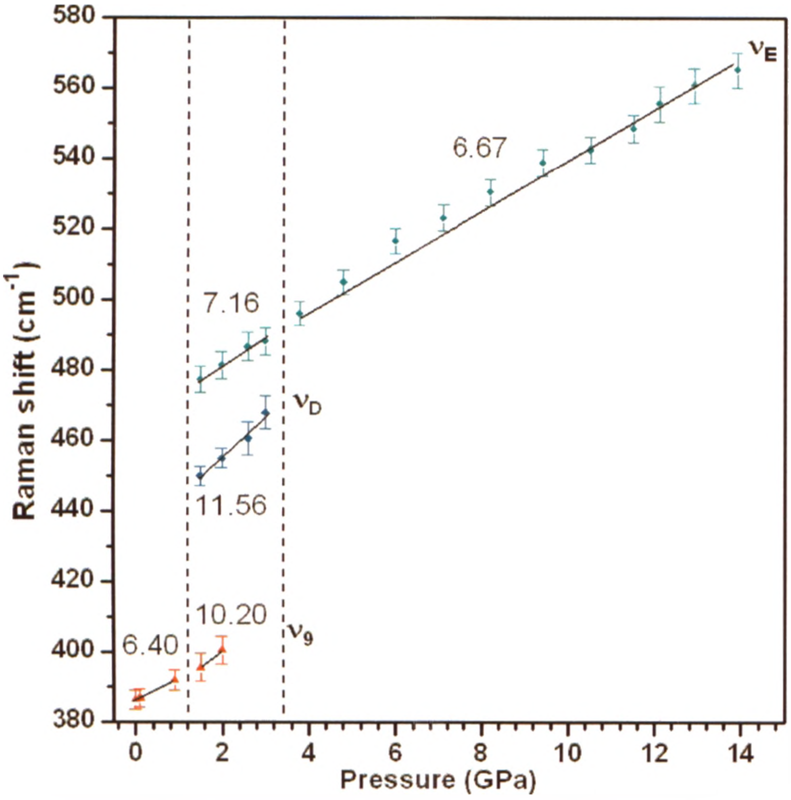

Figure 3.22 Pressure dependence of the Raman shift of calcined siliceous ZSM-5 in the spectral region of 200 – 1000 cm^{-1}. The vertical dashed lines denote the proposed phase boundaries. The *dv/dP* values (cm^{-1}/GPa) are indicated.

3.3.2.1.3 Raman Spectra of Calcined Siliceous ZSM-5 on Decompression

The Raman spectra of the calcined ZSM-5 on decompression are shown in Figure 3.23 from 13.5 GPa to ambient pressure. The new band ν_E gradually shifts to lower frequency and is retained at ambient pressure. A new band (ν_F) can be seen at around 614 cm^{-1}, which gradually emerges during decompression. Another new weak band (ν_G) can only be detected at around 812 cm^{-1} in the spectrum of ambient pressure. These two new bands which were not observable during compression and the band ν_E are assigned to the amorphous material formed at high pressure.

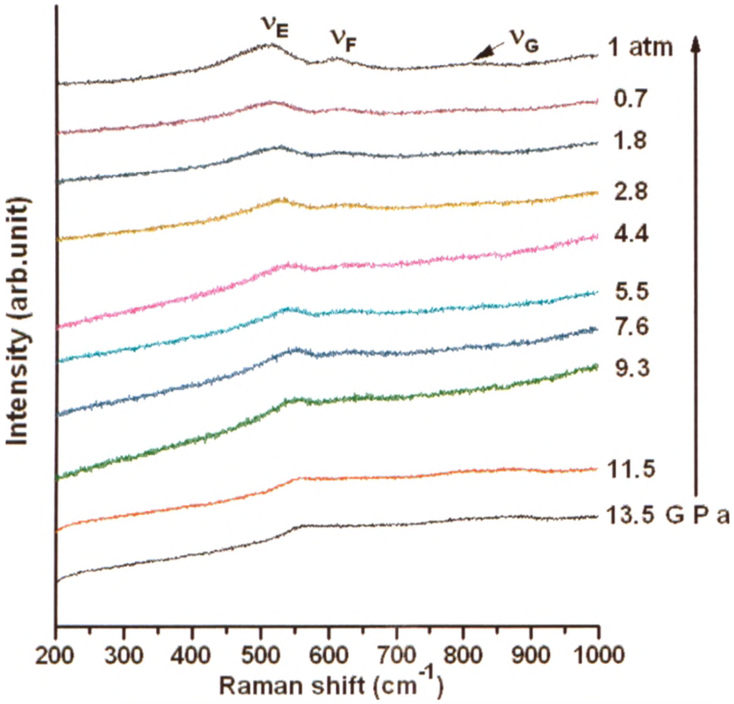

Figure 3.23 Selected Raman spectra of the calcined siliceous ZSM-5 during decompression from 13.5 GPa to ambient pressure in the spectral region of 200 – 1000 cm^{-1}. The vertical arrow indicates the experimental sequence.

From the spectrum of the sample after decompression (Figure 3.24), we can only see the bands due to the amorphous material, whereas the initial Raman mode ν_9 due to the zeolite cannot reappear at all, which means the framework of the calcined ZSM-5 has totally collapsed and the PIA is irreversible.

The spectrum of the recovered sample looks the same as that of HDA silica obtained by high-pressure treatment of LDA silica in the previous studies[35, 53, 54] (Figure 3.12 (b)). As mentioned before, the zeolite studied in the present work is only composed of silicon and oxygen atoms, so it is not unreasonable to argue that the calcined siliceous ZSM-5 also experience two amorphous phases in PIA process. (1) The zeolite quickly deforms and starts to form LDA silica at around 1.5 GPa. The zeolite continues to transform to LDA silica with increasing pressure. (2) The LDA silica starts to evolve into HDA silica at around 3 GPa. (3) Only HDA silica exists in the system at around 11 GPa as the PIA is complete.

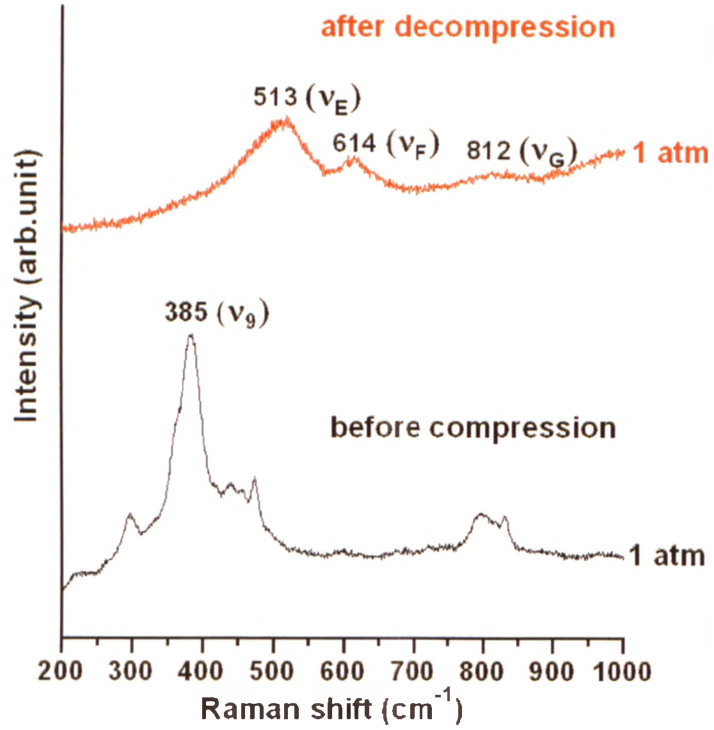

Figure 3.24 Raman spectra of the calcined siliceous ZSM-5 before compression and after decompression

3.3.2.2 IR Spectra of Calcined Siliceous ZSM-5

The IR spectrum of this material at ambient conditions in Figure 3.25 is almost the same as that of the as-made siliceous ZSM-5 (Figure 3.17), since the IR active modes in the spectral region of 200 to 1300 cm^{-1} indicate structural features of zeolite frameworks.[59, 60] Thus, all the bands which are labeled in the spectrum of ambient pressure have the same assignments as those shown in the Table 3.2.

The IR spectra of calcined siliceous ZSM-5 were measured as a function of pressure up to 11.0 GPa at room temperature. The selected spectra in the region of 500 – 1400 cm^{-1} are also shown in Figure 3.25. In the spectrum of 0.6 GPa, the band at 545 cm^{-1} at ambient pressure shifts to 576 cm^{-1}. Since this mode is due to the external vibration related to the linkage of 5MR, the observation indicates that the 5MR in the ZSM-5 framework start deforming.

Similar to as-made ZSM-5, the band at 798 cm^{-1} splits into two components and the new shoulder at about 839 cm^{-1} can be seen in the spectrum of 1.1 GPa, which gradually becomes more resolved upon compression. The appearance of this new band with a similar position to that of the new band seen in the IR spectrum of as-made ZSM-5 indicates the formation of the LDA silica.

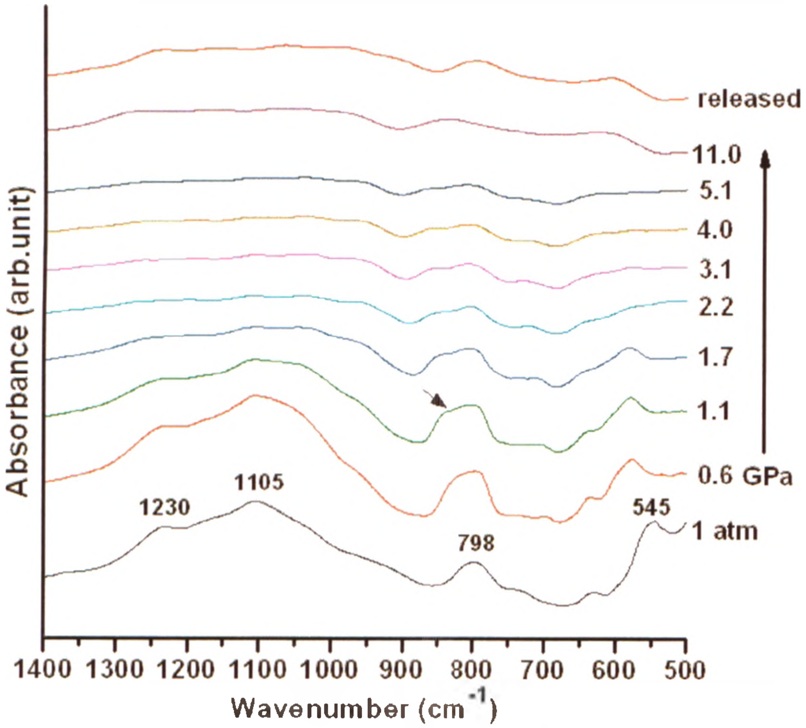

Figure 3.25 Selected IR spectra of the calcined siliceous ZSM-5 on compression in the pressure region 0 – 11.0 GPa in the spectral region of 500 – 1400 cm^{-1}. The vertical arrow indicates the experimental sequence. The small arrow indicates the new band. The released spectrum is the spectrum of the sample recovered from 11.0 GPa.

All the bands quickly become very weak beyond 1.7 GPa. The band at 545 cm^{-1} is invisible at 2.2 GPa. These observations imply that this zeolite transforms to a highly amorphous material above 2.2 GPa. There is no significant change in the spectra between 5.1 and 11.0 GPa except that the overlapping bands merge into one broad envelope at around 837 cm^{-1}.

Upon decompression, the broad bands at about 837 cm^{-1} and 1247 cm^{-1} at 11.0 GPa roughly move back to 797 cm^{-1} and 1238 cm^{-1} at ambient pressure, respectively. The intensities of the other bands increase upon decompression. However, all the bands are still very broad and overlapping, compared to those of the sample before compression. These results mean that the framework of calcined ZSM-5 collapsed under high pressure and cannot be recovered after decompression.

3.3.3 Comparison of the Behaviour of the As-made and Calcined Siliceous Zeolite ZSM-5 under High Pressures and their Reversibility of PIA

The Raman spectra of as-made and calcined siliceous ZSM-5 before compression and after decompression are compared in Figure 3.26. The bands (v_2 and v_9) which are attributed to the ZSM-5 framework vibration at around 380 cm^{-1} in the spectra of the initial samples can be observed clearly, but only a weak signal due to this vibration can be detected in the spectrum of the as-made ZSM-5 after decompression. These observations indicate that only a small amount of HDA silica of the compressed as-made ZSM-5 is converted back to the MFI framework after decompression. This conversion is facilitated by the existence of the occluded TPA^+ cations because the interactions between the TPA^+ and zeolite framework preserve some key local structures associated with the MFI framework structure and these key structural fragments exist in the sample even at 16.3 GPa. Upon releasing pressure, the TPA^+ cations re-direct these local silica units with MFI signature to reform the MFI structure. Similar situation has been found in clathrasil dodecasil-3R (a silica with microporous cavities) with organic molecules (amino-adamantane) in its cages in a previous study.[6] In that study, the compressed sample at 10.3 GPa has partially reverted to the crystalline structure when the pressure is totally removed. In contrast, the HDA phase obtained by compression of calcined ZSM-5 which has no TPA^+ cations is completely preserved upon releasing pressure. Similar result has been shown in a high-pressure study on siliceous zeolite Y whose structure collapses at around 4 GPa and cannot be recovered upon decompression due to the lack of guest species in the framework.[9] Thus, the template molecules play a key role in restoring the original crystalline structure when the pressure is released.

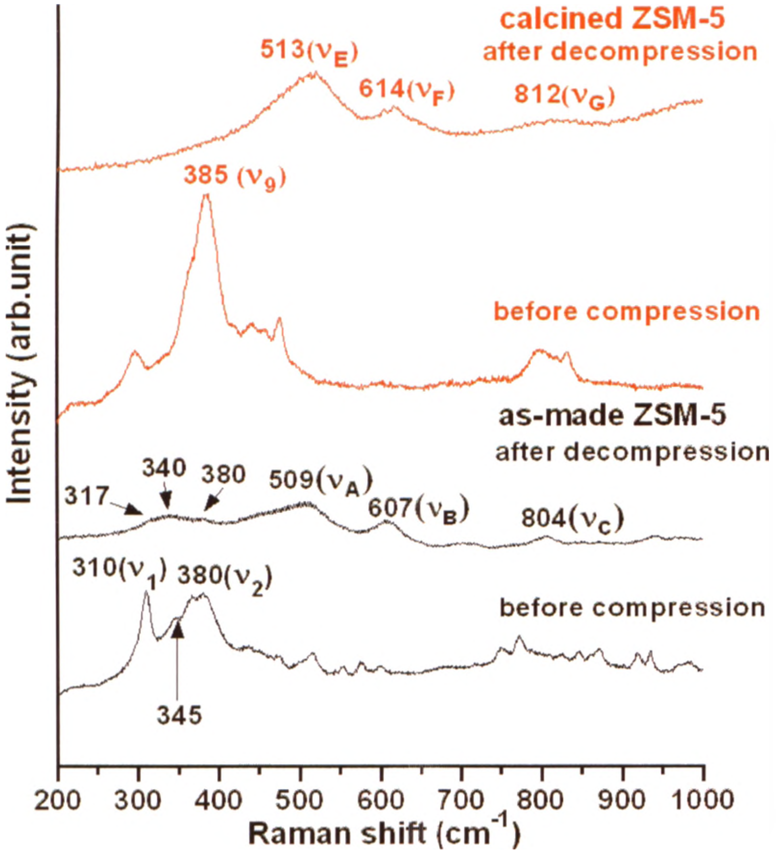

Figure 3.26 Raman spectra of the calcined (red) and as-made (black) siliceous ZSM-5 before compression and after decompression

In the region above 500 cm^{-1}, the positions and profiles of the new peaks of the calcined ZSM-5 (ν_E, ν_F, ν_G) strongly resemble those of the as-made ZSM-5 (ν_A, ν_B, ν_C), which indicates that both as-made and calcined ZSM-5 are transformed to the same HDA material.

PIA has been found to be reversible, or at least partially reversible in some systems,[18, 23, 24] that is, the amorphous phase may revert back to its original crystalline state when the pressure is released. The previous studies[29, 70] have shown that the PIA is not totally reversible above a threshold pressure. In general, for zeolites, the framework topology or the T-O-T connectivity in initial crystalline phase may be preserved in the LDA phase, but lost in the HDA phase.[39] Some authors suggested that amorphization is reversible in the former phase and irreversible in the latter one.[30] In order to determine the reversibility limit of the amorphization process, as-made and calcined siliceous ZSM-5 were first compressed to different pressures, followed by decompression to the ambient pressure.

Raman spectra of the recovered as-made siliceous ZSM-5 samples from different high-pressure experiments are shown in Figure 3.27 and compared with the spectrum of the starting material at ambient pressure. The spectra of the samples recovered from compression to or below around 7 GPa look identical to that of the initial sample before compression. As mentioned before, 7 GPa is the pressure at which the HDA silica is just about to form. The results suggest that the PIA of the as-made siliceous ZSM-5 is totally reversible at around 7 GPa before the formation of HDA phase, i.e. the LDA silica can completely transform back to the MFI structure.

In the spectrum of the sample recovered from 10.2 GPa, all the original peaks show a drastic decrease in the intensity and an increase in the line-width. The ν_2 peak is hardly visible, and the ν_7 and ν_8 peaks severely overlap. These phenomena indicate that a large part of the recovered sample is still amorphous. Thus, the PIA of the sample recovered from 10.2 GPa is only partially reversible. Recovered from 12.6 GPa, all the peaks are broader and weaker than those in the spectra of the sample retrieved from the lower pressure treatments and some peaks look alike to the new bands (ν_A, ν_B, ν_C) in the spectrum of the sample recovered from 16.3 GPa, which implies that a majority of the amorphous materials remain in the recovered sample.

The spectra of the samples recovered from 14.1 and 16.3 GPa are the same, the new bands due to the HDA silica can be seen clearly and the original bands become extremely broad and highly overlapping, suggesting that the recovered sample is highly amorphous only with a very small amount of MFI structure reformed.

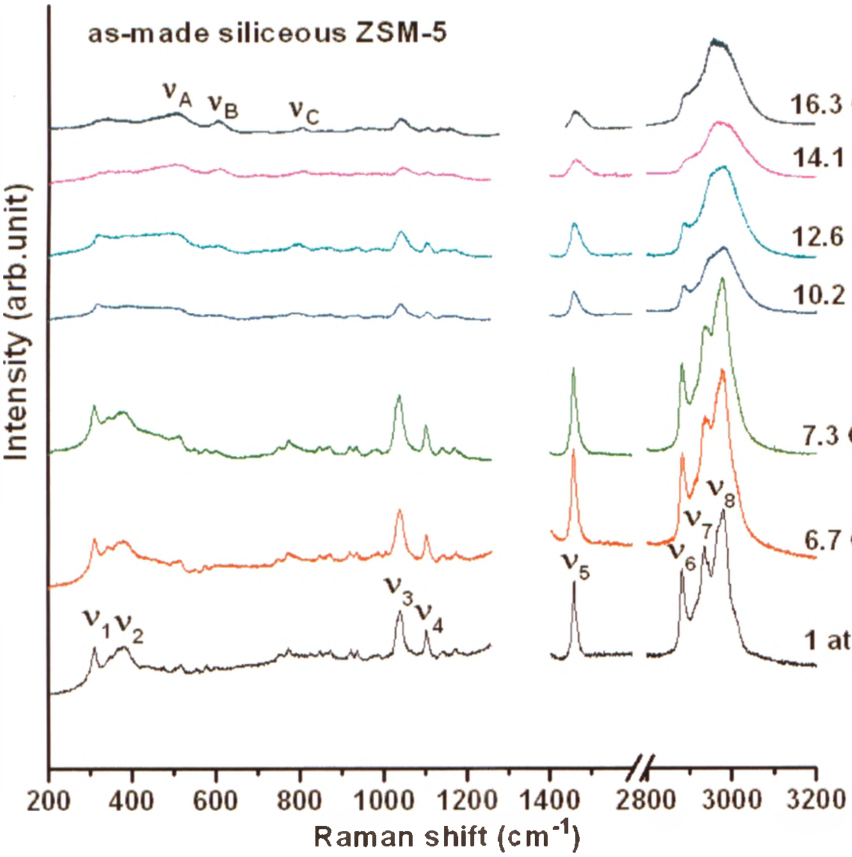

Figure 3.27 Raman spectra of as-made siliceous ZSM-5 samples recovered from different high-pressure runs (maximum pressures are labeled) are compared with the 1 atm spectrum of the sample before compression.

These results demonstrate that the formation of the HDA silica occurs at about 7 GPa and the PIA is only reversible before the appearance of HDA phase. The LDA and HDA silica coexist between 7 and 14 GPa. Above 14 GPa, only the HDA silica exists in the system.

Raman spectra of the recovered calcined siliceous ZSM-5 samples from different high-pressure experiments and the compared spectrum of initial ambient conditions are shown in Figure 3.28. In the spectrum of the sample recovered from 2.7 GPa, all the peaks due to the zeolite framework are just slightly broader and weaker than those of the sample before compression, suggesting the PIA is almost reversible below 3 GPa.

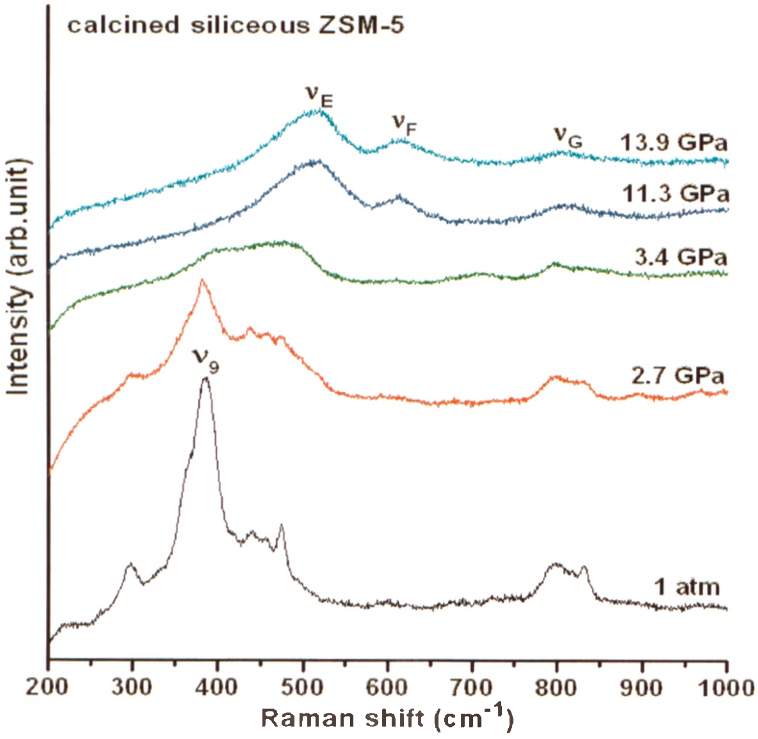

Figure 3.28 Raman spectra of calcined siliceous ZSM-5 samples recovered from different high-pressure runs (maximum pressures are labeled) are compared with the 1 atm spectrum of the sample before compression.

The spectrum of the sample recovered from 3.4 GPa is quite different from that of the noncompressed sample, since all the initial peaks become very broad and weak, especially, the ν_9 peak which overlaps with other peaks due to amorphous silica as a featureless hump. These observations imply that the recovered sample is a mixture of an amorphous phase and the recovered ZSM-5. The PIA is partially reversible after the treatment at the maximum pressure of 3.4 GPa.

The spectra of the samples recovered from 11.3 and 13.9 GPa are the same. The new bands (ν_E, ν_F, ν_G) are clearly visible, whereas all the initial zeolite peaks vanish, suggesting that the starting zeolite becomes completely amorphous after being compressed at the pressures above 11 GPa and the PIA is irreversible at this pressure.

These results indicate that the formation of HDA silica takes place at about 3 GPa for the calcined ZSM-5 and the PIA is reversible before the occurrence of HDA silica; the conversion of LDA to HDA silica finishes at about 11 GPa, above this pressure only the HDA silica exists in the system.

The PIA of the as-made ZSM-5 is reversible in a wider pressure range (0 – 7 GPa) than that of the calcined one (0 – 3 GPa). This is due to that the template molecules in the framework can redirect the silica units produced from the collapsing zeolite structure in the vicinity of the TPA$^+$ cations back to their original positions.

XRD is the most reliable way to determine the reversibility of the sample. The XRD patterns of the recovered as-made siliceous ZSM-5 samples from different high-pressure runs are compared with the pattern of the sample before compression in Figure 3.29. The pattern of the recovered sample treated at 3.7 GPa is almost the same as that of the noncompressed sample, suggesting the recovered sample still maintains its long-range ordering and the PIA is completely reversible.

No obvious difference was detected between the patterns of the sample recovered from 7.3 GPa and the initial sample, which implies that the compressed sample restores the initial crystalline structure and this result is consistent with that from the Raman spectrum of the same pressure in the Figure 3.27. In the pattern of the sample recovered from the highest pressure (14.1 GPa) applied on the as-made ZSM-5, only an extremely weak and broad envelope was noticed, suggesting that the sample is totally amorphous with no crystalline structure being recovered and the PIA is irreversible.

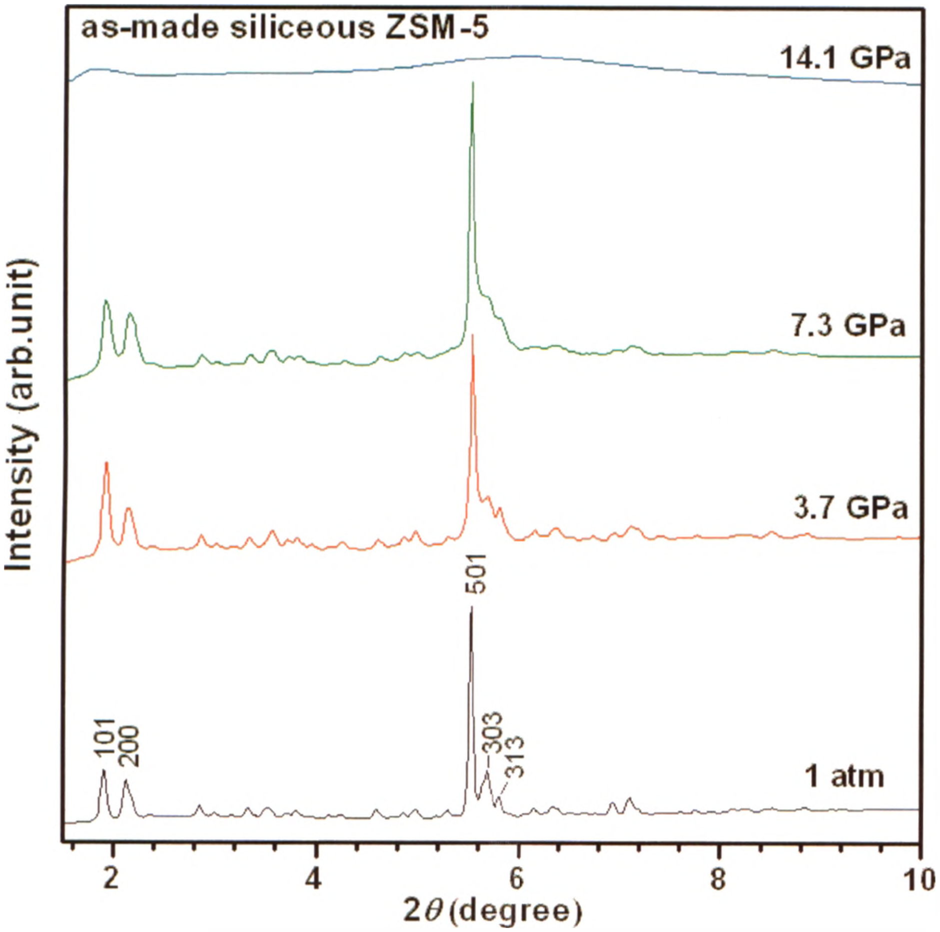

Figure 3.29 XRD patterns of as-made siliceous ZSM-5 recovered from different high-pressure runs (maximum pressures are labeled) are compared with the 1 atm spectrum of the sample before compression.

SEM was used to visualize the effects of different pressures on the sample's morphology. SEM images in Figure 3.30 show the morphologies of the as-made and calcined siliceous ZSM-5 before compression and recovered from different pressures.

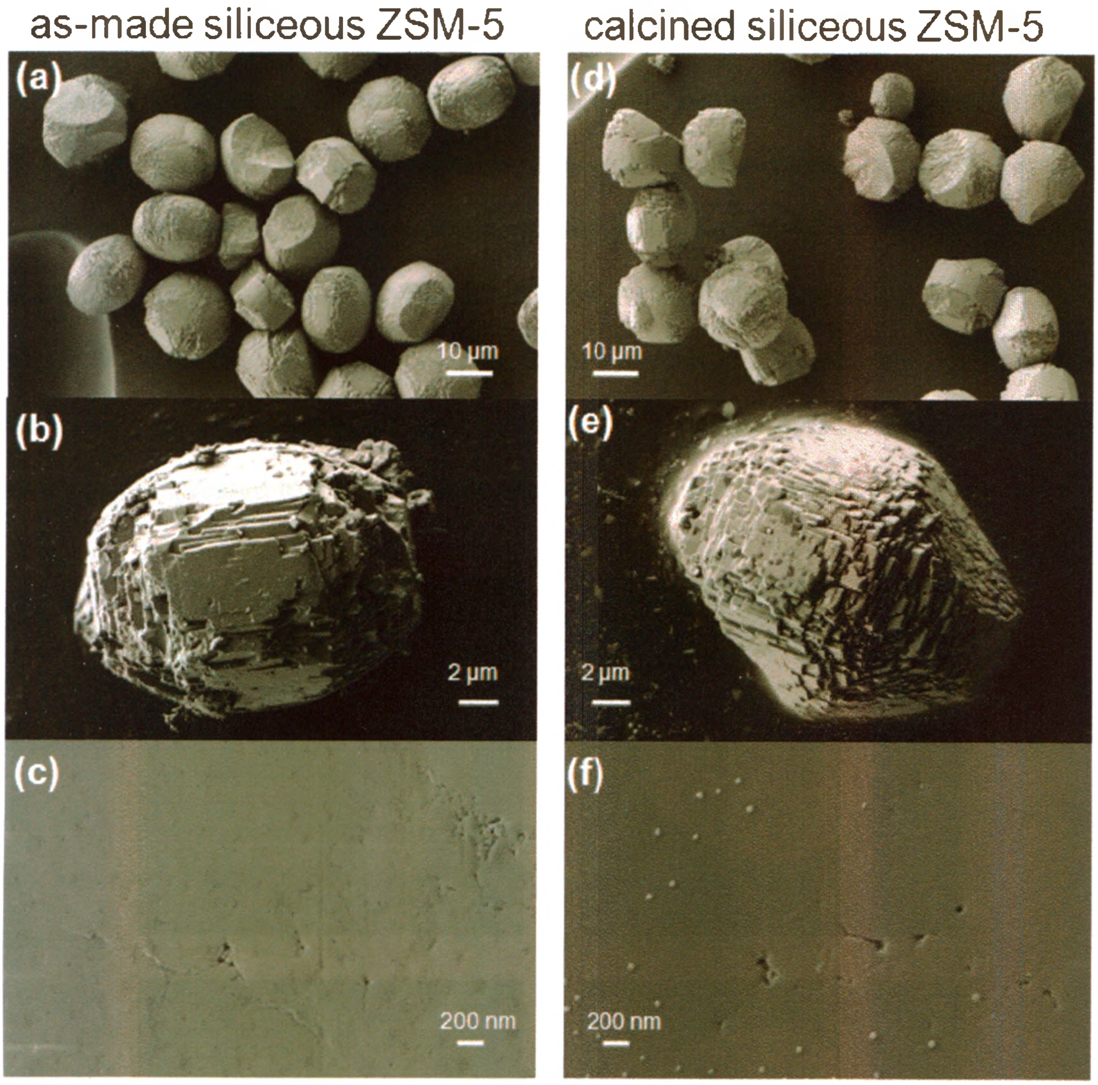

Figure 3.30 Scanning electron micrographs of the morphologies of as-made siliceous ZSM-5 (a) before compression, (b) recovered from 7.3 GPa, (c) recovered from 16.3 GPa, and calcined siliceous ZSM-5 (d) before compression, (e) recovered from 2.7 GPa, (f) recovered from 13.9 GPa (tiny balls on the surface are due to the contaminates from air)

In Figure 3.30 (a), the individual as-made ZSM-5 crystals have a near-ovate shape with the dimension close to 20 µm × 15 µm before compression and the crystals are not transparent in Figure 3.31 (a). After retrieved from 7.3 GPa, some crystals similar to those before compression can still be found in the recovered sample shown in Figure 3.30 (b), suggesting the sample regains its crystalline structure and PIA is reversible at this pressure. Upon releasing the sample from 16.3 GPa, no initial zeolite crystal can be seen (Figure 3.30 (c)), only a large, single amorphous plate with flat and smooth surface forms inside the hole of the gasket and this material is highly transparent (Figure 3.31 (b)), which probably means that the sample has totally lost its crystalline structure and become an amorphous material. Thus, PIA is irreversible around this pressure. The amorphous material with the similar morphology has been found in a high-pressure study of zeolite Y which was compressed to 8 GPa then decompressed.[27]

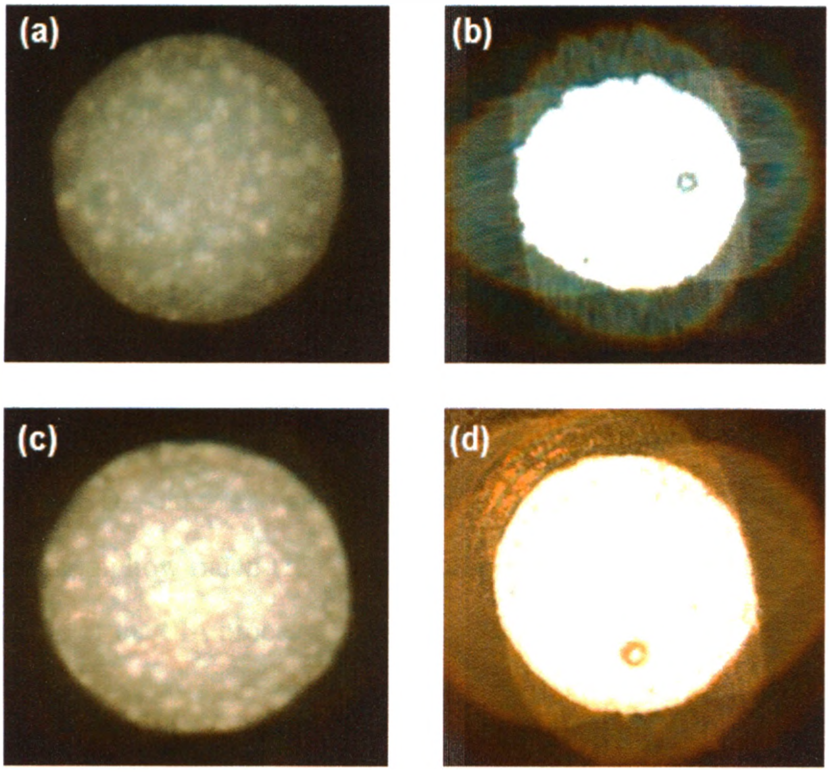

Figure 3.31 Optical micrographs (recorded by a digital camera with the Olympus Microscope) of as-made siliceous ZSM-5 (a) before compression, (b) after recovered from 16.3 GPa and calcined siliceous ZSM-5 (c) before compression, (d) after recovered from 13.9 GPa in the gasket hole using transmitting light for illumination. The chips in the micrographs (b) and (d) are ruby for pressure calibration.

Before compression, the calcined siliceous ZSM-5 crystals shown in Figure 3.30 (d) look similar to those of the as-made ZSM-5. After decompression from 2.7 GPa, the ZSM-5 crystals that look like those before being compressed can still be found in the recovered sample shown in Figure 3.30 (e), indicating that the sample largely recovers its crystalline structure and PIA is reversible at this pressure. For the sample recovered from 13.9 GPa (Figure 3.30 (f)), all the initial zeolite crystals merge into a large, single amorphous plate and this plate also becomes highly transparent (Figure 3.31 (d)), suggesting that the sample has totally lost its crystalline structure and becomes an amorphous material similar to that formed from as-made ZSM-5 under high-pressure treatment. Thus, PIA is irreversible around this pressure.

A comparison of the evolution of the calcined and as-made siliceous ZSM-5 under high pressures suggests that the reversibility of ZSM-5 depends on the existence of template molecules and the maximum pressures applied. PIA is reversible in the LDA phase where the zeolite crystalline topology is preserved but its long-range ordering is lost. The HDA phase, on the other hand, cannot transform back to crystalline ZSM-5 structure, because in HDA phase, the initial zeolite topology is completely lost. Overall, the PIA is irreversible in the HDA phase and partially reversible in the mixture of the LDA and HDA phases, depending on how much HDA silica being formed. The more HDA phase formed the less reversible of the PIA process.

3.4 Conclusions

In the present study, pressure-induced structural evolutions in the completely siliceous as-made and calcined ZSM-5 were investigated in a DAC by Raman and IR spectroscopies, XRD with synchrotron radiation and SEM. As-made siliceous ZSM-5 undergoes two successive phase transitions during the PIA process. Firstly, the crystalline zeolite starts transforming to the LDA silica at around 3 GPa. Between 3 to 7 GPa, as-made

ZSM-5 and LDA silica coexist. The amount of LDA silica gradually increases with increasing pressure. Secondly, the LDA silica starts evolving into the HDA silica at around 7 GPa. For the sample treated at 7 GPa or below, the PIA is reversible. Only the HDA silica exists in the system at around 14 GPa. The HDA silica cannot transform back to the crystalline ZSM-5 upon decompression.

The calcined siliceous ZSM-5 also experiences the PIA and has two amorphous phases. The zeolite deforms as soon as the external pressure is applied. The LDA silica starts forming at around 1.5 GPa. The LDA silica begins to evolve into the HDA silica at around 3 GPa. At this stage, the sample can still recrystallize back to ZSM-5 upon releasing pressure. The LDA phase becomes the HDA silica upon further compression. Above 11 GPa, only the HDA silica exists in the system and the PIA is irreversible.

Comparing the behaviour of the samples under high pressure, we can see that both samples undergo PIA; they gradually transform to LDA silica via rigid rotations of the SiO_4 tetrahedra.[68] The LDA phase is mostly converted to HDA silica at higher pressures when large 10MR of siliceous ZSM-5 collapse to form the smaller rings (3MR and 4MR), leading to a denser amorphous material. However, the threshold pressures of amorphization and polyamorphic transition of the calcined siliceous ZSM-5 are much lower than those of the as-made ZSM-5. The results clearly show that the calcined ZSM-5 deforms more early than the as-made one under the high pressure. This is because the calcined ZSM-5 has no template molecules inside its channels to prevent the 10MR from collapsing.

For both zeolites, the LDA phase can be transformed, at least partially, back to the original crystalline MFI structure. However, the pressure range for this reversible phase transition is much wider for as-made ZSM-5 (0 – 7 GPa) than that for the calcined one (0 – 3 GPa), indicating that the TPA^+ cations also act as 'organizing centers' to redirect the silica fragments with zeolite formwork signature to reform the MFI topology.[6] The results also demonstrate that the PIA is irreversible in the HDA phase. For the sample which is a mixture of the amorphous phases, the more HDA silica formed in the sample the less reversible of the PIA process. In general, the reversibility of this zeolite largely depends on the existence of template cations (TPA^+) and the maximum pressures applied.

3.5 References

[1]H. Van Bekkum, E. Flanigen, P. Jacobs and J. Jansen, *Introduction to Zeolite Science and Practice, 2nd Completely revised and Expanded Edition*, 2001.
[2]J. Nagy, P. Bodart, I. Hannus and I. Kiricsi, *Synthesis, characterization and use of zeolitic microporous materials*, DecaGen Szeged-Szoreg, Hungary, 1998.
[3]R. Xu, *Chemistry of Zeolites and Related Porous Materials: Synthesis and Structure*, Wiley-Interscience, 2007.
[4]P. Wright, *Microporous framework solids*, Royal Society of Chemistry, 2008.
[5]R.M. Hazen, Science, 219 (1983) 1065.
[6]J.S. Tse, D.D. Klug, J.A. Ripmeester, S. Desgrenlers and K. Lagarec, Nature, 369 (1994) 724.
[7]Y. Lee, J.A. Hriljac, T. Vogt, J.B. Parise, M.J. Edmondson, P.A. Anderson, D.R. Corbin and T. Nagai, J. Am. Chem. Soc., 123 (2001) 8418.
[8]Y. Lee, T. Vogt, J.A. Hriljac, J.B. Parise, J.C. Hanson and S.J. Kim, Nature, 420 (2002) 485.
[9]E.A. Havenga, Y. Huang and R.A. Secco, Materials Research Bulletin, 38 (2003) 381.
[10]R.A. Secco, S.V. Goryainov and Y. Huang, Physica Status Solidi B Basic Solid State Physics, 242 (2005) R73.
[11]G.N. Greaves, F. Meneau, F. Kargl, D. Ward, P. Holliman and F. Albergamo, J. Phys.: Condens. Matter, 19 (2007) 415102/1.
[12]S. Ori, S. Quartieri, G. Vezzalini and V. Dmitriev, Am. Mineral., 93 (2008) 53.
[13]R. Arletti, O. Ferro, S. Quartieri, A. Sani, G. Tabacchi and G. Vezzalini, Am. Mineral., 88 (2003) 1416.
[14]J.A. Hriljac, Crystallogr. Rev., 12 (2006) 181.
[15]R.M. Hazen and L.W. Finger, Phase Transitions, 1 (1979) 1.
[16]Y. Lee, H.H. Lee, D.R. Lee, T.J. Shin, J.-Y. Choi and C.-C. Kao, J. Am. Chem. Soc., 129 (2007) 4888.
[17]R.A. Secco, M. Rutter and Y. Huang, Technical Physics (Translation of Zhurnal Tekhnicheskoi Fiziki), 45 (2000) 1447.
[18]Y. Huang and E.A. Havenga, Chem. Phys. Lett., 345 (2001) 65.
[19]O. Mishima, L.D. Calvert and E. Whalley, Nature, 310 (1984) 393.

[20]H. Mao, R.J. Hemley and E.C.T. Chao, Scanning Microsc., 1 (1987) 495.

[21]R.J. Hemley, A.P. Jephcoat, H.K. Mao, L.C. Ming and M.H. Manghnani, Nature, 334 (1988) 52.

[22]Q. Williams and R. Jeanloz, Nature, 338 (1989) 413.

[23]S.M. Sharma and S.K. Sikka, Progress in Materials Science, 40 (1996) 1.

[24]M.D. Rutter, T. Uchida, R.A. Secco, Y. Huang and Y. Wang, Journal of Physics and Chemistry of Solids, 62 (2001) 599.

[25]J. Gulin-Gonzalez and G.B. Suffritti, Microporous Mesoporous Mater., 69 (2004) 127.

[26]S.V. Goryainov and M.B. Smirnov, Eur. J. Mineral., 13 (2001) 507.

[27]G.N. Greaves, F. Meneau, A. Sapelkin, L.M. Colyer, I. ap Gwynn, S. Wade and G. Sankar, Nat. Mater., 2 (2003) 622.

[28]C. Sanchez-Valle, A.D. Lethbridge Zoe, V. Sinogeikin Stanislav, J. Williams Jennifer, I. Walton Richard, E. Evans Kenneth and D. Bass Jay, J Chem Phys, 128 (2008) 184503.

[29]J. Zhang, Y. Zhao, H. Xu, M.V. Zelinskas, L. Wang, Y. Wang and T. Uchida, Chem. Mater., 17 (2005) 2817.

[30]M.H. Cohen, J. Iniguez and J.B. Neaton, J. Non-Cryst. Solids, 307-310 (2002) 602.

[31]J. Gulin Gonzalez, A. Dorta-Urra, P. Demontis and G.B. Suffritti, Microporous Mesoporous Mater., 123 (2009) 30.

[32]Y. Huang, J. Mater. Chem., 8 (1998) 1067.

[33]F. Meneau and G.N. Greaves, Nucl. Instrum. Methods Phys. Res., Sect. B, 238 (2005) 70.

[34]G.N. Greaves, F. Meneau, O. Majerus, D.G. Jones and J. Taylor, Science, 308 (2005) 1299.

[35]B. Champagnon, C. Martinet, M. Boudeulle, D. Vouagner, C. Coussa, T. Deschamps and L. Grosvalet, J. Non-Cryst. Solids, 354 (2008) 569.

[36]O. Mishima, L.D. Calvert and E. Whalley, Nature, 314 (1985) 76.

[37]S. Aasland and P.F. McMillan, Nature, 369 (1994) 633.

[38]M.C. Wilding, M. Wilson and P.F. McMillan, Chem. Soc. Rev., 35 (2006) 964.

[39]I. Peral and J. Iniguez, Phys. Rev. Lett., 97 (2006) 225502/1.

[40]E. Fois, A. Gamba, G. Tabacchi, R. Arletti, S. Quartieri and G. Vezzalini, Am. Mineral., 90 (2005) 28.

[41]S.A. Tabak and S. Yurchak, Catal. Today, 6 (1990) 307.

[42]T.F. Degnan, G.K. Chitnis and P.H. Schipper, Microporous Mesoporous Mater., 35-36 (2000) 245.

[43]F. Bosselet, M. Sacerdote, J. Bouix and B.F. Mentzen, Mater. Res. Bull., 25 (1990) 443.

[44]O. Oehrman and J. Hedlund, Microporous Mesoporous Mater., 91 (2006) 312.

[45]X. Zou, G. Zhu, H. Guo, X. Jing, D. Xu and S. Qiu, Microporous Mesoporous Mater., 124 (2009) 70.

[46] C.S. Cundy and P.A. Cox, Microporous Mesoporous Mater., 82 (2005) 1.

[47] I. Diaz, E. Kokkoli, O. Terasaki and M. Tsapatsis, Chem. Mater., 16 (2004) 5226.

[48] X. Liu, W. Su, Y. Wang and X. Zhao, J. Chem. Soc., Chem. Commun., (1992) 902.

[49] C. Bremard, J. Laureyns and J. Patarin, J. Raman Spectrosc., 27 (1996) 439.

[50] J.R. Bartlett, R.P. Cooney and D.M. Bibby, Studies in Surface Science and Catalysis, 36 (1988) 609.

[51] P. Richet and P. Gillet, Eur. J. Mineral., 9 (1997) 907.

[52] P.K. Dutta and M. Puri, J. Phys. Chem., 91 (1987) 4329.

[53] R.J. Hemley, H.K. Mao, P.M. Bell and B.O. Mysen, Phys. Rev. Lett., 57 (1986) 747.

[54] M. Grimsditch, Phys. Rev. Lett., 52 (1984) 2379.

[55] N. Chiodini, F. Meinardi, F. Morazzoni, A. Paleari, R. Scotti and G. Spinolo, Solid State Communications, 109 (1998) 145.

[56] A. Pasquarello and R. Car, Phys. Rev. Lett., 80 (1998) 5145.

[57] N.N. Ovsyuk and S.V. Goryainov, JETP Letters, 83 (2006) 109.

[58] A. Isambert, E. Angot, P. Hebert, J. Haines, C. Levelut, R. Le Parc, Y. Ohishi, S. Kohara and D.A. Keen, J. Mater. Chem., 18 (2008) 5746.

[59] C.L. Angell, J. Phys. Chem., 77 (1973) 222.

[60] E.M. Flanigen, H. Khatami and H.A. Szymanski, Advan. Chem. Ser., 101 (1971) 201.

[61] G. Coudurier, C. Naccache and J.C. Vedrine, J. Chem. Soc., Chem. Commun., (1982) 1413.

[62] A. Miecznikowski and J. Hanuza, Zeolites, 7 (1987) 249.

[63] P.K. Dutta, K.M. Rao and J.Y. Park, J. Phys. Chem., 95 (1991) 6654.

[64] P.A. Jacobs, H.K. Beyer and J. Valyon, Zeolites, 1 (1981) 161.

[65] J.C. Jansen, F.J. Van der Gaag and H. Van Bekkum, Zeolites, 4 (1984) 369.

[66] G.-J. Su and J. Bock, *Interpretation of the infrared spectra of fused silica*, Univ. of Rochester, Rochester, NY, USA., 1968, p. 56 pp.

[67] Q. Williams and R. Jeanloz, Science, 239 (1988) 902.

[68] H. Xu, J. Zhang, Y. Zhao, G.D. Guthrie, D.D. Hickmott and A. Navrotsky, Am. Mineral., 92 (2007) 166.

[69] K.J. Kingma, C. Meade, R.J. Hemley, H. Mao and D.R. Veblen, Science, 259 (1993) 666.

[70] I. Daniel, P. Gillet, P.F. McMillan, G. Wolf and M.A. Verhelst, J. Geophys. Res., [Solid Earth], 102 (1997) 10313.

Chapter 4 A Preliminary Investigation of the Crystallization of $AlPO_4$-16 Molecular Sieve by Dry Gel Conversion Method

4.1 Introduction

Zeolites and aluminophosphate ($AlPO_4$)-based molecular sieves have been widely used as ion-exchangers, catalysts and sorbents in industry due to their unique properties[1] and they have many new applications in various technologies recently.[2] Although numerous progresses have been made to understand the major principles underlying the formation of these materials under hydrothermal synthesis (HTS) conditions,[3-5] the crystallization mechanisms are still not yet totally understood on a molecular level. Therefore, the rational design of novel frameworks with desired properties is still difficult. The difficulties in investigating crystallization mechanism originate from the fact that HTS is an extremely complicated process with multiple-component reactions and chemical equilibria occurring in both liquid and solid phases at the same time.[4, 5] Another problem is that it is difficult to identify and subsequently characterize the true intermediates of the final crystalline molecular sieves. The intermediates or precursors are generally obtained by quenching the reactions followed by isolation of solids from the liquid phase. Thus, their true structures may be altered by posts-synthesis treatments[5-8] such as washing.

Recently, dry gel conversion (DGC) method[8-11] has been developed as an alternative approach for molecular sieve synthesis. This method transforms pre-dried gel powder to a crystalline microporous material at elevated temperatures and pressures. It can be further divided into two related methods (see Figure 1.5): (1) steam-assisted conversion (SAC) method, in which the pre-dried gel powders containing structure directing agent (SDA) are physically separated from a very small amount of pure water in an autoclave. (2) Vapour phase transport (VPT) method, which is similar to SAC except that the SDA is not contained in the initial dry gel. Instead, a small amount of SDA aqueous solution is placed at the bottom of the autoclave. The methods are well-suited for studying the crystallization mechanisms because the reaction systems are simpler. For SAC, which is the method used in the present study, all the reactive species are contained in the solid phases (dry gel) with a small amount of distilled water separated from them, avoiding the direct contact between the reactive species in solution and solid gel as the situation occurring in HTS conditions. Although the potential of DGC for the study of zeolite crystallization mechanism was previously recognized,[8, 10] there have been relatively few studies that directly focused on the crystallization process.[12-14]

In this chapter, we show that SAC can be used as an effective method to synthesize molecular sieves and to investigate the formation of molecular sieves by capturing the reactive intermediates. The system selected to study is $AlPO_4$-16, a representative $AlPO_4$-based microporous material that was first synthesized by Union Carbide in the 1980s.[15]

$AlPO_4$-16 has AST type structure containing two types of polyhedra, the large truncated rhombododecahedral $[4^6 6^{12}]$ (six 4-membered rings and twelve 6-membered rings (6MR)) and the small hexahedral $[4^6]$ cages (double 4-rings). The resulting structure has no real channel system and the largest pore opening is a 6-membered ring[16] (Figure 4.1 (a)). The Al/P mole ratio of this material is equal to one. Both cubic and tetragonal structures of $AlPO_4$-16 have two distinct tetrahedral sites with a distribution of 4:1 for T_1 and T_2 (T = Al or P) determined by theoretical and experimental studies[16-18] (Figure 4.1 (b), (c)). T_1 and T_2 sites are located on the small and large types of polyhedra, respectively.

AlPO$_4$-16 was initially synthesized by using quinuclidine (Q), an organic amine as template under the HTS conditions.[15] Without fluoride anions (F^-) which are used as mineralizing agents to balance the charge of protonated Q in reactants, the structure of as-made AlPO$_4$-16 was indexed in a cubic cell (space group F23, a = 13.3832(6) Å).[16] On the other hand, with F^-, the structure of as-made AlPO$_4$-16 was indexed in a tetragonal cell (space group I$\bar{4}$, a = 9.3423(1) Å, c = 13.4760(2) Å). Upon removal of the organic template and of fluoride by calcination, the cubic form of AlPO$_4$-16 can be obtained from the tetragonal form. The reason for the symmetry lowering is not quite clear now, but it is not simply due to the incorporation of F^-.[19, 20]

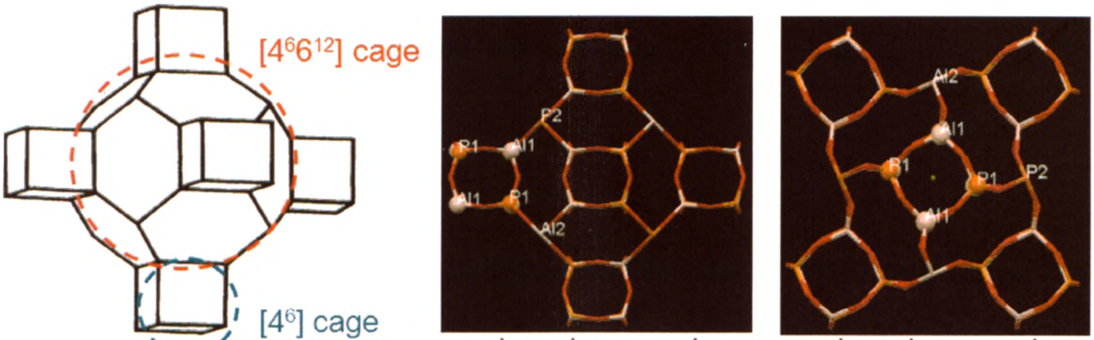

(a) view along *c* axis (b) view along *c* axis (c)

Figure 4.1 (a) The ideal framework topology of AlPO$_4$-16 with two types of cages labeled (Adapted from Ref. 16); (b) cubic form and (c) tetragonal form of AlPO$_4$-16 with the two types of tetrahedral framework sites labeled.

Octadecasil,[21] a clathrate-type inclusion compound, is the all-silica counterpart of the AlPO$_4$-16 with the same AST type structure. The symmetry of octadecasil determined by XRD is tetragonal (space group I4/m). Octadecasil needs to be synthesized in fluoride media, and the position of F^- within the framework has been studied by several groups using solid state ^{19}F, ^{29}Si NMR.[22-24] It can be used as a catalyst in industry, and recently some new metal organic frameworks which can be used as heterogeneous catalysts have been built up from the octadecasil zeolitic cages.[25]

$AlPO_4$-16 can be synthesized by various templates usually with the help of F^-.[18, 26] Hexamethyleneimine (HEX) was used as a template to synthesize $AlPO_4$-16 by HTS method.[27, 28] Since $AlPO_4$-16 being first synthesized until now, there have been only a few reports in the literature related to this material, most of which emphasized the structure of this material, the roles of the templates and F^- in $AlPO_4$-16 synthesis and the positions of the templates and F^- within $AlPO_4$-16.[16-18] To our knowledge, no research concentrating on the crystallization of this material has been done even under the traditional HTS method. In the present study, we examined the formation of $AlPO_4$-16 under DGC conditions using HEX as a SDA in the absence of F^-. The aim of this study is to gain some insight into the synthesis and the crystallization of $AlPO_4$-16 under SAC conditions.

4.2 Experimental Section

The detailed procedures of sample preparation and characterizations are described in chapter 2 (pages 42 – 44).

4.3 Results and Discussion

4.3.1 Powder XRD Studies

In order to observe possible intermediates in $AlPO_4$-16's crystallization process, a series of samples was made at certain temperatures with increasing crystallization time. Powder XRD was used to follow the evolution of the long-range ordering of the dry gel as a function of crystallization time. Figure 4.2 shows the powder XRD patterns of pseudoboehmite (Catapal B) which is used as aluminum source, initial SAC dry gel without heating and the gel samples obtained by quenching the reaction at different time. The white pseudoboehmite powders give four broad peaks at 2θ values of 16.1, 32.7, 44.8 and 57.8°, which are consistent with those reported in a previous study.[28] The initial SAC dry gel is yellowish glassy chip-like before ground, and the colour probably comes from the template (HEX). The pattern of the initial dry gel also contains the broad peaks due to the unreacted alumina. But a new broad peak with a low 2θ value of 6.6° appears in the pattern, indicating that structural reorganization within the amorphous phase occurs and a layered intermediate phase forms. With increasing reaction time, the samples heated between 10 to 40 min do not show obvious difference in their XRD patterns except that the peak due to the layered material is gradually moving to a lower 2θ angle, which means the d-spacing of the layered phase increases.

The XRD pattern of 50 min sample is mainly dominated by the reflections associated with $AlPO_4$-16.[16] In addition, the two strong sharp reflections appear at 7.0 and 9.1° (marked with ★) and they belong to by-product with an unknown structure. The pattern also indicates that the $AlPO_4$-16 synthesized under DGC conditions has the cubic form. The bumpy baseline of the pattern implies the sample also contains some amorphous materials which are probably belong to the unreacted alumina and layered phase. The pattern of the 60 min sample looks the same as that of the 50 min one. The colour of all the as-made samples is yellowish.

To investigate the property of the crystalline by-product and to obtain the pure $AlPO_4$-16, we synthesized the samples with longer reaction time. The results are also shown in Figure 4.2. The XRD pattern of 2 hour sample is similar to that of the 60 min one, but the pattern of 6 hour sample contains some weak reflections of impurities which probably belong to $AlPO_4$-5, $AlPO_4$-22 and other aluminophosphates.[27] For 18 hour sample, the intensities of the impurities (marked with ◆) clearly increase; however, the reflections of the by-product cannot be suppressed by increasing the reaction time. This indicates that this species is a competing phase not an intermediate.

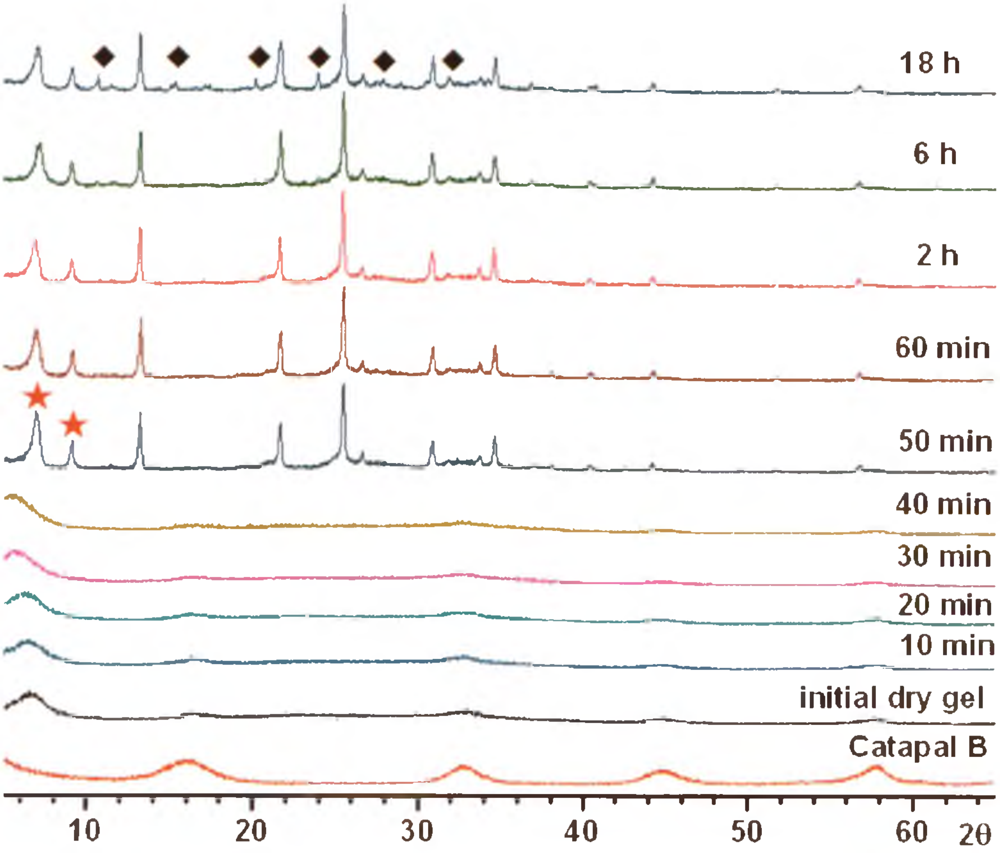

Figure 4.2 Powder XRD patterns of aluminum source and SAC dry gel samples heated at 200 °C

In order to slow down the reaction, we conducted the same experiment, but at a lower reaction temperature (170 °C). The XRD patterns (Figure 4.3) show that lowering reaction temperature only delayed the formation of $AlPO_4$-16 for 10 minutes. No new intermediate shows up before the occurrence of $AlPO_4$-16 and no other impurity (except that the same by-product) can be detected in all the samples heated from 60 to 120 min. Thus, there is no significant difference in the reactions at 200 and 170 °C. The $AlPO_4$-16 still forms quickly. As a result, increasing reaction time or decreasing reaction temperature cannot reveal more information on the crystallization process of $AlPO_4$-16.

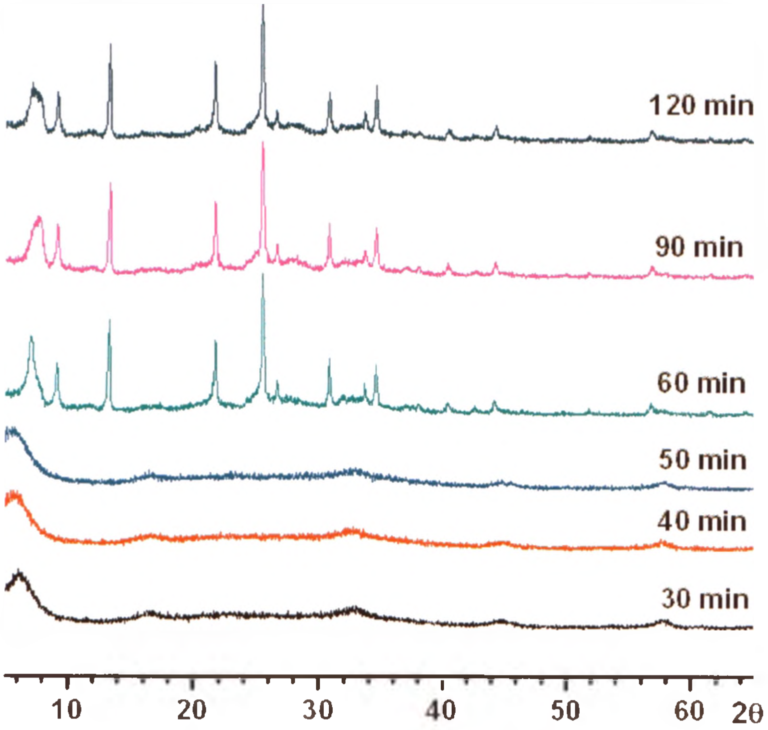

Figure 4.3 Powder XRD patterns of SAC dry gel samples heated at 170 °C

To ensure that the semi-crystalline layered phase in the dry gel samples is a true intermediate, a representative sample (200 °C 30 min sample) at an early stage of the crystallization was reheated in the Teflon cup at 200 °C for 1 hour in the presence of 0.3 g distilled water at the bottom of the autoclave. This sample transformed into $AlPO_4$-16 with the by-product (Figure 4.4), and the pattern of it looks almost the same as that of the 200 °C 60 min sample, confirming that the layered phase is indeed a true reactive intermediate of $AlPO_4$-16.

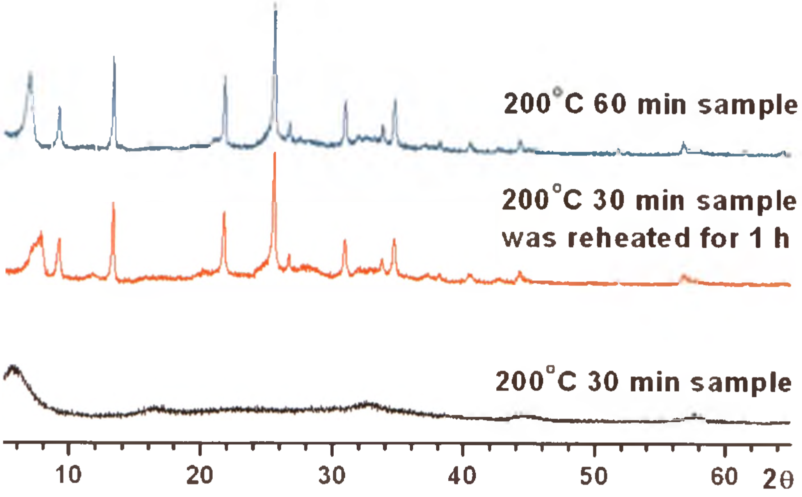

Figure 4.4 Powder XRD patterns of 200 °C 30 min sample before and after reheated for 1 hour and 200 °C 60 min sample

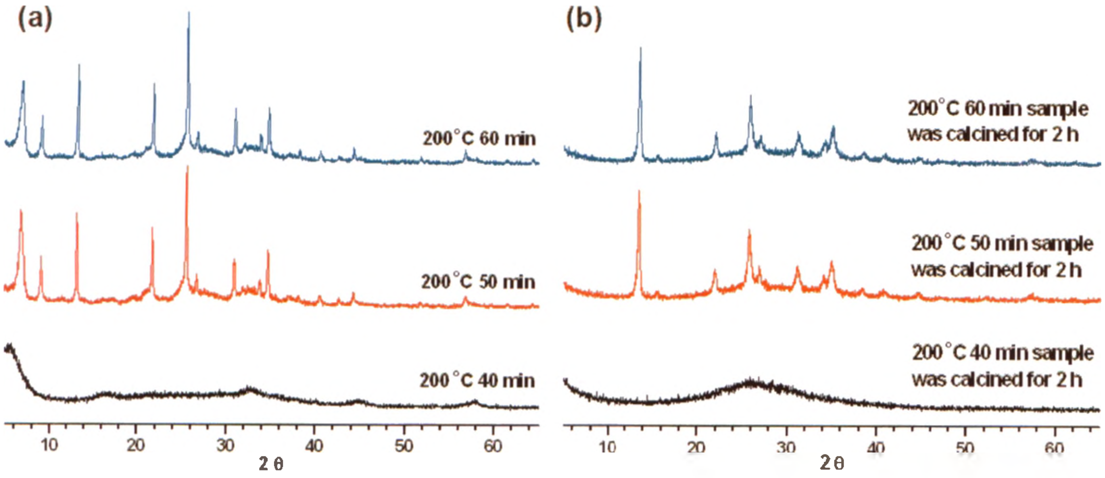

Figure 4.5 Powder XRD patterns of selected 200 °C samples (a) before and (b) after calcination

In order to gain pure $AlPO_4$-16 by post-synthesis treatment, some selected samples crystallized at 200 °C were calcined at 550 °C for 2 hours (Figure 4.5). The structure of 40 min yellowish layered sample has totally collapsed to a black amorphous phase after calcination since the broad low-angle reflection has disappeared and only a broad envelope can be seen at 2θ value of 26.5°.

The XRD patterns of 50 min and 60 min samples after calcination are identical and neither has the reflections from the by-product. The colour of the samples turns to dark grey. It seems that calcination leads to the pure cubic form of $AlPO_4$-16. However, the intensities of the reflections of $AlPO_4$-16 are much weaker than those of the samples before calcination, indicating a decrease in crystallinity. It appears that a part of these samples, presumably the by-product, has transformed to amorphous materials.

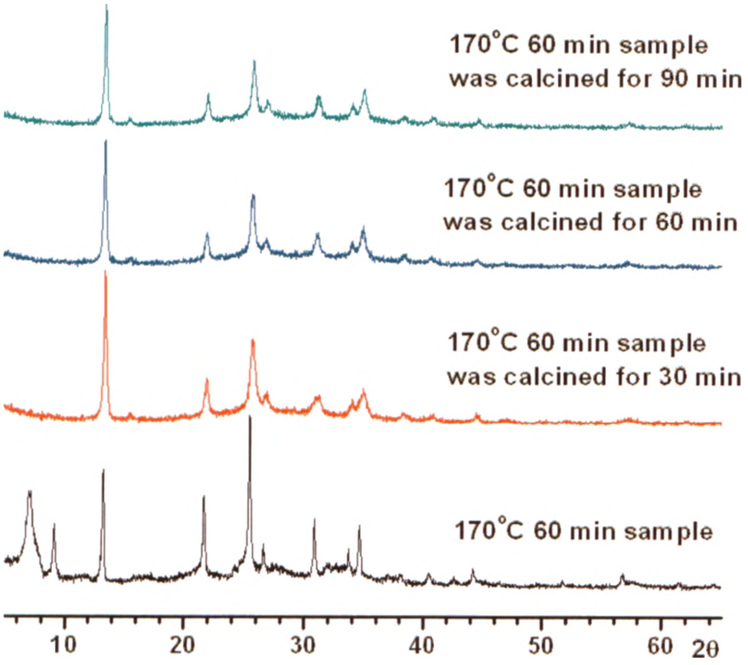

Figure 4.6 Powder XRD patterns of 170 °C 60 min sample calcined for different time

To check when the by-product was removed, we calcined the 60 min sample which was synthesized at 170 °C for various times (Figure 4.6). The patterns show that the structure of the by-product has decomposed completely under calcination for just 30 minutes. There is no noticeable difference among the patterns of the samples with increasing calcination time up to 2 hours.

The as-made sample was washed with distilled water using a centrifuge in order to determine whether or not the by-product can be removed by washing. The selected as-made sample is the 50 min sample synthesized at 200 °C and the XRD patterns of washed and unwashed samples are shown in Figure 4.7. The reflections of the by-product disappear upon washing. Moreover, the reflections of $AlPO_4$-16 of the washed sample which becomes a white powder are sharper than those of the calcined and unwashed sample, implying that the three-dimensional framework of $AlPO_4$-16 has not broken down and the by-product can be removed by distilled water.

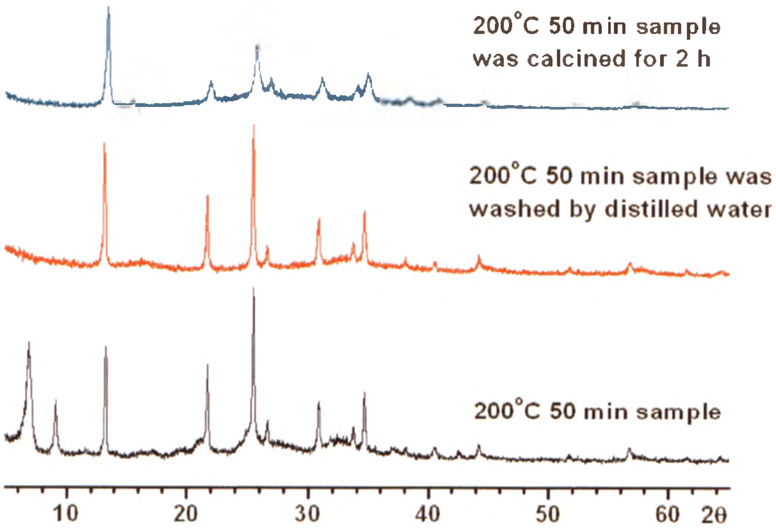

Figure 4.7 Powder XRD patterns of 50 min sample before and after different post-synthesis treatments

To determine whether the by-product was dissolved in distilled water or simply washed away by the water due to its small particle size, a selected sample (200 °C 60 min sample) was washed by water in a beaker and then dried in the same beaker in air without isolation from the liquid phase. This ensures that no solid particles will be washed away. After dried in air for 2 days, the colour of the washed sample is whiter than that of the as-made one and looks quite like the similar sample (200 °C 50 min sample) washed using a centrifuge. The XRD patterns also show much similarity between these two washed samples by different methods (Figure 4.8 (c) and (d)). Thus, we believe that the by-product can be dissolved in distilled water. Previous work showed that some reaction's intermediates are held together by weak bonding interactions.[14, 29] Thus, the present results suggest that the ordered structure of the by-product is probably also held by weak forces such as hydrogen bonding and van der Waals forces. Washing changes these weak interactions, resulting in the transformation to amorphous materials.

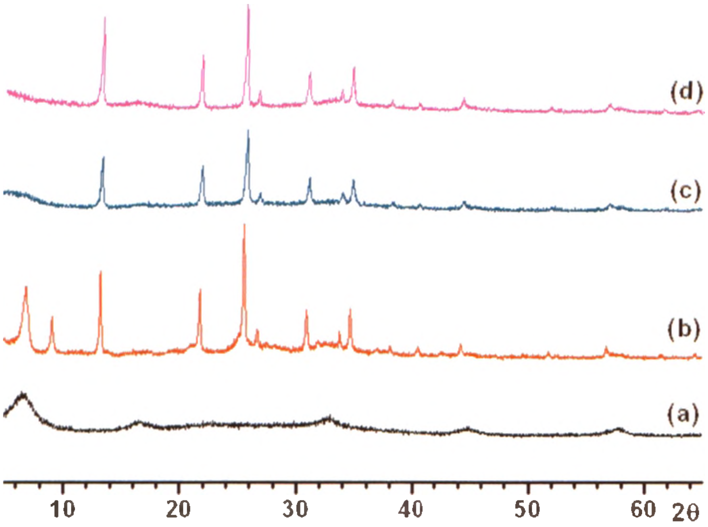

Figure 4.8 A comparison of powder XRD patterns of selected samples washed by distilled water using different methods (a) initial dry gel; (b) as-made 200 °C 60 min sample; (c) washed 200 °C 60 min sample in a beaker; (d) washed 200 °C 50 min sample by a centrifuge

To check whether the layered intermediate phase corresponding to the broad peak at a low 2θ value of 6.6° in the XRD pattern of the initial dry gel can also be removed by distilled water, the dry gel powders were washed by distilled water in a beaker without isolation and dried in air. The appearance of the washed dry gel is the same as the unwashed one which is yellowish glassy chip-like. There is no difference in the XRD patterns of both samples (Figure 4.9). Thus, the layered intermediate phase cannot be removed by distilled water under these conditions. Since previous work[29] showed that the structure of the similar semi-crystalline layered intermediates of $AlPO_4$-based molecular sieves are held by weak bonding, a possible reason leading to the result is that a part of weak bonds in this layered intermediate may be broken by water, but they reform with the help of the template (HEX) and other nutrients in the beaker after the additional water evaporated.

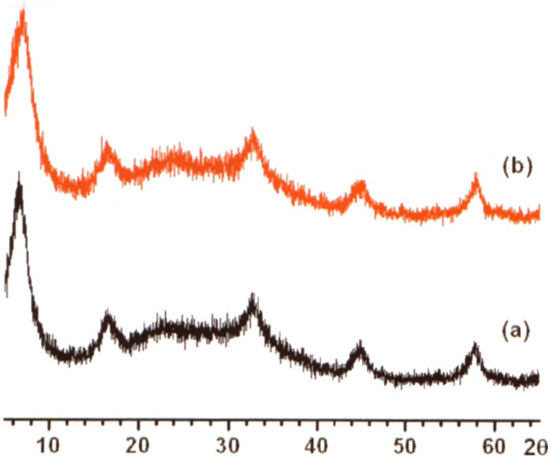

Figure 4.9 Powder XRD patterns of (a) initial dry gel and (b) dry gel washed by distilled water in a beaker

To further confirm the argument, the initial dry gel was washed with distilled water using a centrifuge. After being dried in air, the dry gel becomes a fine white powder. The XRD pattern of the washed dry gel is similar to that of the aluminum source and the broad peak at a low 2θ value disappears (Figure 4.10), which means that the layer intermediate phase in the initial dry gel has largely decomposed and cannot be recovered without enough template and other species such as phosphorus source in the system. Thus, it is reasonable to suggest that the dry gel washed by distilled water using a centrifuge cannot undergo further reaction to form $AlPO_4$-16. Indeed, the XRD pattern of the sample obtained by heating the centrifuge-washed dry gel at 200 °C for 60 min (Figure 4.11 (c)) shows no $AlPO_4$-16 or other crystalline product. The majority of the template and other reactive species within the initial dry gel are probably removed from the system when the mother liquor is decanted. Thus, the weak bonds of the layered intermediate phase broken by washing can no longer be reformed due to the loss of significant portion of HEX and other reactive species.

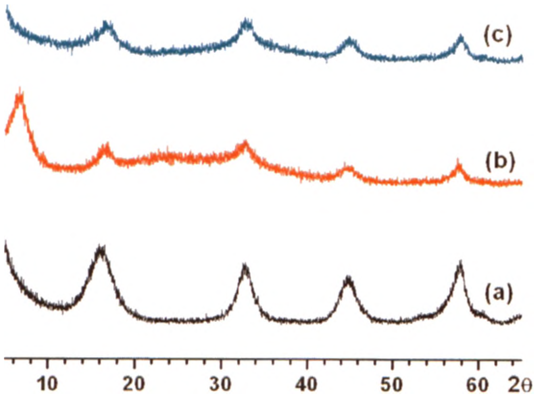

Figure 4.10 Powder XRD patterns of (a) aluminum source, (b) initial dry gel and (c) dry gel washed by distilled water using a centrifuge

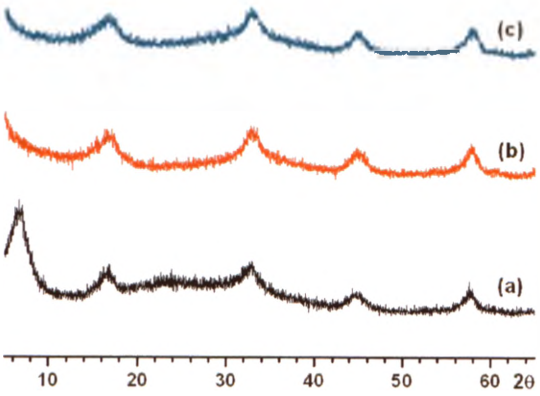

Figure 4.11 Powder XRD patterns of (a) initial dry gel, (b) dry gel washed by distilled water using a centrifuge, and (c) sample of (b) heated at 200 °C for 60 min under SAC conditions

4.3.2 Solid-State NMR Studies

To gain an insight into the crystallization process at a molecular level, ^{31}P and ^{27}Al MAS NMR techniques were applied to obtain the short-range information on the structures of the intermediate phases, $AlPO_4$-16 and the by-product. The ^{31}P MAS spectra of the initial SAC dry gel and selected gel samples heated at 200 °C are shown in Figure 4.12. For the initial dry gel, a resonance centered at around –5 ppm can be observed, accompanied by a very broad shoulder at about –12 ppm. The –5 ppm peak is likely due to an amine-phosphate species which can exist in the AlPO gel.[30] In the previous study of synthesis of $AlPO_4$-based molecular sieves, the broad ^{31}P resonance signals were often observed in the range –10 to –20 ppm for the gel samples obtained at the early stages of the crystallization, and they are usually assigned to the P sites which are in the amorphous aluminophosphate materials.[31-33] Thus, the chemical shift indicates that the –12 ppm shoulder might be attributed to tetrahedral environment of P sites in the AlPO species (amorphous phase and semi-crystalline layered phase) and that the P atoms are not fully condensed (i.e. the number of Al atoms in the second coordination sphere is less than four, such as $P(-OAl)_3(OH)$ and $P(-OAl)_2(OH)_2$).

As the heating time increased to 30 min, the broad signal at about –12 ppm becomes more distinct. From the spectra of samples heated from 20 to 40 min, a weak shoulder gradually appears at around –19 ppm which can be clearly detected in the spectrum of the 40 min sample, suggesting a new phase starts forming. In the literature,[34, 35] most of the reported ^{31}P chemical shifts fall in the range from –19 to –30 ppm for the $AlPO_4$-based materials. It is generally accepted that the peaks in this region are due to fully condensed P sites (i.e. the P atoms tetrahedrally bind to four Al atoms via bridging oxygen atoms).[30, 36] Thus, the emergence of the new resonance at about –19 ppm indicates the development of a new type of P sites with $P(-OAl)_4$ environment. On the other hand, there is almost no change for the relatively sharp peak centered at –5 ppm.

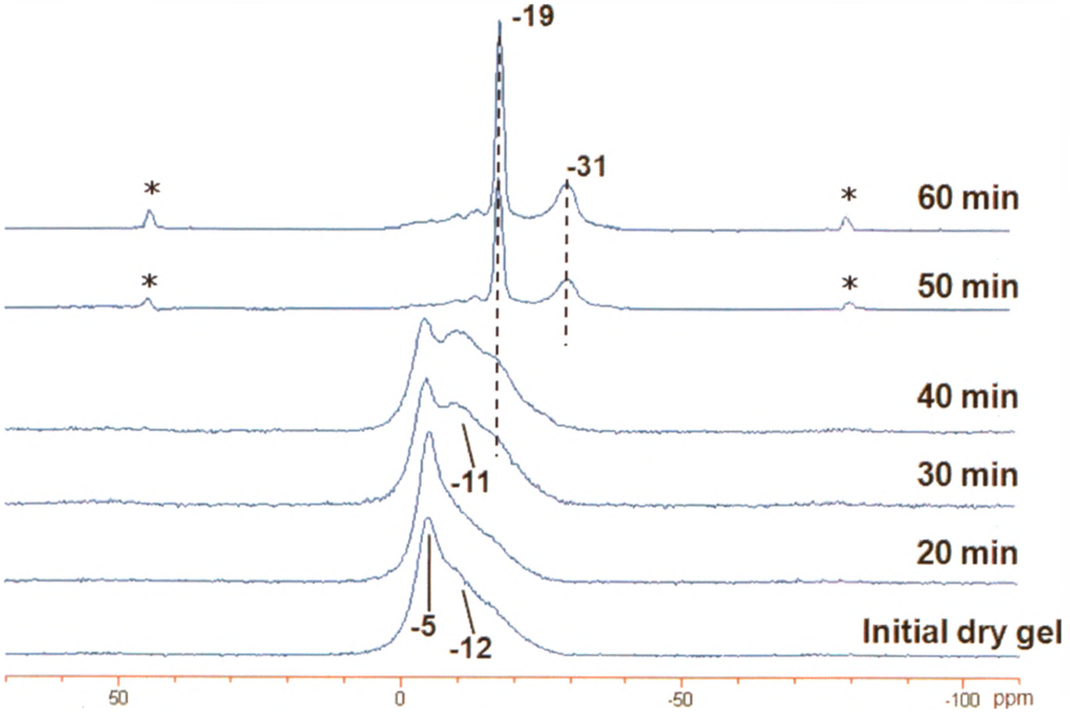

Figure 4.12 ^{31}P MAS NMR spectra of the initial dry gel and dry gel samples heated at 200 °C (* indicates spinning sideband)

The ^{31}P MAS spectrum of the 50 min sample is quite different from that of the 40 min sample. The weak resonance at about –19 ppm dramatically evolves into a sharp strong peak accompanied with a new peak appeared at –31 ppm at the expanse of the signals at –5 and –11 ppm, which coincides with the appearance of the sharp reflections in the corresponding XRD pattern. Both resonances at –19 and –31 ppm are attributed to the fully condensed P sites of the crystalline $AlPO_4$-based phases. Since the P sites only have one type of chemical environment ($P(–OAl)_4$) in $AlPO_4$-based molecular sieves, the different ^{31}P resonances are due to the crystallographically non-equivalent P sites.[34, 35] As a result, the crystalline $AlPO_4$-based phases have formed at the expense of the amorphous phase, semi-crystalline layered phase and amine-phosphate species.

In the previous NMR studies of $AlPO_4$-16 molecular sieve,[17, 18] there are two main ^{31}P peaks observed at around –19 and –29 ppm with the intensity ratio close to 1:4, which are attributed to the two types of crystallographic sites (P_2 and P_1). Compared to the spectra of the previous studies, the resonances in the present study have the same chemical shifts as those of $AlPO_4$-16 but with a different intensity ratio (1.5:1). Based on the corresponding XRD patterns shown before, these two resonances can be assigned to the $AlPO_4$-16 and the by-product. Thus, we can assume that the resonance at –19 ppm is largely attributed to the by-product with a small amount of $AlPO_4$-16. The by-product has a similar local environment as the P_2 site of $AlPO_4$-16. The spectrum also indicates that the 50 min sample still contains non-crystalline phases. The spectrum of the 60 min sample is the same as that of the 50 min sample. Overall, the ^{31}P NMR spectra are consistent with the corresponding XRD patterns.

The ^{27}Al MAS spectra of the initial SAC dry gel and selected gel samples heated at 200 °C are shown in Figure 4.13. The spectrum of the initial dry gel shows two weak peaks at about 42 and –18 ppm and a strong peak at 5 ppm. The weak peak at 42 ppm falls within the range from 35 to 48 ppm reported in the literature for tetrahedral Al environments of $Al(-OP)_4$ for most microporous $AlPO_4$-based materials.[34, 35, 37] On the basis of its shift value, the weak peak at –18 ppm can be attributed to the octahedral Al atoms in AlPO species, i.e. $Al(-OP)_4(OH_2)_2$.[35] Thus, the two weak peaks can be assigned to the layered AlPO phase in the initial dry gel. The strong peak at 5 ppm is probably due to the unreacted aluminum source, since the ^{27}Al MAS of pseudoboehmite (Catapal B) displays a single resonance at the range of 6 to 10 ppm.[17, 31, 38] The spectrum is also consistent with the corresponding XRD pattern (Figure 4.2) which exhibits the reflections of pseudoboehmite.

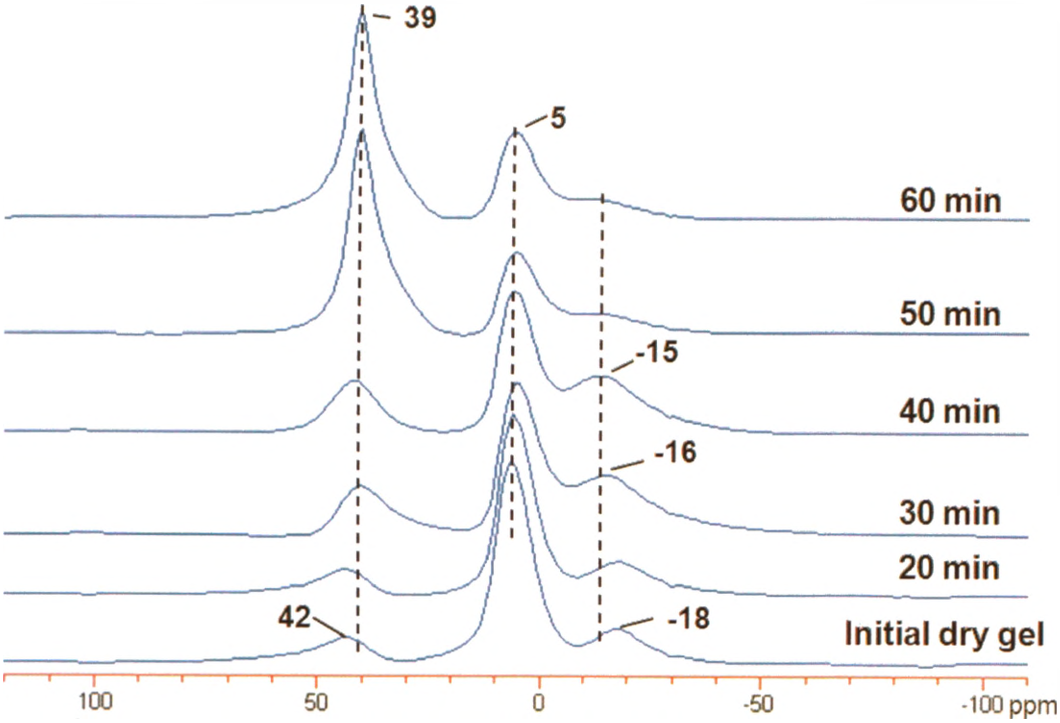

Figure 4.13 ^{27}Al MAS NMR spectra of the initial dry gel and dry gel samples heated at 200 °C

The spectra of the gel samples heated from 20 min to 40 min also contain the three peaks similar to those of the initial gel only with a slightly different shift. However, the intensity of the peak at 5 ppm decreases and the intensities of the other two peaks increase with increasing the heating time. This means a part of aluminum source gradually reacts with the other species (amine-phosphate) in the dry gel. In the spectrum of the 50 min sample, the weak peak at about 39 ppm seen in previous spectra dramatically evolves into the strongest peak, suggesting a large number of tetrahedral Al sites have formed in the crystalline products. The weak peak at about –15 ppm which is due to the octahedral Al sites in the layered AlPO phase almost disappears. This spectrum is similar to that of the $AlPO_4$-16 with residual amorphous alumina reported in literature.[17] Thus, the resonance at 39 ppm is attributed to both $AlPO_4$-16 and the by-product with tetrahedral Al environments. The spectrum of the 60 min sample is as same as that of the 50 min sample.

To further ensure the layered phase is a true intermediate, we also conducted the ^{31}P and ^{27}Al MAS NMR experiments on the same samples used for the XRD experiments (Figure 4.4). The ^{31}P MAS spectrum (Figure 4.14) of the 200 °C 30 min sample reheated at 200 °C for 1 hour under SAC conditions is the same as that of the 200 °C 60 min sample. Similarly, there is no noticeable difference between the ^{27}Al MAS spectra (Figure 4.15) of the two samples. These results are consistent with the corresponding XRD results, which show that the crystallization can be resumed under the SAC conditions. Thus, we can confirm that the dry gel sample (200 °C 30 min sample) is indeed a true reactive intermediate of the $AlPO_4$-16.

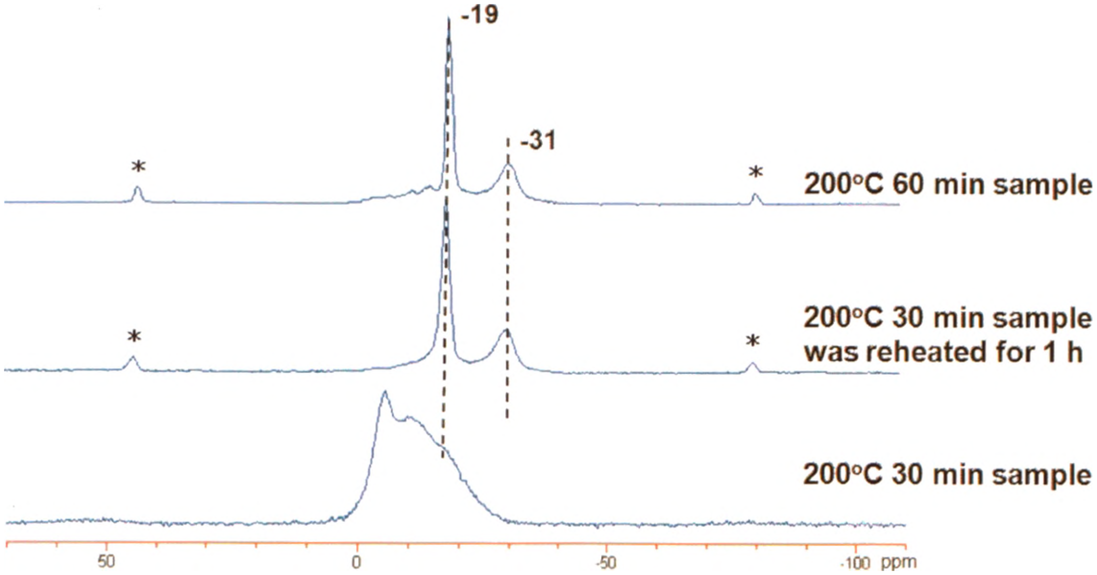

Figure 4.14 ^{31}P MAS NMR spectra of 30 min sample before and after reheated at 200 °C for 1 hour under the same SAC conditions and 200 °C 60 min sample (* indicates spinning sideband)

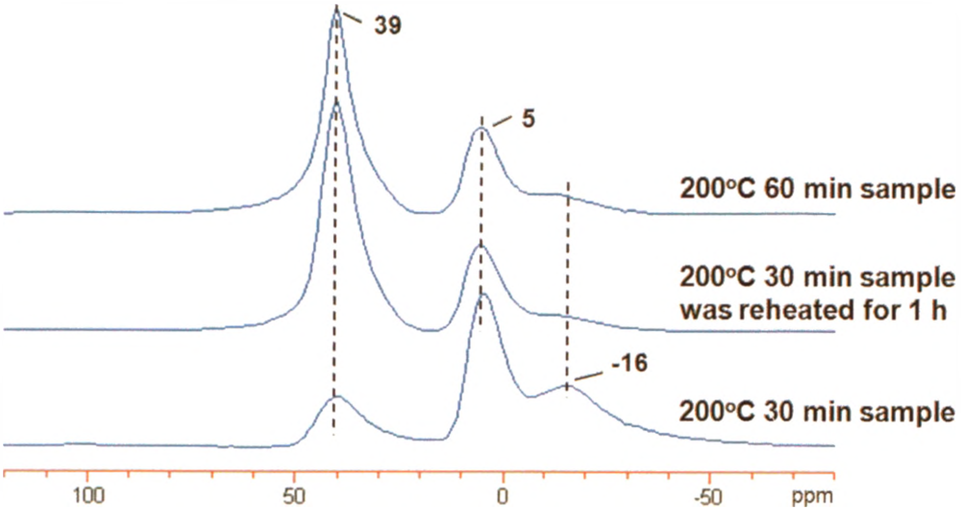

Figure 4.15 ^{27}Al MAS NMR spectra of 30 min sample before and after reheated at 200 °C for 1 hour and 200 °C 60 min sample

From the XRD patterns shown before, the reflections of the by-product can be removed from the patterns of the selected 200 °C samples after calcination at 550 °C for 2 hours. To gain the information on the local environments of Al and P atoms of the selected 200 °C samples after calcination, the ^{31}P and ^{27}Al MAS spectra of these samples were obtained.

The ^{31}P MAS spectra of these samples are shown in Figure 4.16. All the spectra of the calcined samples are quite different from those of the corresponding samples before calcination (Figure 4.12). Only a single resonance at about –26 ppm can be noticed in the spectrum of the calcined 40 min sample. The fact that the peak is extremely broad indicates a large distribution of chemical shifts, suggesting that the sample is amorphous. Thus, this signal is due to an amorphous material resulting from the layered AlPO intermediate phase which has collapsed upon calcination.

A broad signal (which has an asymmetric line-shape) in the spectrum of the calcined 50 min sample is similar to that in the spectrum of the calcined 40 min one. Based on the corresponding XRD pattern, the main peak centered at –28 ppm is attributed to the fully condensed P sites in an amorphous material originating from the collapsed by-product. The weak shoulder near –20 ppm in the spectrum can be assigned to the tetrahedral P_2 sites in the $AlPO_4$-16 structure. As mentioned before, the ^{31}P spectrum of $AlPO_4$-16 should have another resonance due to the tetrahedral P_1 sites at around –29 ppm, and this peak apparently overlaps with the broad peak at –28 ppm in this spectrum. Thus, the chemical shifts of the new formed amorphous phase indicate that the P chemical environments of the amorphous material resulting from the calcined 50 min sample are similar to those of $AlPO_4$-16. The spectrum of the calcined 60 min sample is the same as that of the calcined 50 min one, which is consistent with the corresponding XRD patterns.

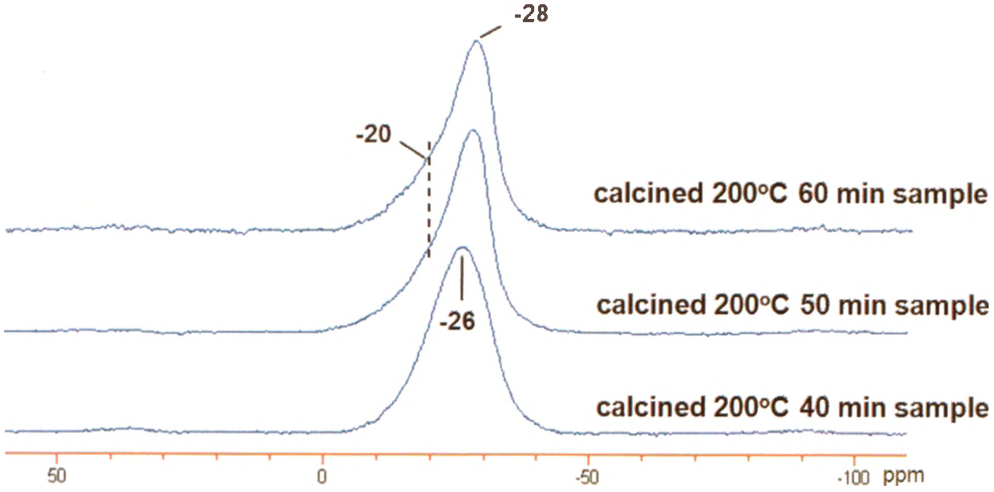

Figure 4.16 ^{31}P MAS NMR spectra of selected samples calcined for 2 hours

The ^{27}Al MAS spectra of the same samples are shown in Figure 4.17. All the spectra of the calcined samples are quite similar, with the three resonances at 38, 5 and –18 ppm similar to those mentioned in the spectra of the corresponding samples before calcination (Figure 4.13). The intensity of the peak at 39 ppm in the spectrum of the 40 min sample before calcination largely increases in the spectrum of the calcined 40 min sample, suggesting that the amorphous phase contains a large number of tetrahedral Al.

The signal at 38 ppm in the spectrum of the calcined 50 min sample can be attributed to tetrahedral Al sites in the structures of $AlPO_4$-16 and the amorphous material originating from the collapsed by-product from the corresponding XRD pattern and ^{31}P spectrum. The peak at –18 ppm can be assigned to the octahedral Al atoms in the layered AlPO species. The spectrum of the calcined 60 min sample looks the same as that of the calcined 50 min one. The similarities in ^{31}P and ^{27}Al MAS spectra between the calcined 40 and 50 min samples indicate that upon calcination the semi-crystalline layered phase and the by-product transform to the same amorphous material.

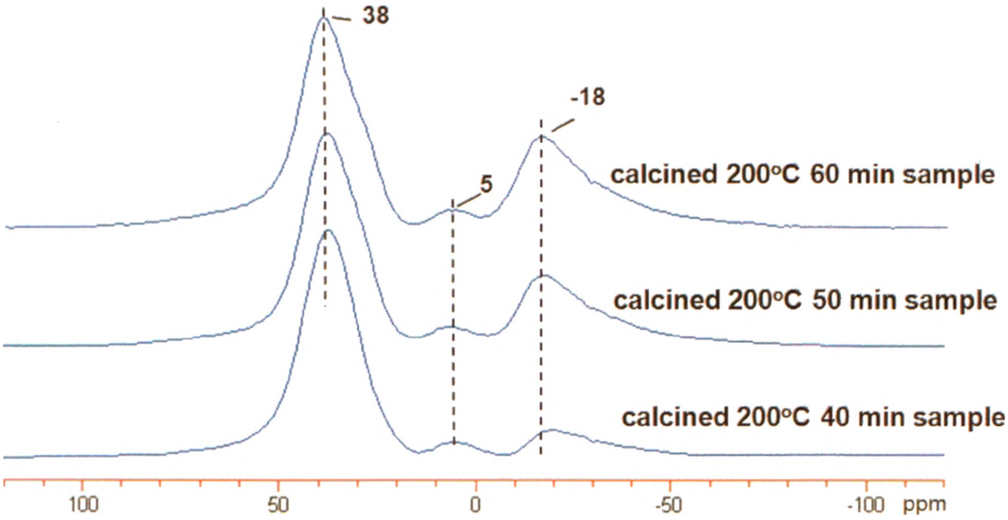

Figure 4.17 ^{27}Al MAS NMR spectra of selected samples calcined for 2 hours

To gain the information on the local environments of Al and P atoms in the samples whose XRD patterns only contain the distinct reflections of $AlPO_4$-16, the ^{31}P and ^{27}Al MAS spectra of these samples were also obtained.

The ^{31}P MAS spectra of the 50 min sample before and after different post-synthesis treatments are shown in Figure 4.18. In the ^{31}P spectrum of the washed 50 min sample, two resonances can be seen at about –12 and –31 ppm. Actually, there are three resonances in the deconvoluted spectrum with the additional one at about –22 ppm. The peaks centered at −22 and −31 ppm are attributed to the two crystallographically inequivalent P sites of $AlPO_4$-16[17, 18] with an intensity ratio of 1:3.4 which is close to the theoretical intensity ratio of the two sites (P_2:P_1 = 1:4). The broad peak observed at −12 ppm is due to the P sites with lower degrees of condensation[34, 36] in an amorphous material. Compared the two spectra of the 50 min sample before and after being washed by water, the emergence of the peak at −12 ppm is accompanied by the large decrease in the intensity of the peak at −19 ppm, which means that the by-product has transformed to an amorphous material by washing.

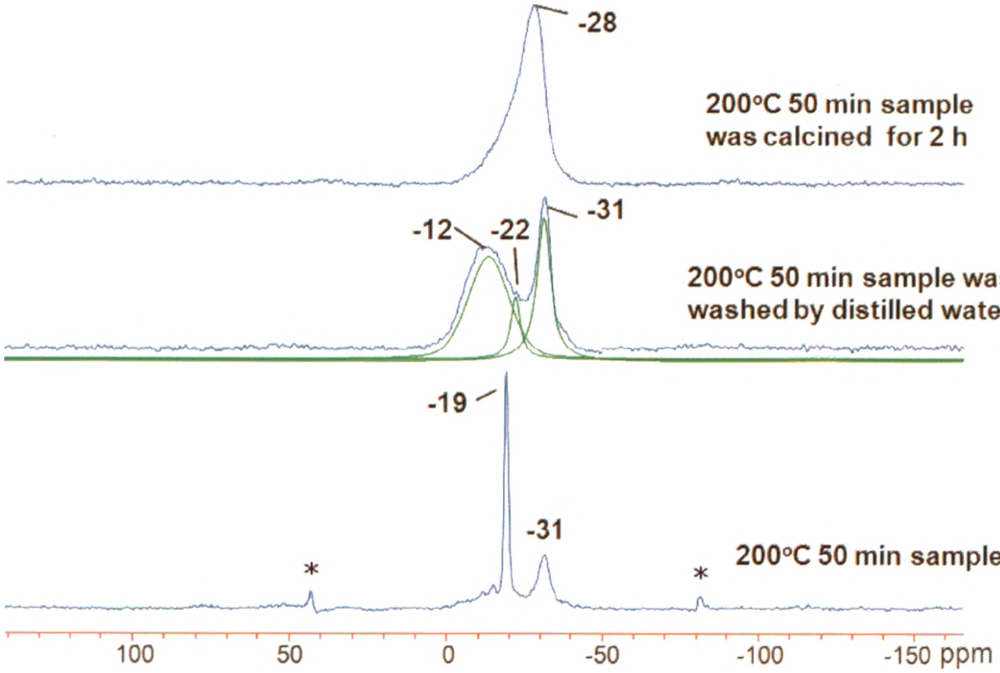

Figure 4.18 ^{31}P MAS NMR spectra of 200 °C 50 min sample before and after different post-synthesis treatments (* indicates spinning sideband)

A comparison with the ^{31}P spectrum of the calcined 50 min sample suggests that the amorphous materials from calcination and washing are different, since they have quite different ^{31}P MAS spectra. Such difference cannot be differentiated from the corresponding XRD patterns (Figure 4.7).

The ^{27}Al MAS spectra of the 50 min sample before and after different post-synthesis treatments are shown in Figure 4.19. In the ^{27}Al spectrum of the 50 min sample, the strongest peak at 39 ppm is attributed to the tetrahedral Al sites in the structures of $AlPO_4$-16 and the by-product. The weak peak at 5 ppm and a hump at about –15 ppm are due to the unreacted alumina and the octahedral Al sites in the layered AlPO phase, respectively.

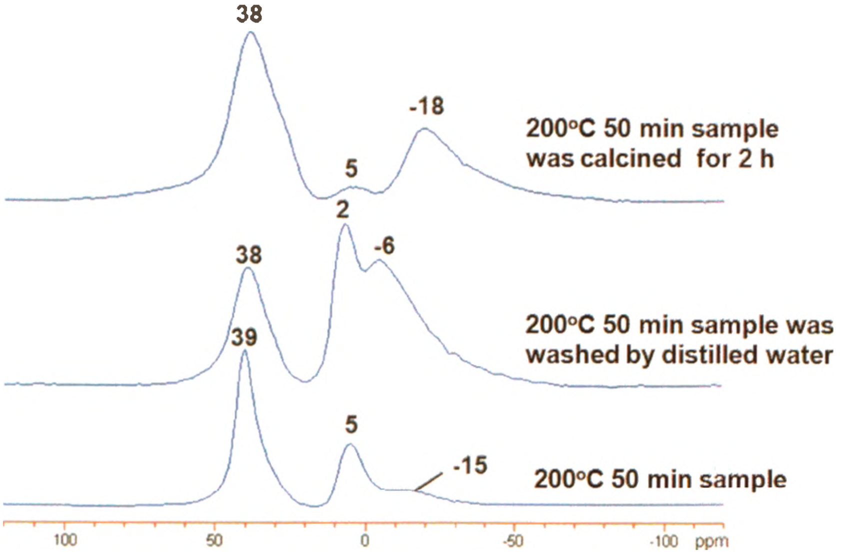

Figure 4.19 ^{27}Al MAS NMR spectra of 200 °C 50 min sample before and after different post-synthesis treatments

In the ^{27}Al spectrum of the washed 50 min sample, three resonances are detected at about 38, 2 and –6 ppm. Compared to the spectrum of the sample before being washed by water, the intensity of the peak at around 38 ppm decreases drastically and this is accompanied by the appearance of a new peak at around –6 ppm which is attributed to the octahedral Al of a new material. Based on the corresponding ^{31}P MAS spectrum, we believe that the new material is the amorphous material transformed from the by-product by washing. The peak at 2 ppm can be assigned to the alumina in the sample.

The resonance at 38 ppm in the ^{27}Al spectrum of the calcined 50 min sample can be assigned to tetrahedral Al sites in $AlPO_4$-16 and the amorphous material resulting from the collapsed by-product. The peak at –18 ppm is attributed to the octahedral Al sites in the amorphous AlPO species. It appears that the amorphous materials obtained from washing and calcination have very different octahedral Al environments.

4.4 Summary

The cubic form of $AlPO_4$-16 can be prepared with HEX as a SDA by SAC method, which has not been reported before. However, under the SAC conditions, the final product is a mixture of $AlPO_4$-16 and a crystalline unknown by-product. This by-product cannot be removed by changing the reaction time and temperature. Although calcination and washing with water result in the disappearance of the reflections due to the by-product from the XRD patterns, the ^{27}Al and, in particular, ^{31}P MAS spectra show that calcination and washing only convert the by-product to the amorphous materials. The amorphous material formed under calcination has fully condensed P sites, $P(–OAl)_4$, in its structure. The ^{31}P chemical shift implies that the amorphous material may have the 6MR units similar to those in the structure of $AlPO_4$-16. The amorphous material obtained by washing has less condensed P environments, such as $P(–OAl)_3(OH)$ and $P(–OAl)_2(OH)_2$. The NMR results indicate that neither calcination nor washing can remove the impurity.

The $AlPO_4$-16 structure is formed via a semi-crystalline layered AlPO intermediate. If the SDA is removed from this intermediate such as extensive washing, no crystalline AST structure will form. The by-product probably has a similar P and Al local structures as those of $AlPO_4$-16 with large polyhedra constituted by 6MR. This by-product is a competing phase rather than an intermediate of $AlPO_4$-16.

4.5 References

[1]H. Van Bekkum, E. Flanigen, P. Jacobs and J. Jansen, *Introduction to Zeolite Science and Practice, 2nd Completely revised and Expanded Edition*, 2001.

[2]P. Wright, *Microporous framework solids*, Royal Society of Chemistry, 2008.

[3]C.S. Cundy and P.A. Cox, Microporous Mesoporous Mater., 82 (2005) 1.

[4]M.E. Davis and R.F. Lobo, Chem. Mater., 4 (1992) 756.

[5]R.J. Francis and D. O'Hare, J. Chem. Soc., Dalton Trans., (1998) 3133.

[6]A.K. Cheetham and C.F. Mellot, Chem. Mater., 9 (1997) 2269.

[7]O.B. Vistad, D.E. Akporiaye, F. Taulelle and K.P. Lillerud, Chem. Mater., 15 (2003) 1639.

[8]M.H. Kim, H.X. Li and M.E. Davis, Microporous Mater., 1 (1993) 191.

[9]W. Xu, J. Dong, J. Li, J. Li and F. Wu, J. Chem. Soc., Chem. Commun., (1990) 755.

[10]P.R.H.P. Rao and M. Matsukata, Chem. Commun., (1996) 1441.

[11]L. Zhang and G.R. Gavalas, Chem. Commun., (1999) 97.

[12]M. Matsukata, M. Ogura, T. Osaki, P. Raja, H.P. Rao, M. Nomura and E. Kikuchi, Top. Catal., 9 (1999) 77.

[13]B. Chen and Y. Huang, J. Am. Chem. Soc., 128 (2006) 6437.

[14]B. Chen and Y. Huang, J. Phys. Chem. C, 111 (2007) 15236.

[15]S.T. Wilson, B.M. Lok, C.A. Messina, T.R. Cannan and E.M. Flanigen, J. Am. Chem. Soc., 104 (1982) 1146.

[16]J.M. Bennett and R.M. Kirchner, Zeolites, 11 (1991) 502.

[17]C. Schott-Darie, J. Patarin, P.Y. Le Goff, H. Kessler and E. Benazzi, Microporous Mater., 3 (1994) 123.

[18]L. Schreyeck, P. Caullet, J.C. Mougenel, J. Patarin and J.L. Paillaud, Microporous Mater., 11 (1997) 161.

[19]L.A. Villaescusa, P.A. Barrett and M.A. Camblor, Chem. Mater., 10 (1998) 3966.

[20]R.L. Withers and Y. Liu, J. Solid State Chem., 178 (2005) 2647.

[21]P. Caullet, J.L. Guth, J. Hazm, J.M. Lamblin and H. Gies, Eur. J. Solid State Inorg. Chem., 28 (1991) 345.

[22]F. Marcuccilli Hoffner, L. Delmotte and H. Kessler, Zeolites, 13 (1993) 60.

[23]C.A. Fyfe, A.R. Lewis and J.-M. Chezeau, Can. J. Chem., 77 (1999) 1984.

[24]R. Garcia, M. Arranz, T. Blasco and J. Perez-Pariente, Microporous Mesoporous Mater., 114 (2008) 312.

[25]F. Gandara, B. Gomez-Lor, M. Iglesias, N. Snejko, E. Gutierrez-Puebla and A. Monge, Chem. Commun, (2009) 2393.

[26]K.J. Balkus, Jr., A.G. Gabrielov and S. Shepelev, Microporous Mater., 3 (1995) 489.

[27]N. Venkatathri, S.G. Hegde, V. Ramaswamy and S. Sivasanker, Microporous Mesoporous Mater., 23 (1998) 277.

[28]N. Venkatathri, S.G. Hegde and S. Sivasanker, Indian J. Chem., Sect. A: Inorg., Bio-inorg., Phys., Theor. Anal. Chem., 43A (2004) 247.

[29]B. Chen and Y. Huang, Stud. Surf. Sci. Catal., 170A (2007) 222.

[30]Y. Huang, B.A. Demko and C.W. Kirby, Chem. Mater., 15 (2003) 2437.

[31]Y. Huang, D. Machado and C.W. Kirby, J. Phys. Chem. B, 108 (2004) 1855.

[32]Z. Liu, W. Xu, G. Yang and R. Xu, Microporous Mesoporous Mater., 22 (1998) 33.

[33]S. Prasad and S.-B. Liu, Chem. Mater., 6 (1994) 633.

[34]A. Sayari, I. Moudrakovski, J.S. Reddy, C.I. Ratcliffe, J.A. Ripmeester and K.F. Preston, Chem. Mater., 8 (1996) 2080.

[35]C.S. Blackwell and R.L. Patton, J. Phys. Chem., 92 (1988) 3965.

[36]Y. Huang, Z. Yan and R. Richer, Chem. Mater., 17 (2005) 6545.

[37]D. Hasha, L. Sierra de Saldarriaga, C. Saldarriaga, P.E. Hathaway, D.F. Cox and M.E. Davis, J. Am. Chem. Soc., 110 (1988) 2127.

[38]P.J. Grobet, J.A. Martens, I. Balakrishnan, M. Mertens and P.A. Jacobs, Appl. Catal., 56 (1989) L21.

Chapter 5 Conclusions and Future Work

5.1 Conclusions

Although the thermal stabilities of zeolites have been studied extensively, the behaviour of zeolites under high external pressures is much less understood. In the first part of the thesis, we investigated the behaviour of the completely siliceous as-made and calcined zeolite ZSM-5 under high pressures up to 16 GPa by *in situ* Raman and Infrared spectroscopies as well as X-ray diffraction with synchrotron radiation using diamond anvil cell (DAC). We also examined the effect of external pressure on the morphology of the zeolitic sample using scanning electron microscopy (SEM). The results indicate that both zeolites undergo the pressure-induced amorphization (PIA) and experience two successive phase transitions under high pressures: (1) the crystalline zeolite transforms to low density amorphous (LDA) silica phase and (2) the LDA silica is converted to high density amorphous (HDA) silica phase.

For the as-made siliceous ZSM-5, it starts to transform to the LDA silica at around 3 GPa. Between 3 to 7 GPa, the as-made siliceous ZSM-5 and LDA silica coexist and the amount of LDA silica gradually increases with increasing pressure. This phase transformation is complete at around 7 GPa. Above 7 GPa, the LDA silica begins to evolve into the HDA silica. Finally, the conversion of the LDA to the HDA silica is complete at around 14 GPa. For the calcined siliceous ZSM-5, its framework deforms quickly under pressure and the zeolite starts to transform to the LDA silica at around 1.5 GPa. The LDA to HDA phase transition begins at around 3 GPa and the amount of HDA phase increases with increasing pressure. Above 11 GPa, only the HDA silica exists in the system.

Both of as-made and calcined siliceous ZSM-5 gradually transform to the LDA silica. In the LDA phase, the MFI framework lost its long-range ordering due to the deformation of the framework via rigid rotations of the SiO_4 tetrahedra.[1] However, the Si-O-Si connectivities are largely retained. At higher pressure, the LDA phase gradually transforms to the HDA silica. In the HDA phase, the large 10-membered rings (10MR) existing in the MFI structure collapse to small rings (3MR and 4MR) via Si-O bond breaking and reforming, resulting in a denser amorphous material. Although the general phase behaviour of as-made and calcined ZSM-5 under pressure is similar, the onset pressures of amorphization and polyamorphic transition of the calcined siliceous ZSM-5 are much lower than those of the as-made one. This is because the calcined ZSM-5 has no template molecules inside its channels. The existence of the TPA^+ cations in as-made ZSM-5 effectively prevents the significant framework deformation from occurring in the early stage of compression.

We also demonstrated that the PIA is reversible in the LDA phase where the long-range ordering of the framework is lost, but the overall framework topology and Si-O-Si connectivities are preserved. The PIA appears to be irreversible in the HDA phase which loses the zeolite framework topology due to the significant bond breaking and reforming under higher pressures. The pressure range of reversible PIA is wider for the as-made ZSM-5 (0 – 7 GPa) than that for the calcined material (0 – 3 GPa). This is due to the fact that the occluded TPA^+ cations can act as rigid 'organizing centers' for the reversible transformation.[2] For the samples where both the LDA and HDA phases coexist, the amount of ZSM-5 that can be re-crystallized upon releasing the pressure is proportional to the LDA in the mixture. In general, how easily the siliceous ZSM-5 can be recovered from the amorphous materials largely depends on the existence of template cations (TPA^+) and the maximum pressures applied.

The crystallization mechanisms of $AlPO_4$-based molecular sieves are not yet fully understood on a molecular level. In the second part of this thesis, we examined the synthesis and the formation process of $AlPO_4$-16 by dry gel conversion (DGC) method. It was shown that the cubic form of $AlPO_4$-16 can be synthesized using hexamethyleneimine (HEX) as a structure directing agent (SDA) by steam-assisted conversion (SAC) method. However, the final product is a mixture of $AlPO_4$-16 and a crystalline unknown by-product. This by-product is not an intermediate of $AlPO_4$-16, but a competing phase. This competing phase has local P structures very similar to the P sites in the 6MR of $AlPO_4$-16. The by-product, however, cannot be suppressed by changing the reaction time and temperature. Although either calcination or washing with water appears to be able to remove the reflections due to the by-product from XRD patterns, the ^{27}Al and, in particular, ^{31}P MAS NMR results show unambiguously that the calcination and washing only convert the by-product to amorphous materials. The amorphous phases formed by calcination and washing have different structures. The amorphous phase resulting from the calcination has fully condensed P sites ($P(-OAl)_4$), and this material seems to have the 6MR which also exist in the structure of $AlPO_4$-16. The amorphous material formed by washing has P sites with a lower degree of condensation. The possible P environments include $P(-OAl)_3(OH)$ and $P(-OAl)_2(OH)_2$. It was also demonstrated that the $AlPO_4$-16 structure is formed via a semi-crystalline layered AlPO-based intermediate and the existence of the SDA is essential since no $AlPO_4$-16 forms when the SDA is removed even partially from this intermediate.

5.2 Suggestions for Future Work

1. More systematic synchrotron X-ray diffraction experiments should be carried out on the as-made and calcined siliceous zeolite ZSM-5 which need to be ground to a finer powder (less than 2μm in diameter) so that the crystal structures of the zeolites under high pressures can be refined and the unit-cell parameters can be calculated from the patterns.

2. High-temperature and high-pressure experiments can be performed on the zeolites to map out the *T-P* diagram.

3. If possible, the computational simulations should be conducted to reveal the

underlying mechanisms for amorphization of the zeolites.

4. More detained structural information on the intermediates of $AlPO_4$-16 (the semi-crystalline layered material) and the unknown by-product needs to be obtained by using more advanced solid-state NMR techniques.

5. Synthesizing pure phase $AlPO_4$-16 with different SDAs under DGC conditions should be explored.

5.3 References

[1] H. Xu, J. Zhang, Y. Zhao, G.D. Guthrie, D.D. Hickmott and A. Navrotsky, American Mineralogist, 92 (2007) 166.
[2] J.S. Tse, D.D. Klug, J.A. Ripmeester, S. Desgrenlers and K. Lagarec, Nature, 369 (1994) 724.

Appendix 2-D ADXRD Images of As-made Siliceous Zeolite ZSM-5

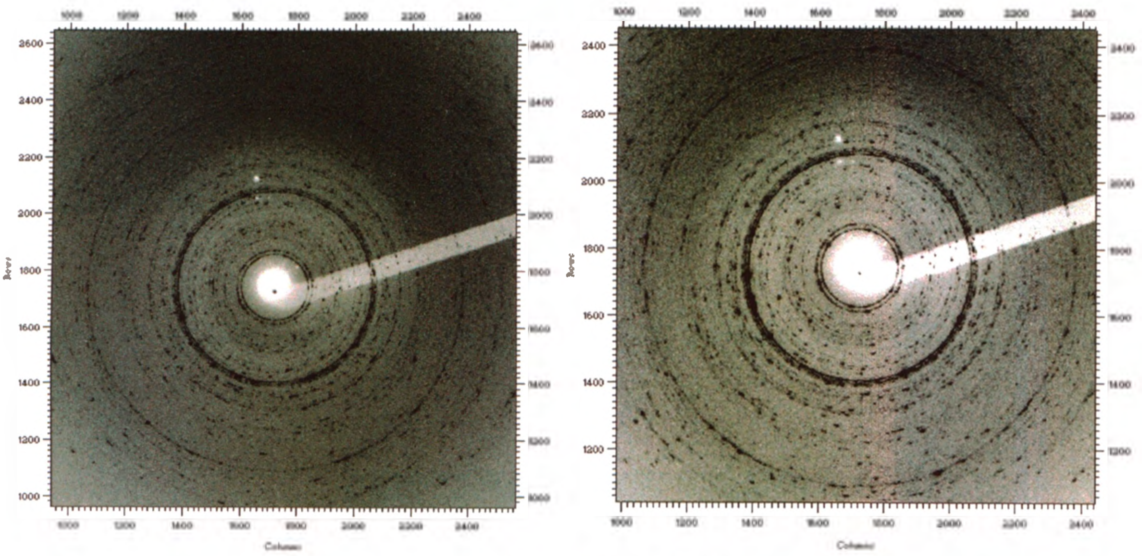

Figure A.1 Original images of the sample at ambient pressure (left) and at 0.2 GPa (right).

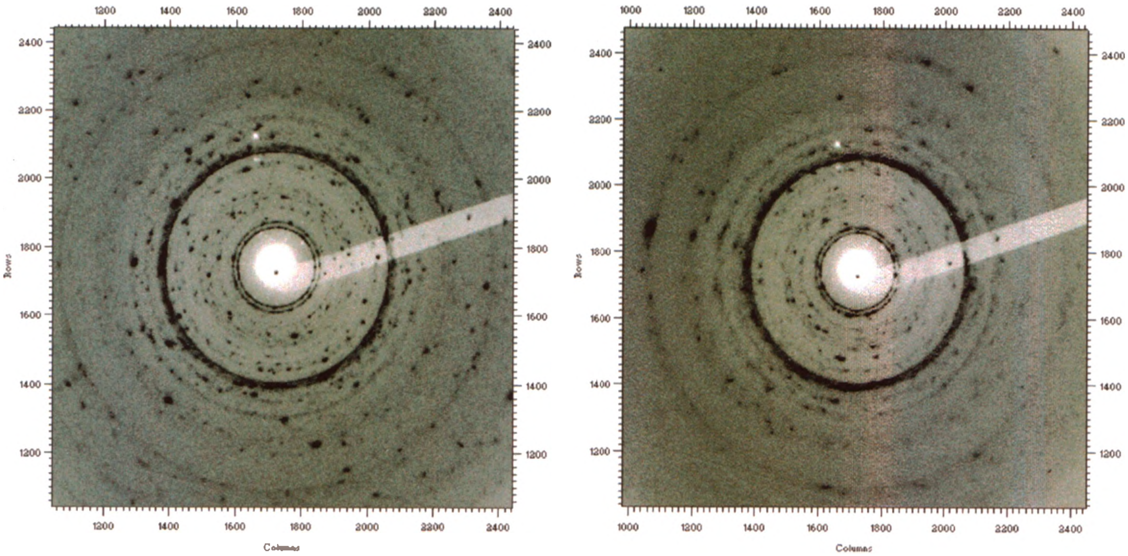

Figure A.2 Original images of the sample at 1.0 GPa (left) and at 1.4 GPa (right).

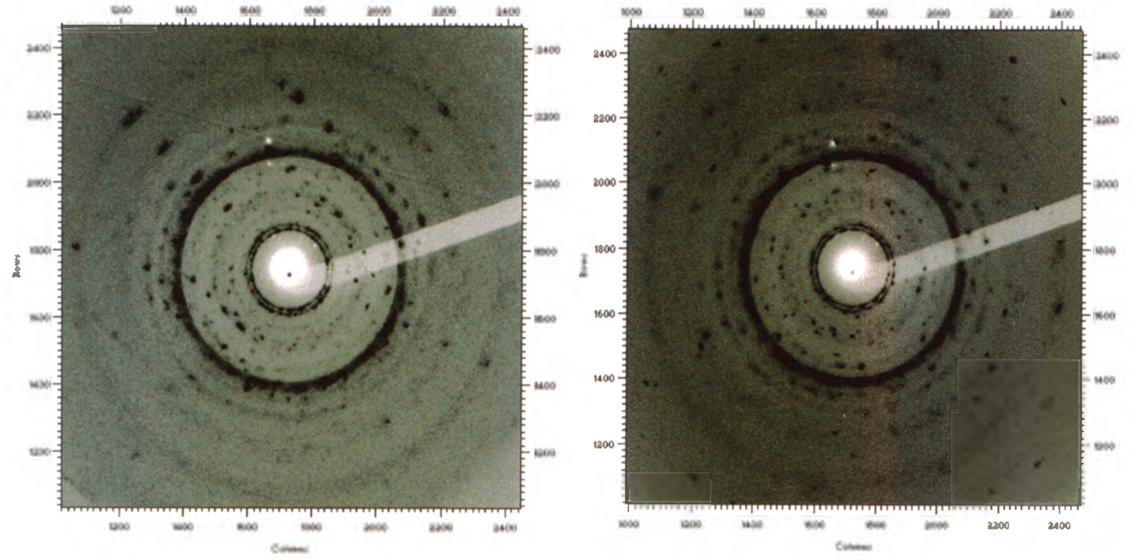

Figure A.3 Original images of the sample at 2.0 GPa (left) and at 2.4 GPa (right).

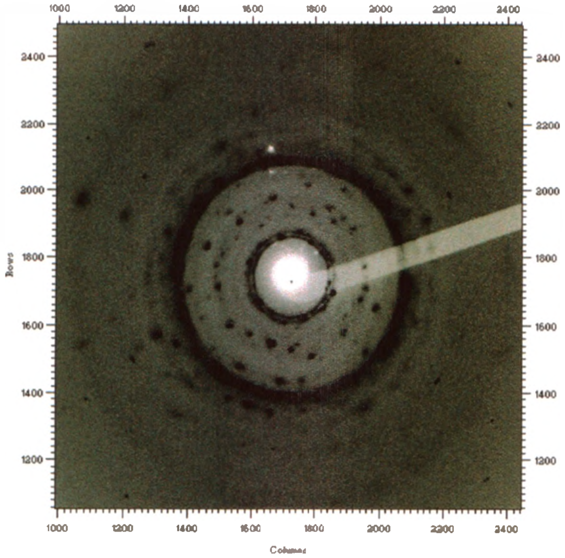

Figure A.4 Original image of the sample at 3.2 GPa.

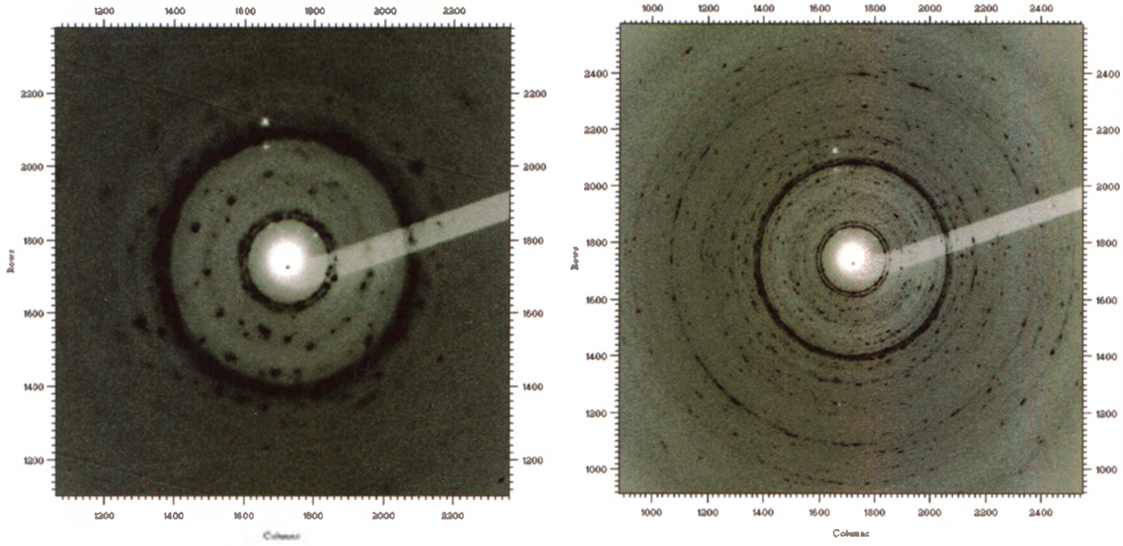

Figure A.5 Original images of the sample at 3.7 GPa (left) and recovered from 3.7 GPa (right).

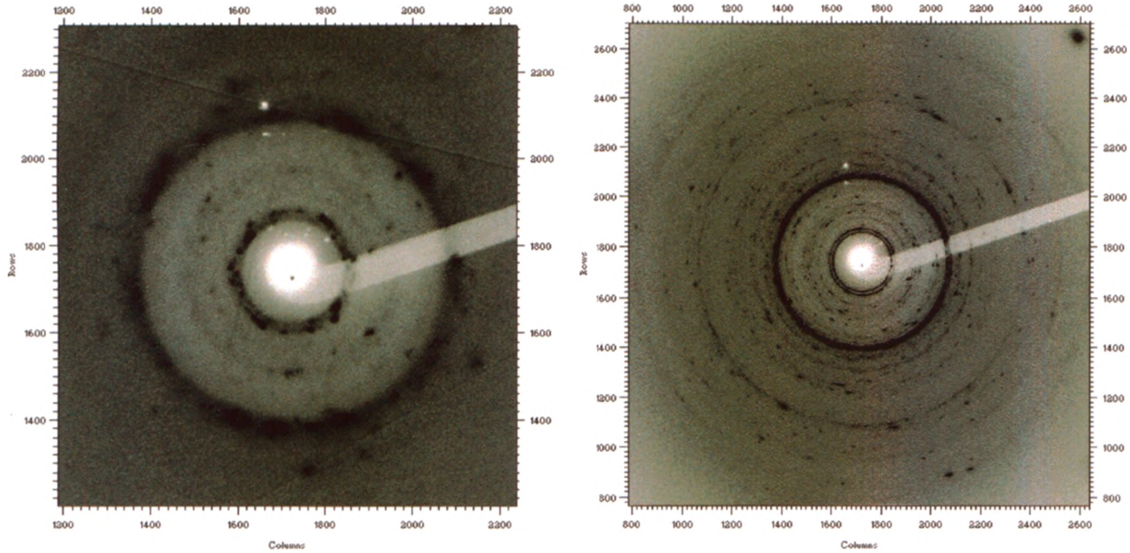

Figure A.6 Original images of the sample at 7.3 GPa (left) and recovered from 7.3 GPa (right).

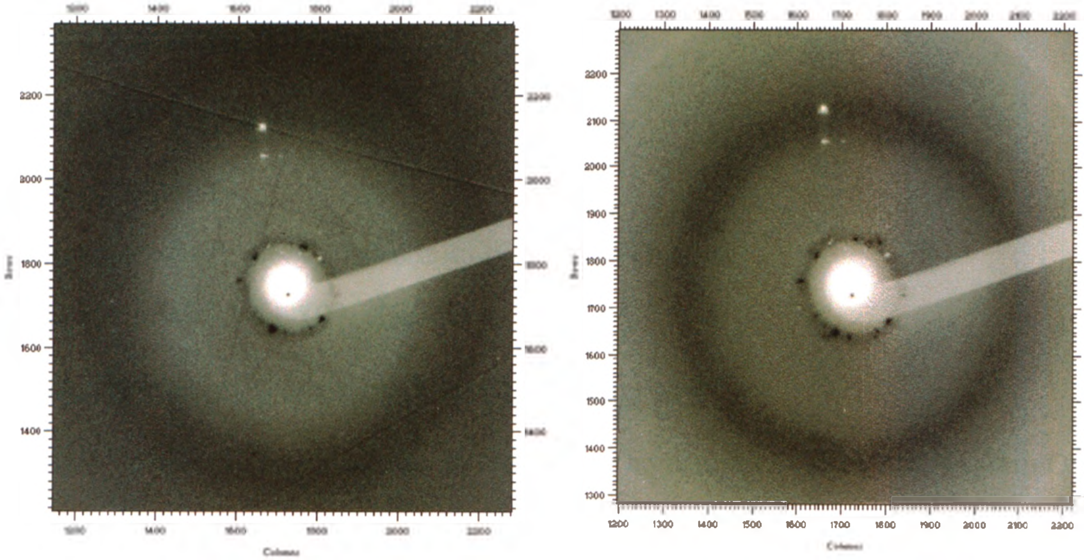

Figure A.7 Original images of the sample at 14.1 GPa (left) and recovered from 14.1 GPa (right).